University College of Southeast Norway
Applied Micro- and Nanosystems

Doctoral dissertation no 9
2017

Luis André Lourenço Fernandes

The development of a miniaturized hydration sensor based on the principle of osmotic pressure

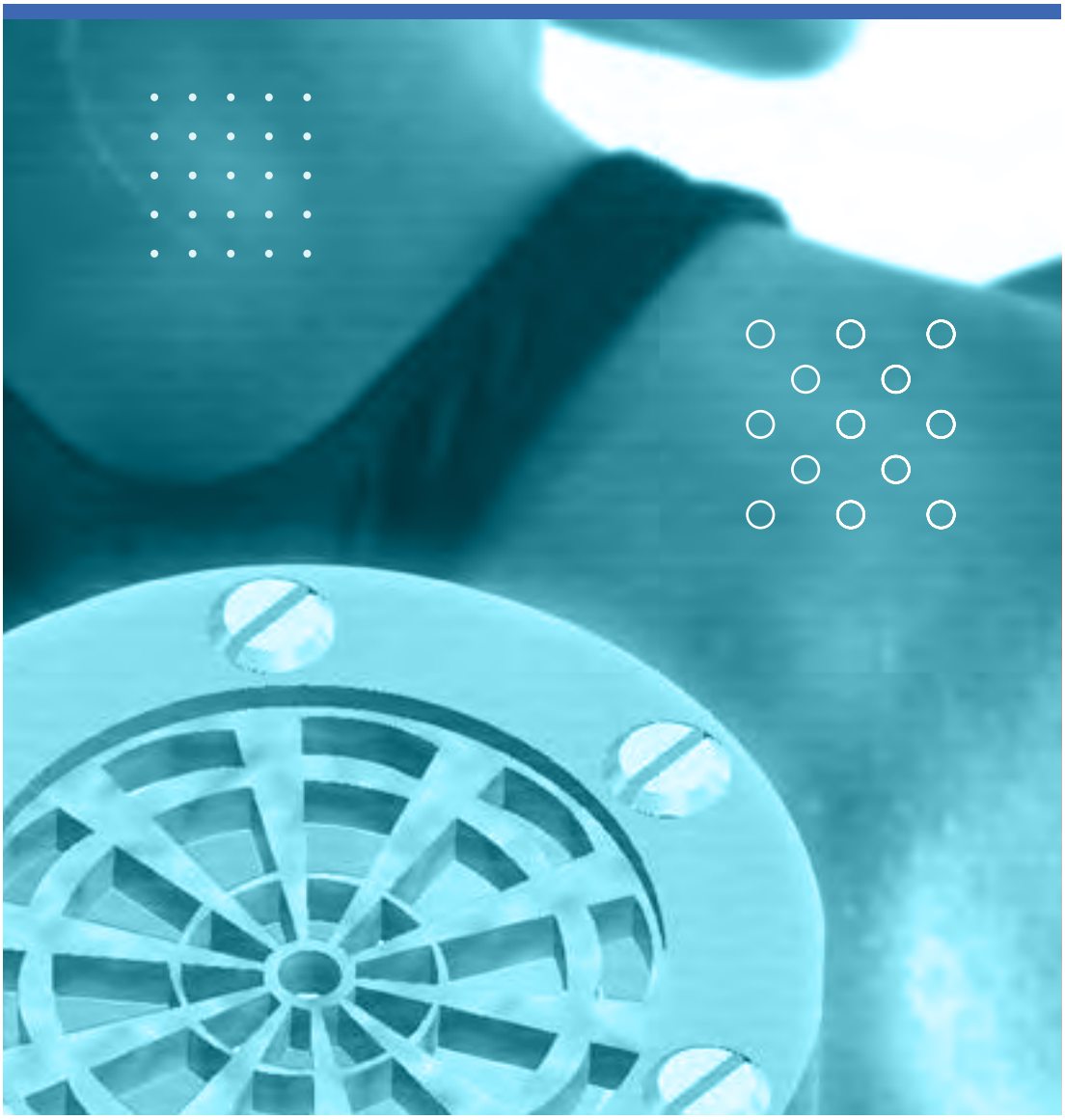

Luis André Lourenço Fernandes

The development of a miniaturized hydration sensor based on the principle of osmotic pressure

A PhD dissertation in
Applied Micro- and Nanosystems

Faculty of Technology
University College of Southeast Norway
Kongsberg, 2017

Doctoral dissertations at the University College of Southeast Norway no. 9

ISSN: 2464-2770 (print)
ISSN: 2464-2483 (electronic)
ISBN: 978-82-7860-286-7 (print)
ISBN: 978-82-7860-287-4 (electronic)

Print: **University College of Southeast Norway**

Abstract

The thesis presents a novel hydration sensor that employs osmotic pressure to detect de- and overhydration in body fluids. This sensor could be used to measure different levels of hydration in an organism, e.g. the human body. A prototype was fabricated in an acetal copolymer integrating a semi-permeable membrane and an electronic interface containing a resistive pressure transducer together with an ASIC and a few discrete components assembled on a silicon substrate. The sensor has a cavity (reference chamber) with a pressure transducer used to record the osmotic pressure induced by the physical separation between two solutions of different salt concentrations: the reference solution (inside the sensor's cavity) and the external media. The hydration sensor described in this work offers an alternate solution to the methods used today for measuring hydration (sampling of body fluids, skin impedance analysis, body weight, etc.). This makes it less complex, portable, smaller in size, with a low power consumption and capable of continuous measurements. Its low power architecture, in combination with the advances made in microfabrication, make it a suitable candidate for further miniaturization and implantation in the human body. This technology is a versatile medical sensor because of the physical principles it implements, for example: It uses a semi-permeable membrane for solute selectivity permitting the detection of changes in the concentration of different molecules in the human body which are indicators of changes in the human body electrochemical balance, helping to monitor different pathologies. Making use of the membrane's physical (porous size and density), chemical and electrical properties one can monitor (through an osmotic process) different solutes/molecules from the extracellular fluids and use the osmotic hydration sensor to sense other parameters, such as diabetes (glucose), kidney function (Sodium concentration), and blood volume (Hemoglobin), where the last parameter described is particularly important for post-operative care. The sensor presented in this work has three different development stages investigated with the use of other prototype sensors, which paved the way towards a final device, a *proof of concept* of a

novel osmotic hydration sensor that is validated for measuring hydration *"in vitro"*. The osmotic hydration sensor encapsulation was manufactured in acetal copolymer integrating a 25.4 µm thick ion-exchange Nafion (NR211) membrane and a silicon substrate measuring 10x10 mm. Both the pressure transducer and the ASIC were integrated to the substrate. The sensor was tested/validated for a ±20% hydration span, ranging from 220 $mOsmL^{-1}$ (overhydration) to 340 $mOsmL^{-1}$ (dehydration) and showing a resolution of approximately 2% with a response time of 5.5 hours to reach 100% signal. This result, corresponds to an accuracy of 5.71 bits for the sensor's dynamic range. The low power architecture implemented in the ASIC uses a low voltage supply (1 V) in the sub-threshold regime with bias currents of approximately 50 nA resulting in an average power consumption of only 39.4 µW. An Analog-to-Analog approach converts the voltage signal from the pressure transducer (due to a change in resistance) into a frequency output that, for every transition on the output, inverts the power to the transducer. This approach results in a resistance controlled oscillator (RCO), eliminating the use of a power-consuming clock to drive an Analog to Digital converter (ADC).

Acknowledgments

This PhD work has been developed at the Department of Micro and Nano Systems Technology (IMST) at the University College of Southeast Norway (USN) in collaboration with the Nanoelectronics group at the Department of Informatics (IFI) at the University of Oslo (UiO).

I would like to thank IMST, and IFI, for granting me the support and funding for the realization of this project. In addition, I would like to thank the Norwegian Micro- and Nanofabrication facility (NorFab), together with the Norwegian PhD Network on Nanotechnology for Microsystems (NanoNetwork), for their funding contributions.

During my PhD, the support, motivation, availability and friendship of my supervisor (Prof. Erik A. Johannessen) and co-supervisors (Dr. Philipp Häfliger and Dr. Mehdi Azadmehr) was essential for the success of this project and further development of my skills as a researcher. In addition, would like to express my sincere gratitude for their role in helping me getting a guest research position at the Department of Chemistry at the University of Connecticut (UConn). Furthermore, would like to thank Dr. Robert Birge (Professor Emeritus), Dr. Nicole Wagner and Dr. Jordan Greco at UConn for their support and advice.

Would also like to note the importance of all the lab technicians and other Researchers at IMST and IFI that helped me achieving good experimental procedures and results.

A special thank you note to the BioMEMS group members at IMST and Dr. Trung Thanh Nguyen at IFI for their contributions to my work.

Finally, this work would not have been possible without the support of my family that motivated me in taking this challenge. A special thank you note to my lovely wife that found this PhD position for me and to whom I am dedicating this thesis.

List of Publications

Note that papers omitted from online version due to publisher's restrictions

I. L. A. Fernandes, P. Häfliger, M. Azadmehr, and E. Johannessen, "Design and characterization of an osmotic sensor for the detection of events associated with dehydration and overhydration," IEEE Journal of Translational Engineering in Health and Medicine, vol. 1, pp. 1-9, 21 August 2013.

II. N. Trung Thanh, L. A. L. Fernandes, and P. Häfliger, "An Energy-Efficient Implantable Transponder for Biomedical Piezo-Resistance Pressure Sensors," Sensors Journal, IEEE, vol. 14, pp. 1836-1843, 2014.

III. L. A. Fernandes, E. Johannessen, M. Azadmehr, and P. Häfliger, "Low power integrated electronics system for the operation of a miniaturized hydration sensor," presented at the IEEE International New Circuits and Systems (NEWCAS), Trois-Rivières, Canada, vol. 14, pp. 17-20, 2014 (invited for communication/presentation).

IV. L. A. Fernandes, P. Häfliger, M. Azadmehr, and E. Johannessen, “An osmotic pressure sensor for monitoring the level of hydration in biological fluids”, Sensors Journal, IEEE, vol. 16, pp. 4331-4337, 2016.

List of abbreviations

DI	Deionized water
ICF	Intracellular fluid
ECF	Extracellular fluid
CM	Cell membrane
BF	Body fluids
TBW	Total body weight
ASIC	Application Specific Integrated Circuit
SMD	Surface Mount Devices
PV	Plasma volume
BIS	Bioelectrical impedance spectroscopy
MEMS	Microelectromechanical Systems
PCR	Polymerase chain reaction
DNA	Deoxyribonucleic acid
MWCO	Molecular weight cutoff
PTFE	Polytetrafluoroethylene
MF	Micro filtration
UF	Ultra filtration

RO	Reverse osmosis
PMN	Polymorphonuclear leukocytes
ROS	Reactive oxygen species
EMI	Electromagnetic interference
EMC	Electromagnetic compatibility
OPS	Osmotic pressure sensor
RC	Reference chamber
RS	Reference solution
OP	Osmotic pressure
OF	Osmotic flow
OE	Osmotic equilibrium
OS	Osmotic strength
PBS	Phosphate-buffered saline
ISO	International Organization for Standardization
MSCD	Mixed Signal Circuit Design
IC	Integrated Circuit
CMOS	Complementary metal–oxide–semiconductor
NMOS	n-channel MOSFET
PMOS	p-channel MOSFET

SNR	Signal-to-noise ratio
TSMC	Taiwan Semiconductor Manufacturing Company
FET	Field-effect transistor
MOSFET	Metal–oxide–semiconductor field-effect transistor
PSRR	Power supply rejection ratio
CMRR	Common mode rejection ratio
OTA	Operational Transconductance Amplifier
GBW	Gain bandwidth
OHS	Osmotic Hydration Sensor
HSS	High Speed Steel
TMAH	Tetramethylammonium hydroxide
EDS	Energy-dispersive X-ray spectroscopy
SEM	Scanning Electron Microscopy
STM	STMicroelectronics
ENOB	Effective Number of Bits
RMS	Root Mean Square

Table of Contents

1. Introduction 1

1.1. Motivation 1

1.2. Hydration 4

1.2.1. Dehydration 5

1.2.2. Overhydration 6

1.3. Measuring hydration and current state-of-the-art 7

1.4. MEMS applications in biomedical sensors 11

1.5. Membrane bounded microsystems for separation processes 13

1.5.1. Membrane structures 15

1.5.2. Membrane characteristics 19

1.5.3. Porous and composite membranes 22

1.5.4. Ion-exchange membranes 24

1.5.5. Gas permeable membranes 24

1.5.6. Membrane drawbacks 26

1.6. Packaging Challenges 27

1.6.1. Hermeticity 28

1.6.2. Biocompatibility 29

1.6.3. Electrical compatibility 33

1.6.4. Mechanical requirements 33

1.6.5. Electrical pathway 33

1.6.6. Internal packaging 33

1.6.7. Reliability 34

2. Osmotic pressure sensors 35
2.1. Osmotic pressure 36
2.1.1. Physiological aspects of osmosis 37
2.1.2. Osmotic strength 38
3. Sensor interface 41
3.1. Mixed Signal Circuit Design 44
3.1.1. Second order effects 48
3.1.2. Sub-threshold region 49
3.1.3. Triode region 50
3.1.4. Saturation region 51
3.1.5. Single stage amplifiers 51
3.1.6. CS stage with current source load 56
3.1.7. CS stage connected with a diode load 56
3.1.8. Differential amplifier 57
3.1.9. Current Mirror 58
3.1.10. PSRR, CMRR & SNR 59
4. Sensor Design Implementation 63
4.1. Osmotic pressure sensor 64
4.1.1. Encapsulation 65
4.1.2. Transducer 66
4.2. ASIC 68
4.2.1. Bandgap reference/Power amplifier 70
4.2.2. BIAS generator 71

4.2.3. Pressure-to-frequency converter 72
4.2.4. Temperature monitoring 75
4.2.5. Layout 75
4.2.6. Integration 76
5. Materials and Methods 79
5.1. Membrane investigation 80
5.2. ASIC 80
5.2.1. SNR 81
5.2.2. PSRR 81
5.2.3. Temperature monitoring 83
5.3. ASIC implementation & Characterization 83
5.4. Temperature dependency 84
5.5. Packaging 84
5.5.1. Prototype manufacture (tools) 84
5.5.2. Substrate preparation 85
5.6. Test and validation of osmotic hydration sensor 90
5.6.1. Reference solution preparation 91
5.6.2. Membrane preparation 91
5.6.3. Sensor assembly in reference solution 92
5.6.4. Sensor “bleeding” 92
5.6.5. Sensor validation 92
6. Results and discussion 95
6.1. Membranes 95

6.1.1. Ion-exchange membranes 95
6.1.2. Gas permeable membranes 98
6.2. ASIC 100
6.2.1. Schematics 100
6.2.2. Layout 101
6.2.3. Temperature monitoring 102
6.2.4. ASIC implementation 104
6.3. Temperature dependency 107
6.4. Osmotic hydration sensor characterization & validation 108
6.4.1. Response time 109
7. Conclusions and future work 111
8. Outlook 115

1. Introduction

1.1. Motivation

Modern lifestyle is changing people's most basic habits such as excess eating, excess drinking and low physical activity (sedentary lifestyle) which has a detrimental impact on a person's health. It is commonly said that "water is equivalent to health", i.e, the consume of water helps keeping a good physiological balance keeping a good function of our cells and therefore, keeping an individual healthy. A disturbance in the salt concentration in the human body will trigger water diffusing into (overhydration), or out from (dehydration) the cell making them swell, or shrink, respectively. The salt concentration in the human body is proportional to the hydration level and, in case of a disequilibrium, complications can occur. For example, American football players lose an average of 1.2% body mass due to dehydration after each training session [1] and further studies have revealed that the heart rate increases by approx. 10 beats/min for every 1% loss of body mass [2]. In contrast, a 15% increase in water content (overhydration), could lead to a comparable serious condition known as hyponatremia or water intoxication [3-5]. Hence, it is extremely important to assess the hydration level but mainly for risk groups such as: patients in intensive care or suffering from a chronic illness that may disturb the electrolyte balance (e.g. kidney and heart diseases). Other groups include people undergoing a high continuous physical workout, soldiers operating in a hot environment, pilots, astronauts or high altitude climbers, where a low ambient pressure triggers a more rapid loss of water through evaporation/perspiration. Elderly people living at home may also be at risk (dehydration is a signature of dementia – forgetting to ingest food/water) and children with infectious diseases (stomach virus/diarrhea) due to a relative smaller body mass volume compared to adults.

The main solutes governing the electrolyte concentration originate from sodium chloride (NaCl) and potassium chloride (KCl) which dissociate in water to sodium (Na^+),

potassium (K^+) and chloride (Cl^-) ions. Since Na^+ is the main cation present in the body fluids (BF), its change in concentration will be used in this work as a reference for the events associated with de-, and over-, hydration.

Current methods for the detection of hydration include manual sampling and analysis of BF from saliva (viscosity), urine (conductivity/color) and chromatography [6-8]. Other techniques measure the impedance, and thickness, of the dermis layer (skin) by means of ultrasound or electromagnetic radiation [9-12]. Another possibility could involve tracers, such as deuterium oxide (D_2O), that is added to an ingested fluid and subsequently collected in blood samples to assess the integrated effects of gastric emptying and intestinal absorption [13]. These methods require a stationary instrument, combined with a high device complexity and a low sampling rate that can take days [14]. Hence, disruptive technological alternatives should aim for an autonomous hydration sensor that is able to track hydration continuously from an unobtrusive and small device. It should take advantage of the most recent technologies involving microfabricated sensors with an electronic interface based on deep sub-micron complementary metal–oxide–semiconductor (CMOS) circuits.

Biomedical sensors that measure physiological parameters in the human body can originate from microelectromechanical systems (MEMS) that are small enough to be integrated into wrist watches, skin patches or implantable devices. Such biomedical MEMS (or BioMEMS) have already been used in pacemakers, glucose monitoring devices oxygen sensors, heart rate and blood pressure monitors [15]. They have also been used to record changes in physiological parameters arising from traumatic events [16] or from drug therapies [17] which may require complex delivery patterns [18]. Ultra low-power integrated circuit interfaces are used to translate signals from the MEMS devices (i.e., physical, chemical, or biological) to an electronic parameter (voltage, current, resistive, capacitive or inductive) for signal processing. These circuit architectures push the power consumption down to the lowest reported figures known today in combination with a small circuit footprint [19]. These circuits are capable of obtaining comparable signal-to-

noise ratios (SNRs) to their macroscopic counterparts, and provide the users with smaller biosensors, but not without compromising the resolution and dynamic range.

It is presented in this thesis an osmotic hydration sensor (OHS) that makes use of the following available technologies for measuring hydration: membrane separation (semi-permeable), MEMS resistive pressure sensor, TSMC 90 nm processing technology and microfabrication techniques for substrate assembly and preparation/fabrication. In this way, this project has been divided in three main categories:

(i) The identification of a suitable semi-permeable membrane that could separate ions and therefore, provide us with an osmotic pressure (OP) signal proportional to the salt concentration/balance in the BF (hydration).

(ii) The design of the front-end interface for the OHS using a low power approach that could lead to an implantable sensor.

(iii) The Packaging process which included the design of the OHS in a biocompatible material (e.g., acetal copolymer) and the integration of the circuit on a silicon substrate followed by its encapsulation.

The membrane used will provide a physical separation between an external media and a cavity (reference chamber) containing a solution with a known salt concentration (reference) which induces an OP due to an osmotic flow (OF). This principle is governed by the difference in osmolarity between the reference electrolyte and the media salt concentration where only the solutes that are not able to diffuse across the membrane will contribute to an increase in the OP (Gibbs-Donnan effect) [20].

The MEMS resistive sensor is a Wheatstone bridge resistance sensor that will record the changes in pressure inside the sensor's cavity given by changes in the bridge resistance.

The TSMC 90 nm technology will be implemented in order to design/manufacture the circuit's interface schematics and layout using a low voltage approach. This technology uses polysilicon, instead of metal, for the transistor's gate.

Microfabrication techniques used include substrate preparation in a clean room and wire bonding of ASIC, and pressure transducer, pads to the substrate. The wire soldering for communication, and power, of the electronic interface was done using a low temperature solder (Rose's metal).

1.2. Hydration

The electrolyte balance of the human body is carefully controlled through a process known as homeostasis in order to maintain cell and organ function, which is essential to life. The homeostatic mechanism regulates the body fluid volume, the pH and the electrolyte concentrations, maintaining a delicate, and dynamic, balance which can be destabilized due to illness, intensive workout and tough environmental conditions such as: altitude, heat, humidity, etc. [21]. The electrolyte concentration in our BF is measured in terms of osmolarity, or osmolality, and are typical units for defining the osmotic strength (OS). This concentration will in a healthy person correspond to an OS of approx. 280-300 mOsm L^{-1} [22] and should remain constant within this range. The term osmolarity relates to the amount of osmotically active molecules (solute) and is measured in mOsm L^{-1} (milliosmoles per litre of solution). In contrast, osmolality (also a frequently used definition) is measured in mOsm Kg^{-1} (milliosmoles per kilogram of solvent).

These electrolyte solutes that are distributed throughout the BF can be divided up into two main categories; (i) the intracellular fluid (ICF) and; (ii) the extracellular fluid (ECF) [23]. The ECF include the interstitial fluid (fluid retained within the tissue matrix), plasma, lymph, blood and cerebrospinal fluid. The cell membrane (CM) separates the intracellular, from the extracellular, components and is permeable to water but relatively impermeable to ions where a change in the ionic concentration in the

intercellular media will be responsible for the variation in the osmolarity of the BF (ECF and ICF) according to the Gibbs-Donnan equilibrium principle [24]. This diffusion of water across the CM will change the OP inside the cell.

Euhydration is the equilibrium state, where a person in not de-, nor over-, hydrated [13]. The loss of water volume inside a cell can increase the concentration of the main ions (*hypernatremia*), such as Na^+, K^+ and Cl^-, while an increase in the water volume inside the cell will provoke a decrease in the concentration of Na^+ (*hyponatremia*). Both hypernatremia, and hyponatremia, conditions are sensed by osmoreceptors that are located in the hypothalamus region of the brain and can detect changes in OP that could lead to a swelling, or shrinking effect on living cells. If the OP variation inside the cells is too large, it can result in a cell rupture causing its death however, the real problem is that the swelling can also happen to the brain (encephalopathy) and, if left untreated, it can lead to the death of a person [24, 25].

The total body water (TBW) per weight percentage (wt%) for an adult male and woman is in average 58.3±6.7 and 48.5±8.6 [TBW wt%)] respectively [26]. About 2/3 of the TBW corresponds to the intercellular volume, whereas the remaining 1/3 corresponds to the extracellular volume. The human body can only withstand changes in hydration, corresponding to changes in the TBW of ±20%, before a person's death [5]. For this reason, it is important to measure, and control, the hydration level of the human body especially for risk groups prone to hydration deficiency.

1.2.1. Dehydration

Dehydration results from an excess loss of water volume in the human body which in turn causes an increase in the ionic concentration in the BF (mainly sodium, potassium and chloride). The most prominent physiological symptoms are: thirst, headache, dry skin, mouth dryness, decrease in the production of saliva, loss of appetite, tiredness, confusion and a decrease in urine volume (darker color). The water in our body is used to transport oxygen, nutrients and waste products (sustains life) where a large degree

of this water is lost during the day in form of insensible loss via skin and lungs (breathing plus perspiration), feces, sweat and urination. Even though food offers about 1/5 of the total daily intake of fluid, there is an excess of approx. 2-4 L of water that should be supplied by direct intake of fluid each day [27]. The amount of water required varies according to the following variables: age, activity level, weather conditions (temperature and humidity), altitude (air pressure), and water depravation. Dehydration is important to monitor because not only affects our physical, and psychological, performance but it can also lead to death in the most extreme cases if left untreated. For example: an osmolality increase of only 1% initiates the sensation of thirst, leading to an increase in fluid consumption.

There are three different types of dehydration: *hypotonic*/*hyponatremic* (loss of electrolytes, mainly Na^+), *hypertonic*/*hypernatremic* (loss of water), *isotonic*/ *isonatremic* (loss of both water and electrolytes). Hypotonic dehydration is not a consequence of dehydration itself but improper rehydration i.e., replacing lost fluid by plain water without sodium. Throughout this manuscript, it is referred to hypotonic dehydration as *overhydration*.

1.2.2. Overhydration

Overhydration, also known as water intoxication or dilutional hyponatremia or hypotonic dehydration, can originate from an excess water intake that affects the electrolyte balance. For example, one can refer to overhydration as a serious state of hyponatremia that induces a much lower Na^+ concentration because of the excess of water intake that diffuses into the cell leading to a cell malfunction and, if not treated, it could swell until rupture causing the death of a person. For example, hyponatremia can result in seizures and the rate of rehydration can be very important to control in order to avoid serious complications such as cerebral edema.

Overhydration can also originate from heart illnesses, medication (diuretics) but also from exercise rehydration [28, 29]. For example, athletes are encouraged to ingest large

quantities of water in order to prevent dehydration which would affect their physical performance during the exercise, game or competition. In some cases, athletes are even encouraged to initiate a physical activity from a state of overhydration. It is here referenced exercise rehydration as an example of overhydration, also known as hyponatremia of exercise [29-31]. Rehydration during, and after, surgery is also important however this might be closely monitored through the urine color during the procedure or at the Intensive Care Unit (ICU). If an athlete, ingest sodium (chloride) free water after his training to compensate for the loss of water (but not the loss of electrolytes), he/she will most likely go into a state of hyponatremia because [Na^+] is lower than average provoking a water diffusion from the extracellular to the intracellular *milieu* increasing the cells volume (swelling).

1.3. Measuring hydration and current state-of-the-art

Both hypertonic dehydration and overhydration translate in a decrease, and increase, in the plasma volume (PV) respectively which results in changes of the ICF and, consequently, in the TBW due to the water diffusion from the intercellular, to the extracellular, region [27]. Changes in the TBW result in changes of the salt concentration in the human body that affect the OS of the BF, measured in terms of *Osmolarity or Osmolality*. The hydration sensor here presented will detect changes in the BF's OS.

The water exchange methods/rates in the human body are presented in figure 1. The method used to assess a person's hydration in a clinical setting was developed in 1975 by Grant and Kubo [32]. They used three different categories: (i) laboratory tests (serum and urine osmolality, sodium concentration, etc.); (ii) objective non-invasive measurements (body mass, water intake and output, heart rate, etc.); and (iii) subjective observations (skin turgor, thirst, etc.) [13]. Some of these measurements used to assess the level of hydration are still used today, mainly the body mass method.

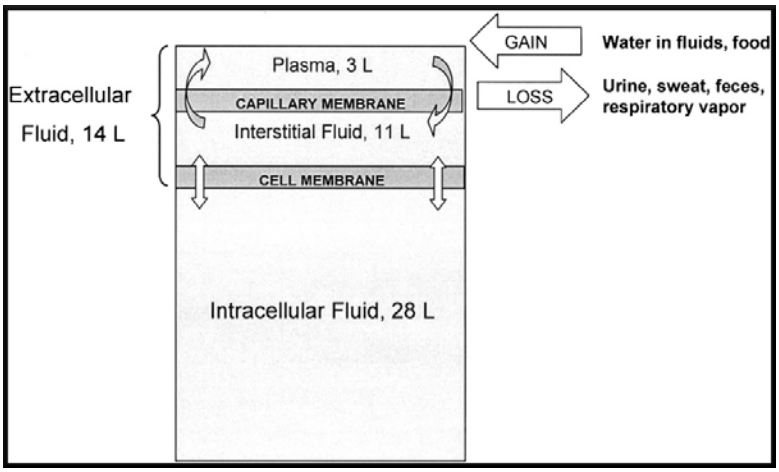

Figure 1: Schematic representation of the TBW of a human body weighing 70Kg. The 42 L of TBW are comprised in different body fluid compartments together. Fluid gain, and loss, sources are also represented according to [14].

Armstrong concluded that it is not possible to assess the complete level of hydration, and that there is a need for an “elusive gold standard” that corresponds to the TBW under controlled conditions [14]. This means that by controlling the experimental, postural, exercise, dietary, and environmental factors, the TBW, volume of body fluid compartments, and extracellular fluid concentration may stabilize and equilibrate [14, 23]. Hence, his “gold standard” constituted a method based on isotope dilution and neutron activation analysis, but the use of laboratory facilities with highly controllable settings and an equilibrium time of approx. 5 h has made his method impracticable for everyday life. Furthermore, the BF are rarely stable during daily activities. Armstrong has also described this and other methods during his review in [14, 23] (Table I)t that are still used today.

Table I: Methods of assessing the level of hydration according to Armstrong [14, 23]

Technique	***Body fluids involved***	***Time required***	***Portability***	***Probability of adverse effects***	***Description***
Stable isotope dilution	All (ECF and ICF)	Much	Not portable	High	Oral or intravenous administration of a tracer substance, before and after sampling a body fluid or expired air, enables measurement of human fluid compartment size.
Neutron activation analysis	All	Much	Not Portable	Moderate	A specimen is irradiated in a nuclear reactor, producing specific radionuclides that emit characteristic gamma rays during decay. Requires radiation detectors.
Bioelectrical impedance spectroscopy (BIS)	Uncertain	Much	Moderate	Low	Resistance of body tissues and water to electric current. BIS is a statistical technique that extrapolates values for resistances at very high and very low frequencies from resistance values in the frequency range that is reliable (i.e., 1–500 kHz).
Body mass change	All	Little	Portable	Low	Measurement of body mass at a caloric balance over a period of 1-4 hours with, or without, exercise.
Thirst rating	Hypothalamus	Little	Portable	Low	The sensation of thirst can be used to announce the threshold of hypohydration that affects physiological responses and health.
Plasma Osmolality	ECF	Moderate	Not portable	Moderate	Direct laboratory measurements of plasma osmolality are performed with either a freezing point or vapor pressure depression osmometer.

% plasma volume change	blood	Moderate	Not portable	Moderate	Dye dilution method technique [33] to assess the change in color of a known volume with blood.
Salivary flow rate, osmolality, total protein	Whole, mixed saliva	Moderate	Moderate or Not portable	Low	Measuring the saliva volume, density and solute content gives an indication of the electrolyte balance, or misbalance, in the body.
Urine osmolality	Excreted urine	Moderate	Not portable	Low	A measure of the total urine solute content.
Urine specific gravity		Low	Portable	Low	Urine density (m/V) is compared with pure water.
Urine Conductivity		Moderate	Not portable	Low	Measuring the urine conductivity, using two electrodes, gives an indication of the electrolyte body balance.
Urine Color		Low	Portable	Low	Simple investigation of the urine color and classification accordingly.
24h urine volume		Low	Portable	Low	Comparison of urine volume with the one from healthy individuals.

Osmolality is used in Table I as a unit of measurement instead of osmolarity however, both terms go hand in hand as a measuring unit of the OS where, osmolarity, is more commonly used *in vitro*. Throughout this work we refer to a solution's OS as osmolarity, instead of osmolality, since this is a more correct unit for our application/validation and both osmolarity, and osmolality, are interchangeable when referring to *in vitro* solutions [34].

From Table I, it is difficult to claim which techniques are better since these depend on unique individuals and situations. Most of these techniques require a high technical expertise by the operator.

1.4. MEMS applications in biomedical sensors

Silicon microfabrication has been long used to support new medical procedures, new analysis techniques, but also to monitor physiological changes in the human body that can indicate an organism/body "malfunction".

MEMS transducers designed to record physical environmental parameters such as, pressure, temperature, acceleration, rotation, mass change and light are becoming particularly important in biomedical applications where they would form the core of wearable or implantable devices that monitor key physiological parameters related to performance (mental and physical) or a specific disease condition as part of a therapeutic regime [17, 35]. For example, MEMS pressure sensors have been used in non-invasive equipment since 1985 such as respiratory pumps and blood pressure cuffs [36]. More recently, pressure sensors have been integrating invasive equipment such as, for example, catheter tip sensors [37]. Other recent examples can be endoscopic pills [38] integrating pH and temperature transducers, besides a CMOS camera, as well as new retinal implants with light sensitive CMOS pixels devices [39-44].

Transducers (sensors) can be active or passive depending on what their function is: An active sensor simply converts the ambient physical variable monitored directly to a

corresponding electrical signal whereas, a passive sensor, converts the ambient physical variable monitored into a variable impedance, such as capacitance, inductance or resistance. For example, a pressure transducer based on a Wheatstone bridge resistance is converting the environmental pressure changes into a variable resistance that can be transformed, and amplified, into a voltage, or current, signal through an electronic front-end interface.

In the seventies, Stanford University developed the first silicon based microelectrode arrays for neural recording and stimulation while, in the eighties, new efforts in the development of small size and low cost sensors led by companies such as Lucas Nova Sensor, and Motorola) resulted in, created the first disposable blood pressure monitoring sensors/kits [45]. More recent advances have led to have led to further advances with applications in biochemistry and medical diagnostics such as, for example, polymerase chain reaction (PCR / DNA amplification) on a silicon die and novel DNA techniques. This has been possible by borrowing the integrated circuit techniques to develop and produce MEMS devices and transducers in an ever smaller size, and consequently, larger volumes and lower costs.

The two largest market segments for MEMS devices products are pressure sensors and accelerometers [45]. Most of the MEMS products nowadays are built utilizing microfabrication techniques such as bulk micromachining and anisotropic etching solutions. Most of the implemented pressure transducers, and accelerometers, used nowadays are based on piezoresistive resistors, such as the pressure transducer we use in the hydration sensor presented in this thesis.

1.5. Membrane bounded microsystems for separation processes

A synthetic membrane is a physical structure created for separating, or retaining, constituents present in a solution through a process known as filtration. They can be made of organic, or inorganic, materials but the most common synthetic used membranes are made of polymeric structures.

Modern membranes are technologically advanced products used in the industry and science [46]. Membranes have been used to produce freshwater by filtering out the salts from seawater in order to generate an uninterrupted water supply for mankind, reclamation and the reuse of raw wastewater [47]. There is a lot of potential in combining membranes with biological processes (*bioprocessing*) such asthe concentration and purification of macro- and micro solutes or the increase in concentration of a biocatalystwhich will increase the volumetric productivity of a reactor and reduce subsequent recovery requirements [48].

One can think of filtration as a pressure driven process which removes particles (*retentate/concentrate*) selectivity from a fluid (*feed*) by passage through a semi-permeable membrane (allows the passage of a solvent but retains solutes/particles). The properties governing the permeability behavior of a membrane to a given solvent (*permeate*) may depend on its phase (liquid or vapor), as well as the electrical, physical and chemical properties. Membrane processes are classified into ultrafiltration, microfiltration, nanofiltration and Reverse Osmosis (RO) depending on the pore size (solute retention) in which RO membranes have the smallest (figure 2).

Membrane processes have been playing a critical role in the purification of biotechnology products for the last few decades [22]. The mass transfer across membranes is provoked by solute concentration (steady state conditions), or pressure, differences across the membrane. However, while pressure-driven processes include ultrafiltration, microfiltration, nanofiltration and RO that mostly use liquid semi-

permeable membranes (allows passage of a liquid permeate), it is important not to exclude other membranes that can have a very high selectivity, such as ion-exchange and gas separation membranes.

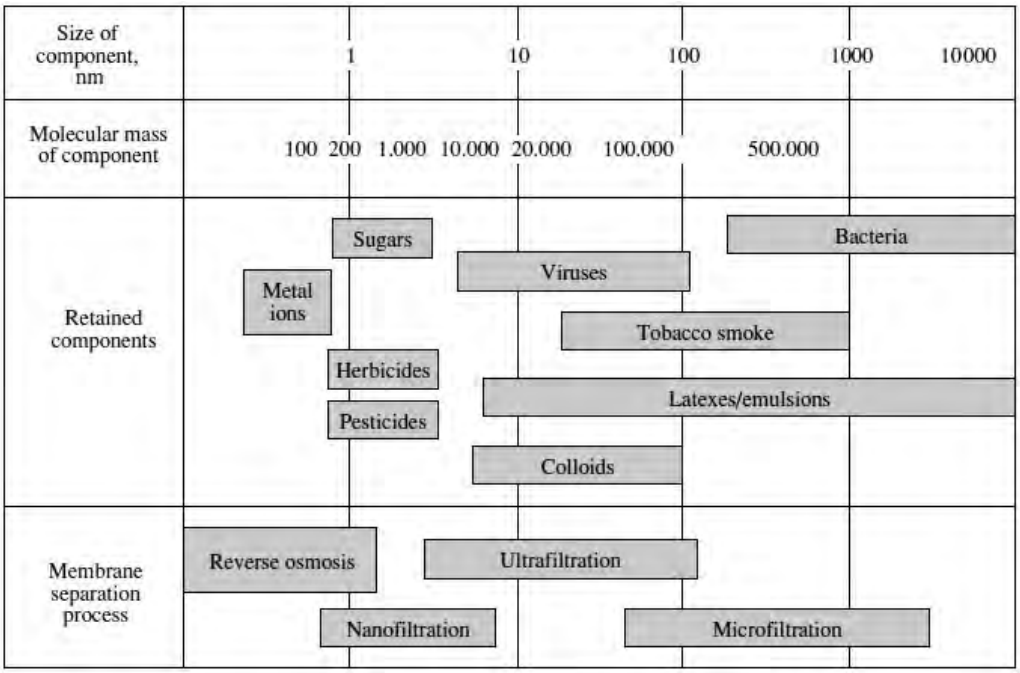

Figure 2: Filtration spectrum, Volvok et al. [45].

From figure 2 one can see that the size of the solute that is being retained classifies the membrane type, i.e., membranes are classified according to their pore size or nominal molecular weight cut-off (MWCO) which can be defined to be 90% retention of a given solute after filtration. [49]. The selectivity, S, of a specific membrane can be given by (1) [50]:

$$S = \frac{C_f}{C_F} \qquad (1)$$

where C_f and C_F are the solute concentrations in the filtrate and feed solutions, respectively. The permeability, detention capability, process flux and process capacity characteristics of a membrane characterize the operation capability of a given microsystem, implantable or not. There are other separation processes that need other membrane technology applications. These major separation processes can be: dialysis, electrodialysis, Donnan dialysis or membrane bioreactor.

The structural fabrication processes can be: air casting, immersion casting, melt casting, track-etching, stretching and radiation-induced polymerization. Casting can also be performed using another membrane as a substrate originating composite membranes [50]. The development of the fabrication methods for membranes allowed for the manufacturing of two types of membranes: ceramic and polymeric. The development of polymeric membranes has contributed to an increase in the biocompatibility of the membranes if one thinks of an implantable membrane bounded microsystem sensor. Polymers surface properties facilitate the adsorption of proteins creating an adsorbed protein layer that will influence the subsequent biological reactions fouling the immune system (section 1.6) [51].

1.5.1. Membrane structures

The main type of membrane structures can be classified as follows (figure 3):

- *Isotropic membranes* - Uniform pore structure throughout the thickness of the membrane. Larger probability of concentration polarization (solute concentration gradient affecting the membrane permselectivity) at the membrane surface however, high levels of clearance (low resistance to solute diffusion through the membrane) may easily be achieved.

- *Anisotropic membranes* - Known by its graded pore size distribution, normally present a smaller pore size in the upstream side protecting the downstream

side pores from blockage. It is useful for streams worth relative homogeneous particle size distribution.

- *Composite membranes* - When two different types of membranes are combined together, normally isotropic with anisotropic. Gives freedom of designing different feed streams. First layer can be used as a pre-filter.

- *Multi-layer membranes* - Similar to composite membranes, its advantages are in the physical bonding of two different membranes together. First layer normally used as a pre-filter.

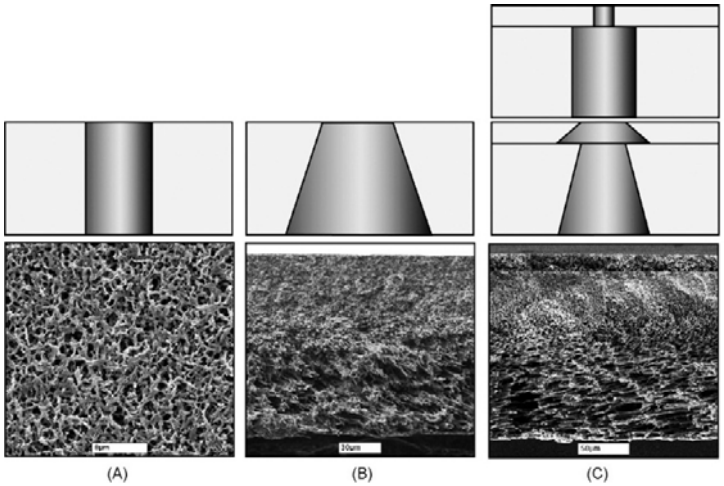

Figure 3: Cross-sectional view of sterile filters developed for the biotechnology industry using multiple composite membranes with varying pore size distribution (A) isotropic to (B) anisotropic to (C) composite. Scanning electron micrographs from Millipore Corporation [52].

Other sources such as for example, S. P. Nunes and K. V. Peinemann [52], may simplify membrane's structures according to figure 4.

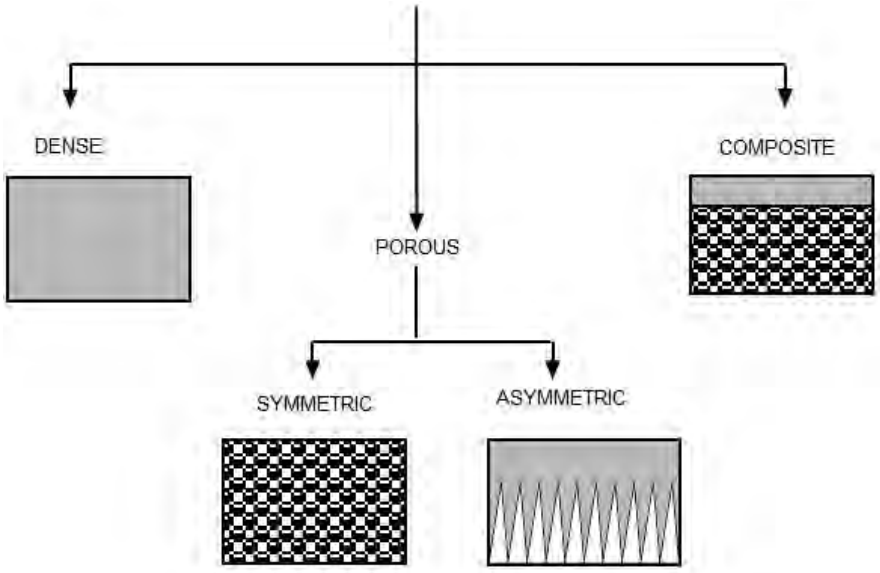

Figure 4: Membrane classification according to the morphology [52].

From figure 4 one can classify the membranes as being dense, composite or porous. While separation by dense membranes relies on physicochemical interaction between permeating components and the membrane material, separation by porous membranes is achieved by size exclusion, where the rejected material can be dissolved or suspended depending on its size in regards to the size of the pore [47]. Table II gives a general overview of the different membrane formation possibilities.

Table II: Membrane compositions [53]

Membrane formation	***Membrane material***	***Description***
Membranes derived from microporous media	Ceramics, Sintered metal, Sintered polymers, Wound wire or fiber	Assembly of small particles laid down or sintered with pores formed from interstices between the solid particles
Membranes derived from homogeneous solid films	Track-etched membranes, Stretched polymers, Aluminum derivatives, Dense films	Stretched polymers perpendicular to the axis of a crystallite orientation (Semicrystalline polymers)
Membranes derived from heterogeneous solid films	Leached glasses, Extracted polymers	Metals made into membranes by selectively dissolving one phase
Symmetric membranes derived from a solution	Leached membranes, Thermally inverted solutions	Preparation of a concentrated solution of a Polymer in a solvent and thermal precipitation
Asymmetric structures derived from solution	Loeb-Sourirajan membranes [54]	Also named as skinned membranes, they divide two necessary functions of a membrane (Separation and Support layers)
Asymmetric composite structures	Dynamic membranes, Thin film composites, Coated structures, Self-assembled structures	Membranes used as a substrate to provide an extra uniform pore size distribution

Membranes are usually made from natural or synthetic polymers such as cellulose acetate (CA), polyvinylidene difluoride, polyamide, polysulfone, polycarbonate, polypropylene, and polytetrafluoroethylene (PTFE). Newer membranes can also be ceramic based on alumina (formed during the anodizing of aluminum) carbon and glass. Other membranes can be made of metals such as, stainless steel, silver, gold, platinum and nickel [47]. Membranes can present different configurations based on the

geometric form given to synthetic membranes. The main configuration modules are: tubular elements, hollow fiber (or capillary fiber), plate-and-frame element, spiral wound and flat sheet.

In the purpose of this thesis research, flat sheet membranes will be considered only. These are easier to implement in the prototype hydration sensor here presented. This way, it will also be easier to achieve a good reproducibility for the experiments since all membranes will have a similar aspect ratio, i.e., flat sheet membranes have a high surface area/volume ratio.

1.5.2. Membrane characteristics

All types of membranes are classified according to their solute retention capabilities. In a membrane bounded microsystem for filtration of a solution, one can define three streams: the feed, the permeate and the concentration of retained solute/particles (retentate). In most processes, the membranes are permeable to water, or water vapor if considering gas permeable membranes. Liquid mixtures can be separated by pervaporation where the permeated product is removed in the vapor state on the permeate side of the membrane. While the mass transport through porous membranes is mainly done convectively (Darcy's law), the transport through dense polymeric membranes can be described through different diffusion mechanisms. However, both transport mechanisms occur side-by-side.

In The diffusion mechanisms through polymeric membranes illustrated in figure 5 can be divided into 4 categories: The viscous, or bulk, flow; the Knudsen flow, the molecular sieving flow and the solution-diffusion model [55]. The flow/diffusion mechanism for the molecules through a membrane depends on the pores' size in regards to the mean free path. Both viscous, and Knudsen flow explains the transport of the molecules through the membrane pores:

- Viscous, or bulk, diffusion, that takes place for very large pores where the flow is inversely proportional to the viscosity of the liquid/gas.

- Knudsen diffusion holds at very low pressures where lighter molecules move across faster in the stable larger pores (capillary forces quantified by Darcy's law). Molecules smaller than the mean free path.

- Molecular sieving is a selectivity model where the pores' size does not allow the passage of a solute. This model provides different membrane classifications according to their filtration capabilities as it has been previously explained in section 1.5.

- Solution-diffusion is used in dense polymeric films and is described in this section.

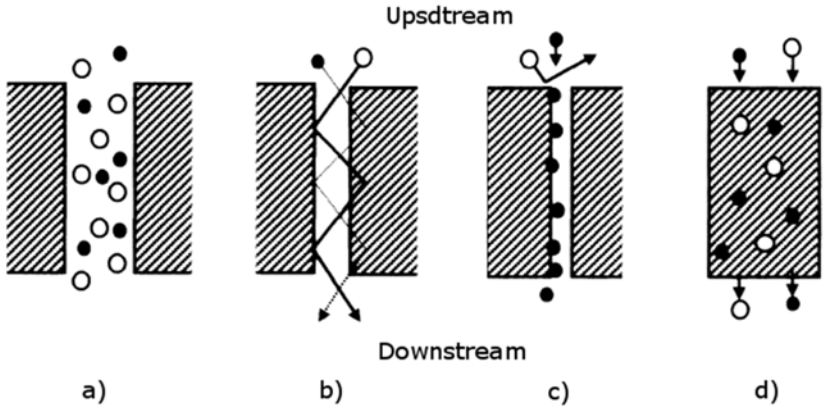

Figure 5: Mechanism of flow of gas molecules: a) viscous, or bulk; b) Knudsen; c) molecular sieving and d) solution-diffusion [55].

The Permeability (P), Diffusivity (D), and Solubility (S) of a gas or solute through a polymer depends on the following factors: the molecular size, and physical state, of the diffusant; the morphology of the polymer; the compatibility or solubility limit of the

solute within the polymer matrix; the volatility of the solute and finally, the surface or interfacial energies of the monolayer films [56].

In 1855 Fick proposed a law of mass diffusion where “the rate of transfer of diffusing substances through unit area of a section is proportional to the concentration gradient measured normal to the section”. Fick’s first law of diffusion is mathematically expressed as [56-58]:

$$J = -D\frac{\partial C}{\partial x} \tag{2}$$

where *J* is the rate of transfer per unit area of section (mol m^{-2} s^{-1}), *C* (mol cm^{-3}) is the concentration of diffusing substances, x is the space co-ordinate measured normal to the section and *D* is the diffusion coefficient (m^2 s^{-1}). Once the mass-balance of an element is taken into account, equation (2) can be used to derive the fundamental differential equation of diffusion:

$$\frac{\partial C}{\partial t} = D\left(\frac{\partial^2 C}{\partial x^2} + \frac{\partial^2 C}{\partial y^2} + \frac{\partial^2 C}{\partial z^2}\right) \tag{3}$$

The diffusion coefficient in polymeric and non-homogeneous systems varies from point to point and equation (3) becomes:

$$\frac{\partial C}{\partial t} = \frac{\partial}{\partial x}\left(D\frac{\partial C}{\partial x}\right) + \frac{\partial}{\partial y}\left(D\frac{\partial C}{\partial y}\right) + \frac{\partial}{\partial z}\left(D\frac{\partial C}{\partial z}\right) \tag{4}$$

Diffusion is normally restricted to one direction only and equations (3) and (4) become (5). This process is also known as Fick's second law of diffusion:

$$\frac{\partial C}{\partial t} = D\frac{\partial^2 C}{\partial x^2} \tag{5}$$

Important membrane specifications that can influence the choice of the most appropriate membrane for the intended separation/function are: mechanical strength, temperature tolerance, chemical compatibility, hydrophobility, hydrophilicity, permeability, selectivity (permselectivity) as well as manufacturing cost [47].

1.5.3. Porous and composite membranes

According to figure 2 different filtration processes can be obtained based on the pore size of membranes. For example, Microfiltration (MF) membranes are usually used in processes that remove micron-sized particles from fluids and has pore sizes ranging from 0.1 to 10 µm. Ultrafiltration (UF) membranes are capable of retaining solutes in the range of 10 to 1000 Å. Nanofiltration (NF) membranes can already separate particles such as bacterias, proteins, etc., with a molecular weight larger than 1000 Da. As a more selective membrane one can think of Reverse Osmosis (RO) membranes that have the smallest pore structure, with diameters ranging approx. 5 to 15 Å [47].

RO membranes fall into two categories: asymmetric membranes containing one polymer, and thin-film composite membranes consisting of two or more polymer layers [59]. Asymmetric RO membranes present a very thin permselective skin layer (0.1 to 1 µm thick) supported on a more porous sublayer of the same polymer where the sublayer works only as a porous mechanical support of the selective skin layer. It presents the advantage of concentrating salts and chemicals with low-pressure requirements however, has the disadvantage of easily getting suspended particles on the feed side making it hard for the particles to go through the membrane.

Track etched membranes (TM) play an important role in biomedical applications due to their very narrow pore size distribution and biocompatibility. These type of membranes are based on a solid polymer structure that is made porous by a process known as nuclear tracks etching [46]. Dependent on the track etching protocol, TM will offer pore geometries ranging from cylindrical, to conical, funnel-like and cigar-like [60]. There are two methods for producing latent tracks in foils to be transformed in porous membranes: irradiation with fragments from the fission of heavy nuclei such as, for example, 235U and chemical etching where the damaged zone of a latent track is removed and transformed into a hollow channel forming a pore [45]. Chemical etching is what determines the pore size, and shape, by controlling two parameters: VB (bulk etch rate) and VT (Track etch rate). Some particular polymers for the TMs production are polyethylene terephthalate (PET), polycarbonate (PC) and polypropylene (PP).

Track etched membranes are mainly used for two types of separation methods: In the absence of a surface adsorption process, the membrane acts as a "screen" retaining particles that are smaller than the pore [46]. In the presence of a surface adsorption process, the retention of particles depends on the nature of the surface of the membrane (permselective layer) and the nature of the particles such as, for example, polarity and size. In addition, other factors can also influence the retention of particles such as pH, presence of surfactants, etc., decreasing the filtration rate.

For steady a state condition, Fick's second law [equation (5)] is given by:

$$\frac{\partial^2 C}{\partial x^2} = 0 \qquad (6)$$

The concentration changes linearly from C_1 to C_2 through a plastic sheet or membrane and the rate of transfer for a diffusing substance is the same across all sections.

$$J = -D\frac{\partial C}{\partial t} = \frac{D(C_1 - C_2)}{l} \quad (7)$$

where *l* (cm) is the membrane thickness.

1.5.4. Ion-exchange membranes

Ion-exchange membranes can be classified as cation-exchange or anion-exchange depending on the type of ionic groups fixed to the membrane backbone. Cation-exchange membranes present negatively charged groups ($-SO_3^-$, $-COO^-$, $-PO_3^{2-}$, PO_3H^-, $-C_6H_4O^-$, etc.) allowing the passage of cations and rejecting anions. The opposite can be achieved with anion-exchange membranes containing positively charged groups ($-NH_3^+$, $-NRH_2^+$, $-NR_2H^+$, $-NR_3^+$, $-PR_3^+$, $-SR_2^+$, etc.). Ion-exchange membranes can also be classified as homogenous and heterogeneous according to their chemical structure where the charged groups can be chemically bounded to or physically mixed with the membrane matrix, respectively [61].

1.5.5. Gas permeable membranes

Transport of gases through a dense polymeric membrane is usually described by a solution–diffusion mechanism that consists of three steps:

- The adsorption on the upstream side of the membrane (sorption).
- The diffusion through the membrane.
- The desorption, or evaporation, on the downstream side of the membrane.

The solution-diffusion mechanism is a result of a concentration gradient between the two sides of the membrane [62]. In systems where a gas or vapor is the diffusant, the surface concentration may not be known. In gas and vapor systems, the rate of diffusant transfer is expressed in terms of vapor pressures, p_1, p_2, by equation (8), according to Crank [63]:

$$J = P\frac{p_0 - p_1}{l} \tag{8}$$

where *P* is the permeability coefficient ($cm^2\ s^{-1}\ Pa^{-1}$). According to the solution diffusion model, the permeability through a dense membrane can be defined by:

$$P = D.S \tag{9}$$

where *S* represents the solubility coefficient [cm^3 (at 273.15K; $1.013.10^5$Pa) $cm^{-3}\ Pa^{-1}$]. Both the diffusion and the solubility coefficients are dependent on the temperature, where the diffusion increases and the solubility decreases with temperature respectively.

Transport properties in polymers are sensitive to the amount of free volume in the polymer matrix. The amorphous density data were used to estimate the fractional free volume (FFV) of the amorphous phase using the following group contribution method [64]:

$$FFV = \frac{V - V_0}{V} \tag{10}$$

where *V* (cm^{-3}) is the specific volume of the amorphous polymer at the temperature of interest and *Vo* is the specific occupied volume at 0 K.

1.5.6. Membrane drawbacks

Important drawbacks for membrane separation processes can be: *fouling*, *membrane contamination*, *sterility*, and *flexibility*.

The filtration capabilities of a membrane degrade over time due to fouling and concentration polarization effects [50]. *Fouling* occurs from the adsorption on, or within, the membrane pores forming a deposit on the external surface of the membrane (pore blockage). When fouling occurs a *concentration polarization* arises leading to a complete, or partial, accumulation of solutes at the upstream surface of the membrane constraining the bulk mass transfer. Equation (11) is giving the relation between the ratio of the membrane area fouled with particles to area of clean pores and the dimensionless filtration time, t_f:

$$t_f = \gamma . n . \int_0^t \frac{dV}{dt} \tag{11}$$

where *γ* is the ratio of the pores area to the total membrane area, *n* represents the number of particles per unit volume of the feed and *V* is the permeate volume (cm^3) [65]. For pressure driven separation methods, there are techniques to control fluid flow characteristics (avoiding fouling) such as: high shear rates in tangential flow filtration modules or inducing a secondary flow involving Taylor or Dean Vortices.

In dense membranes, it can occur *membrane contamination* from other molecules, or ions, replacing the main component forming the backbone of the membrane. For ion-exchange membranes, it can change its conductivity properties leaking undesirable ions

and, for gas permeable membranes, it can lead to a leakage occurring from an increase in the FFV.

Sterility is also a challenge associated to the use of membranes in bounded microsystems due to thermal expansion of various membrane materials that increases the voids in the membrane structure.

Also, membrane *flexibility* (it is very difficult to produce rigid membranes) can add errors to a microsystem when measuring, for example, osmotic pressures (OPs). The membrane deformation would affect the volume and therefore, the pressure.

An important remark should be made to the possibility of fabrication faults (lack of accuracy) that can produce non-ideal pore sizes, and pore distribution, which may result in a leakage in the system.

It is said that a membrane system capacity/life spam is defined by the volume of feed that can be processed per unit membrane area before the membrane must be regenerated or replaced [50]. This is not ideal for separation systems that include membranes such as, for example, implantable microsystem, where there will be a need for extra medical intervention in order to replace the membrane, or implant.

1.6. Packaging Challenges

There are several factors that one need to consider when packaging a biomedical implant [66]. These are: Moisture protection, impermeability to water vapor, adhesion, metallic corrosion and polymeric degradation, thromboresistance, sterilization, rigidity, weight, size and shape, fixation (migration of implant should be avoided), mechanical stability, electrical stability and thermal stability. The external packaging of an implantable medical device helps absorbing mechanical stresses on the device (could be muscle contractions) but it also prevents corrosion, toxic leakages, degradation, calcification and embrittlement [67]. For this reason, standardization of medical devices

has been implemented in order to protect the end user. This is a quality measure implemented by the ISO 14708 for active implantable medical devices, and ISO 10993 for biocompatibility of medical devices, that comes under the standard IEC 60601 for the safety and effectiveness of medical electrical equipment, published by the International Electrotechnical Commission. Most of the requirements here described can be "tackled" using a hermetic package that protects the sensor from the outside environment, property known as hermiticity. However, some of these properties are not attenuated by using a package that hermitically seals the sensor and have to be considered during sensor development such as:

- Rigidity, size and shape could originate wounds associated to movement/muscle contraction and giving origin to an inflammation.
- Weight, can be uncomfortable for the end user.
- Mechanical, Electrical and thermal stability for a correct measurement of the physical property being monitored (noise reduction).
- Fixation, part of the surgical procedure this is a very important factor since it could be life threatening.

Even though the sensor presented in this manuscript is a *proof.of-concept* device for *in vitro* measurements/validation, it is important to show the risks, and requisitions, for an implantable device as later one would like the OHS to be. There are two packaging requirements that are considered to be of great importance for a biomedical implant: (i) hermeticity and (ii) biocompatibility.

1.6.1. Hermeticity

Hermeticity can be defined as "the state or condition of being airtight" or "sealed so that the object is gas tight." In reality, it is impossible to accomplish an absolute or complete hermeticity because all materials are gas permeable to some degree [68].

Hermeticity provides the necessary protection of the implant from, for example, moisture diffusion that may damage the electronics by creating short circuits due to humidity increase, or damaging the solder contacts due to oxidation. The choice of biocompatible materials will reduce the rejection mediated processes instigated by the immune system, as well as making the implantable device non-toxic and less dangerous to use. The packaging of sensors in the human body, has to take into consideration several aspects addressed in the sections below [69].

1.6.1.1. Biological hermeticity

Packaging acts as a biological barrier between the body, and internal electronics, and helps against mechanical stresses applied, keeping its integrity. It is important to protect the electronics inside the device from the BF as well as to avoid leakage from the internal composites of the device. An implantable device needs to be hermetically sealed which can be tested for a package that is in the presence of a helium flow at 20 °C with 1 bar differential pressure, then the diffusion flow rate should be below 10 - 8 cm^3 s^{-1}. Hermetic sealing can be used to seal a variety of surfaces including metals, polymers, plastics, alloys, ceramics, etc. using techniques such as: welding, soldering, etc. [70].

1.6.2. Biocompatibility

Biocompatibility is “the ability of a material to perform with an appropriate host response in a specific application” [51]. If the tissue does not change the material properties within the design specifications, then the material may be considered biocompatible.

Biomaterials used for packaging of implantable sensors should be non-inflammatory, non-toxic, non-allergenic, non-carcinogenic and, when located inside the blood stream, non-thrombogenic [71]. Moreover, the implant function needs to be resistant to the surrounding tissue, Biofouling [72]. For a long time it was believed that a biological inert material would minimize the host response by avoiding cell-material interactions.

However, further studies suggest that permitting specific cell responses may be beneficial for the biomaterial integration in implants. The material surface treatment (physical or chemical coating) can improve the implant integration such as, for example, the osseointegration of titanium implants will allow the migration and adhesion of bone-forming cells from the surrounding tissues onto the implant improving the integration of the material and increasing the body healing comprehension [73]. Therefore, the study of biomaterials is important in order to modulate immune cell function appropriately. Strategies of the design of biomaterials include alteration of material surface properties either passively via physiochemical features or actively with molecules or matrices designed to systematically target cell behavior. The choice of a biomaterial is a process with tradeoffs where the purpose of the encapsulated device needs careful evaluation. There are four main classes of materials to be used in the human body according to Table III.

Table III: Class of materials used in the human body according to "Biomaterials: An introduction" [67]

Material	***Advantages***	***Disadvantages***	***Examples***
Polymers (nylon, silicone rubber, polyester, polytetra fuoroethylene, etc.)	Resilient, Easy to fabricate, Low cost	Not strong, deforms with time and may degrade	Sutures, blood vessels or other soft tissues, hip socket, ear, nose
Metals (Ti and its alloys, Co-Cr alloys, Au, Ag, stainless steels, etc.)	Strong (tough ductile)	May corrode, dense, difficult to make, expensive	Joint replacements, dental root implants, pacer and suture wires, bone plates and screws
Ceramics (alumina, zirconia, Calcium phosphates including hydroxyapatite, carbon)	Very biocompatible	Brittle, not resilient and weak in tension	Dental and orthopedic implants
Composites (carbon-carbon, wire or fiber reinforced bone cement)	Strong (tailor made)	Difficult to make	Bone cement, dental resin

1.6.2.1. Host Tissue responses towards implantable biodevices

The surgical procedure involved in the implantation of a physical device causes injury to the tissue, that originates an inflammatory response (wound healing) that starts with the formation of an extracellular matrix around the implant, more precisely around the encapsulation/packaging of, for example, a sensor [74]. The material alone may also trigger immune reactions in addition to the wound healing. The material is either accepted by the body, in which case a thin fibrous envelope surrounds the implant (extracellular matrix), or any illicit response may arise resulting in an inflammation of the tissue in cause. There are two main types of host tissue responses that can be outlined according to Franz et al. [73]:

- Onset of the inflammatory response: blood proteins and alarmins induce granulocyte/monocyte activation.

- Coagulation, complement and adhesion proteins - signals for integrins.

In figure 6, one can see that after the implant is inserted in the tissue, proteins adsorb to the biomaterial surface initiating an immune response that activates polymer-phonuclear leukocytes (PMNs), monocytes and resident macrophages. Signals are released from the injured tissue enhancing the activation and priming of PMNs which triggers an inflammatory response. The release of enzymes and ROS (Reactive Oxygen Species) from PMNs will corrode the bio- material surface exposing the sensor. These tissue responses describe a natural process that will always occur whenever a foreign body is implanted in a human and it is a phenomenon that is still not completely understood. Macrophages are the driving force of chronic inflammation according to figure 6.

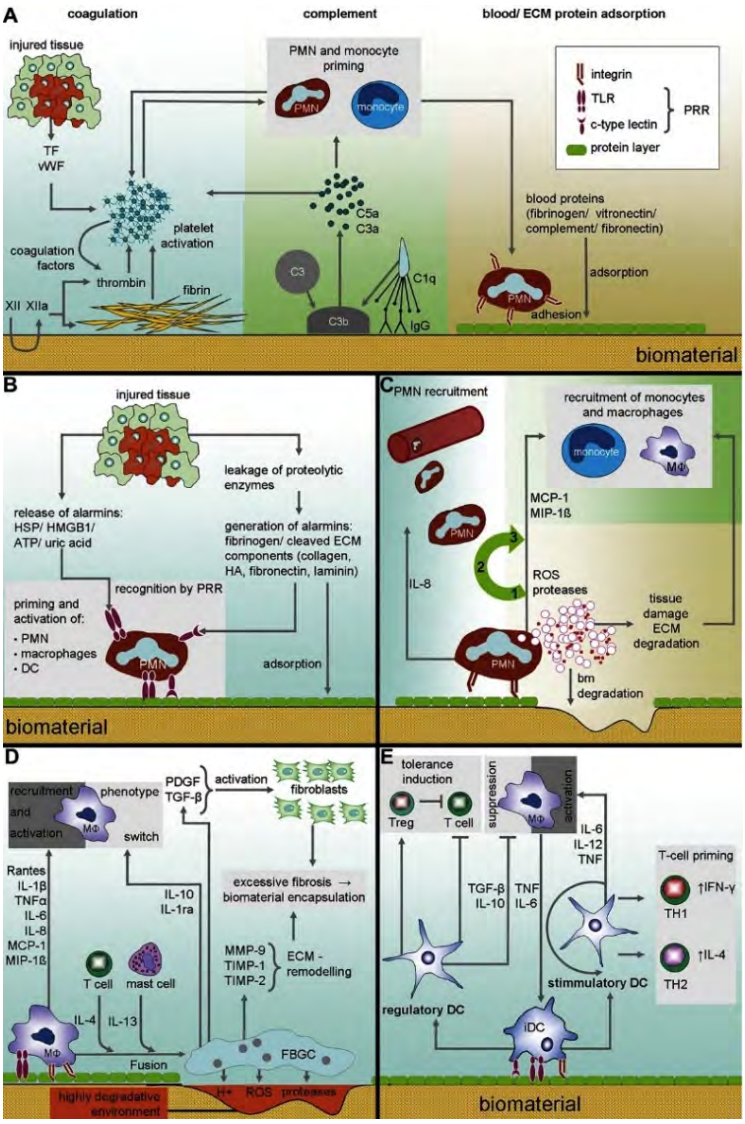

Figure 6: Immune response towards biomaterials; A) Adsorption of blood proteins (activation of the coagulation cascade) activating PMNs, monocytes and macrophages. B) Danger signals (alarmins) released from damaged tissue for an enhanced function of the immune system via PRR engagement. C) The acute inflammatory response is dominated by action of PMNs that secrete proteolytic enzymes and ROS, corroding the biomaterial surface. D) Macrophages attached to the biomaterial can foster invasion of additional inflammatory cells by secreting chemokines. E) Stimulus type mature DCs to either immunogenic or tolerogenic subtype [73].

1.6.3. Electrical compatibility

Electrical compatibility is more related to EMI (electromagnetic interference) that can be caused by other electrical devices. It is very important that, for example, a pacemaker does not suffer from any interference since it could cause cardiac dysrhythmias and result in patients' death.

1.6.4. Mechanical requirements

The encapsulation needs to protect the integrity of the sensor function, i.e., it should provide resistance of the sensor/implantable device to temperature variations, vibration, shock, etc. It also needs a "biocompatible shape" in order to avoid unnecessary wounds and make it more comfortable for the patient (sharp corners to be avoided).

1.6.5. Electrical pathway

The external packaging of the device can be part of an electrical circuit and programed to act as an electrode that completes a circuit, for example, defibrillator leads connected to a pacemaker. These devices have to take into account bio-impedances when delivering a high electric signal across the body.

1.6.6. Internal packaging

Implantable devices have the potential to integrate several microelectronic functions such as: wireless telemetry, data storage, on-board microprocessors for signal processing and therapy optimization, etc. These new functions lead to assembling crucial sensing and pacing functions with additional high voltage therapy modules which makes it impossible to manage on a single integrated circuit technology and maintain a sufficient noise immunity sensing. For this reason, packaging plays an important role on the signal transmission and avoiding EMI.

1.6.7. Reliability

The reliability of an implant, after insertion, depends on the probability of failure, f, which depends on fracture, wear, infection etc. Equation (12) shows the reliability factor, r, and can be expressed in terms of reliabilities, r_n, according to equation (13), where each reliability corresponds to a specific factor for failure [67]:

$$r = 1 - f \tag{12}$$

$$r_n = r_1 + r_2 + \ldots + r_n \tag{13}$$

The main cause of sensor failure inside the human body is corrosion of the sensitive electronics due to moisture diffusion into the sensor however, techniques exist in order to increase the reliability of an implantable sensor such as: moisture absorbers and humidity sensors. However, every implantable sensor needs a careful reliability evaluation which means that the sensor has to pass a series of accelerated life tests such as: baking, temperature cycling, burn-in, mechanical shock and steady-state life test [75].

Metal alloy implants such as, titanium alloys, stainless steels and cobalt-based alloys are employed universally since they are durable and provide good biocompatibility. However, polymer properties such as: flexibility, water impermeability (impermeable to gas with surface treatment), cost, EMC (electromagnetic compatibility), chemical and thermal resistance, etc., provide an excellent option of biocompatible materials such as ceramics, polyolefins, perfluorinated polymers (silicone rubbers) and polyurethanes.

2. Osmotic pressure sensors

Osmotic pressure sensors (OPSs) work similarly to the cells in the human body, making use of osmosis for the detection of an OF originating in the retention of solutes/ions while permitting water to diffuse. This can translate in a particular malfunction in the human organism.

An osmotic pressure sensor (OPS) is built around a reference chamber (RC, enclosed volume with a reference solution) which is in direct contact with a pressure transducer that monitors the pressure inside the RC, and which is separated from the external media through a semi-permeable membrane. The semi-permeable membrane is designed to block a specific solute from diffusing through the membrane. The retentate will trigger an osmostic flow of the permeate (water) towards the side of the membrane that contains a higher concentration of solutes in order to try to balance the OS of the solution according to figure 7. This process is known as *osmosis*. The sensor detection mechanism is based on a reduction, or increase, in hydrostatic pressure inside the RC created by the water escaping (due to a lower solute concentration than in the media), or entering (due to a higher solute concentration than in the media), the RC respectively. The pressure changes inside the reference chamber (RC) translate into the osmotic pressure (OP) set by the semi-permeable membrane, similar to the OP exercised on a cell membrane (CM) that selects the ions that can go through it. The OP would only stop increasing, or decreasing, when the OS inside the RC is equivalent to the one outside.

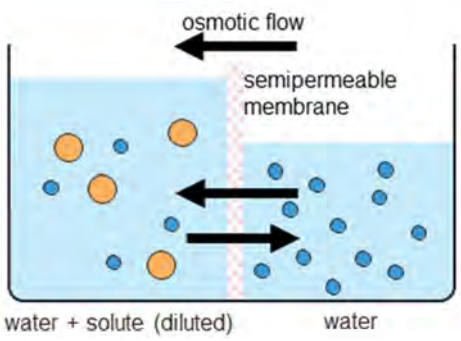

Figure 7: Water molecules, in dark blue, diffuse freely through a semi-permeable membrane while the solute of interest marked in yellow color is blocked by the membrane.

From figure 7 one can see an OF of water from the right side which continues until the increased hydrostatic pressure on the left side raises the escaping tendency of the diluted water to that of the pure water at atmospheric pressure, point when the osmotic equilibrium (OE) is achieved [76].

2.1. Osmotic pressure

The OF stops when the hydrostatic pressure inside the RC increases. By definition, the pressure required to achieve an OE (represented by the increase in hydrostatic pressure inside the RC) is known as OP, i.e., the water volume, represented by an hydrostatic pressure increase, required for a solution to achieve OE [76].

The OP Π is given by the van't Hoff equation according to (14):

$$\Pi = i \sum c_i RT \tag{14}$$

where *i* represents the van't Hoff factor given by the number of ions that dissociate in the solvent, c_i (mol L^{-1}), is the concentration of solutes/ions in a solution, *R* is the universal gas constant (0.08314 L bar mol^{-1} K^{-1}) and *T* is the thermodynamic (absolute) temperature (K) [5].

Van't Hoff's law (14) considers an ideal ion behavior in the solution (enthalpy of solution is zero) but is often used to estimate the OPs of solutions that are too concentrated (uneven ionic distribution) for the Law to apply exactly. One way of correcting this is by means of correction factors called osmotic coefficients [77]. Consider the osmotic coefficient (Φ), then Van't Hoff's Law becomes (15):

$$\Pi^{*} = \Phi\Pi \tag{15}$$

where Π^{*} is the compensated OP. Equation (15) compensated (14) for the deviation of the solvent from an ideal behavior. The osmotic coefficient can be calculated from the Pitzer equations [78].

2.1.1. Physiological aspects of osmosis

As it has been previously written in sections (1.2 & 2), OF plays an essential part in maintaining the physiology of the human body and other animals. For example, if a cell is placed in contact with deionized water (DI) water the ICF volume will increase dramatically, due to water diffusing inside the cell in order to reach an OE, and the cell will under these circumstances eventually rupture. The reason for a rupture is that the cell contains salts, and other solutes that triggers a solute concentration difference across the CM to the DI water outside. Another example of the importance of osmosis are fresh water fish that, like seawater fish, intake water through the gill tissue, through osmosis. Since the blood of fresh water fish contains about 1% salt content, whereas sea water contains about 3%, then these fish would dehydrate at sea [76]. Freshwater fish kidney function is adapted to constantly expel water. On the other hand, seawater fish kidney function is adapted to constantly retain water making them overhydrated in freshwater. The use of salt to preserve meat is also based on osmosis since any single cell organism, such as bacteria, would not be able to survive in that environment since water would be extracted from the organism through osmosis. An example could be the

presence of excess of solutes in the bowels (due to a person's diet or bowel irritation) draws water from the intestinal walls, giving rise to diarrhea.

2.1.2. Osmotic strength

The OS is regarded as the number of osmotically active solutes/ions in the interstitial fluids or human blood. Therefore, one can characterize OS as osmolarity, or osmolality, which correspond to the following: The normal blood osmolarity level for a healthy subject ranges from 280 to 300 mOsm L^{-1} [5]. The salts that govern the osmolarity are the most abundant in the human body, such as Na^+, K^+ and Cl^-, that appear due to the dissociation of chiefly sodium-chloride (NaCl), and potassium-chloride (KCl), in water. Considering NaCl and KCl the most abundant salts, one can use a phosphate buffered saline (PBS) solution to simulate the interstitial fluids in the human body. On can approximately calculate the OS/osmolarity of a PBS solution according to equation (16) :

$$Osmolarity = 2\left(\left[NaCl\right]+\left[KCl\right]\right) \tag{16}$$

where *[NaCL]*, and *[KCl]* represents the concentrations of the respective solutes in molar (M). The total osmolarity is increased by a factor of two because the salts are being dissolved in an aqueous solution and dissociating into 2 ions that are osmotically active: Na^+, K^+ and 2 Cl^- ions. The 2 factor represents the van't Hoff coefficient also used in (14) .

Water plays a very important role in the ionic hydration. According to Coulomb's law, the force between two charged particles is given by the following equation:

$$F = \frac{q_1 q_2}{D_e d^2} \tag{17}$$

Where q_1, and q_2, represent the charges (C), d the distance between the particles (m) and D_e the dielectric constant which is given by the media (solvent). Since water has a high dielectric constant, it requires less energy to break up the oppositely-charged particles in an ionic solid. It also reduces the attraction between the dissolved ions, discouraging their recombination. Water molecules attach to ions by ion-dipole interaction, further stabilizing the dissolved ions. Because they are now quite large, oppositely-charged hydrated ions cannot get very close to each other, and the tendency for them to recombine is reduced. This way, all ions dissolved in water are hydrated gaining a new hydration radius (hydration shell) dependent on the ionic charge.

3. Sensor interface

The electronic front-end interface is what makes the sensor possible to read by the end-user. In other words, the interface measures the physical parameter (e.g., osmotic pressure) from the analog world (physical world), does signal processing (digital) before it can transmit the signal back to the physical world.

A sensor will generate an electric signal in the form of current, voltage, resistance, inductance or capacitance variation. If one considers a biological/bioMEMS microsensor, then the desired signals are normally small in amplitude, dangerously close to white noise (background noise), or they can suffer from interference from undesirable signals located in different frequency bands. Low power interface circuits, such as the one presented in this project, are designed to run/supply a sensor, record raw data, perform signal conditioning and transmit the signal to an external receiver. Therefore, one can assume the existence of an analog shell separating the sensor world from the user requiring some signal processing [79].

Integrated circuits (ICs) are built using CMOS technology. This technology was invented by Frank Wanlass, and patented in 1967 [80], and it is used in microprocessors, microcontrollers, etc. This technology permits allocating a high density of logic function on a chip by using a combination of p-type and n-type Metal-oxide-semiconductor field effect transistors (MOSFETs) to implement logic gates and other digital circuits.

A key element in realizing miniaturized remote operated sensor nodes is the design constraints governing their physical size and the compromise of device complexity and the consumption of power. Microsystems integrating both the sensor and the electronic platform for the interface benefit largely from the progress made in the Very-Large-Scale Integration (VLSI), where the advances made in microsystems technology and mixed signal circuit design (MSCD) have been equally contributing for this progress in order to permit the design of complex electronic circuitry on a minimum footprint.

The circuit interface here presented is a good example of a VLSI integrating a pressure transducer together with a MSCD interface responsible for translating the transducer's output to a signal that the user can read. This is a *proof of concept* however, the system has to be characterized and validated for use in the human body where the following challenges must be addressed:

- *Low-power* – This will help powering the device which could be *via* a battery or induced. Nevertheless, it is important to keep the power level as low as possible in order to avoid dangerous current levels and heat generation from the device. This is here implemented by using low voltages (regulated voltage supply of 1 V) and avoiding the use of an Analog to Digital converter (ADC) which would require a clock generator that is very power consuming. Also, the sensor does not need to sample constantly and can be powered only for short periods.

- *Sensitivity* – By using a low voltage (1 V) to operate the pressure transducer, instead of the recommended 5 V supply on the datasheet (appendix 5), one is reducing the sensitivity significantly. Sensitivity is here compensated by "constantly" inverting the supply voltage to the pressure transducer and is explained in section 4.1.2.

- *Low noise* – This plays a very important role in biological signals where their amplitudes, and frequencies, can be small which leads to a bigger influence from noise (white noise) that can damp the sensor output and make it impossible to read/detect changes in OP. The most significant sources of noise are thermal, and flicker. Low noise is here addressed by reducing the circuit's dependency on the unregulated supply and making sure that the transconductance amplifier (OTA) has a good Common mode rejection ratio (CMRR), and power supply rejection ratio (PSRR), in order to achieve a good signal-to-noise ratio (SNR), as high as possible.

- *Small footprint* – A small footprint is a paramount aspect of BioMEMS since it reduces the sensors' size making the implantation easier and avoiding/delaying inflammation. For this project we use transistors that are 90 nm wide by using the TSMC (Taiwan Semiconductor Manufacturing Company) 90nm technology where smaller transistors translate into a higher speed. We also make use of the advances made in microfabrication technology in order to bond the ASIC to the same substrate as the pressure transducer and integrate the substrate with the sensor's encapsulation. In addition to this, smaller transistors require less power facilitating a reduction in the overall power supply towards 1 V while individual elements operate at a minimum threshold voltage of 0.3-0.4 V [81].

CMOS transistors operating in the sub-threshold regime (section 3.1) offer a current figure of merit of 2.2 fJ per data conversion [82] and novel architectures are deemed to push this number beyond the pJ level [83]. The combination of small size, complexity and ultra-low power consumption will enable medical sensor nodes orientated towards a "*cloud-based*" technology for "*mobile health systems*" (mHealth) [84].

Throughout this section, it will be given a general overview about the transistors' properties/functionalities and purpose. This material constitutes a revision of what is available on text books but has been considered relevant since this was a big part of the project, i.e., had to be taken into consideration when designing, and simulating, the circuit's schematics and layout

3.1. Mixed Signal Circuit Design

In order to connect the outside (analog), to the digital (electronic) world for signal storage and processing, it is important to make use of both analog and digital circuitry design with MSCD. Since natural occurring signals are analog (e.g. sound, photocells in video camera, etc.), one need to build analog circuits that detect natural signals which is then processed digitally. The purpose of digital electronics is to handle more signals simultaneously which results in faster data handling and which is less prone to noise. During the 70s, Gordon Moore predicted that the number of transistors (digital units) per standardized chip size would continue to increase to the double at every one and a half years and this law is still valid today showing that the transistors size has been dropping considerably, increasing the circuit's speed respectively. However, the design of ADCs for high speed, high precision and low power dissipation constitutes many of todays' challenges putting at risk Moore's law [85]. One of today's challenge for medical sensor technology, such as the one use in this project, is to detect signals that have very low amplitudes (voltage, current or resistance changes) that are difficult to differentiate from white noise (background noise). For this reason, it is important to consider the PSRR, and CMRR, of CMOS amplifiers that will affect the circuit's SNR.

Transistors are built on a silicon substrate however, silicon itself is a poor conductor, since it has no free carriers, except when doped with extra electrons (n-type), or holes (p-type). While the n-type transistors are classified as nMOS, the p-type are classified as pMOS defining two types of transistors (figure 8):

- nMOS: Negatively doped silicon, rich in electrons.

- pMOS: Positively doped silicon, rich in holes.

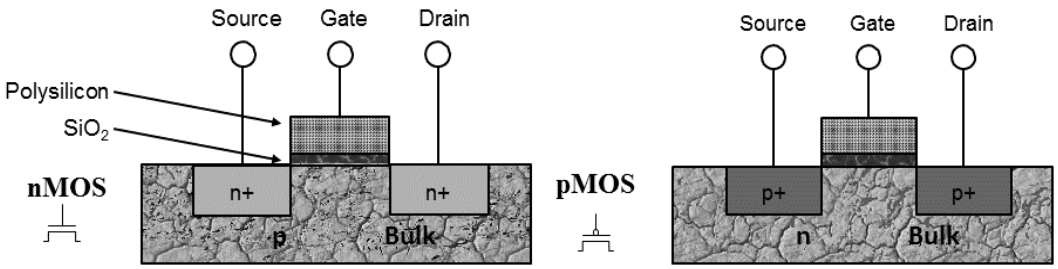

Figure 8: nMOS (left image with schematics representation) and pMOS (right image with schematics representation) type transistors. Transistors have four terminals: Source, Gate, Drain and Bulk (substrate) which is made of Silicon. Modified image from [85].

Both transistor types must be fabricated on the same wafer, i.e., the same substrate, meaning that the pMOS device is placed in a well (n-well). nMOS, and pMOS, are called NFET, and PFET, respectively.

Ideally MOSFETs work as switches where 1 represents a high state, equivalent to a higher voltage (e.g. 1 V), and 0 represents a low state, ground (GND). However, a MOSFET is far from ideal after fabrication and leakage currents occur from the technology limitations that create contact areas where there should be none. There are extrinsic and intrinsic capacitances associated to each MOSFET and that affect the transistor/circuit performance. Intrinsic capacitance is associated to gate-to-Bulk capacitance (built by the gate-oxide and oxide substrate capacitances connected in series), while the extrinsic capacitances can be classified as: overlap, and junction, dependent on the geometry and bias, respectively that can be improved with optimized layouts.

In order to better understand the transistors properties, one has to study it's I/V curve. The main concept is the threshold voltage: since there is a capacitance between the gate and the bulk, if a voltage is applied to the gate (Vg) and increased, then the holes in the substrate are repelled from the gate area leaving negative ions behind, proportional to Vg. This way, a depletion region is formed but it does not conduct current since there are no charge carriers available. As Vg increases so does the depletion region until electrons start to flow from the source into the interface and into the drain creating a

"channel" of charge carriers between the source and drain which corresponds to "turning on" the transistor (figure 9). The voltage necessary for the transistor to turn on is the threshold voltage (Vth) [85].

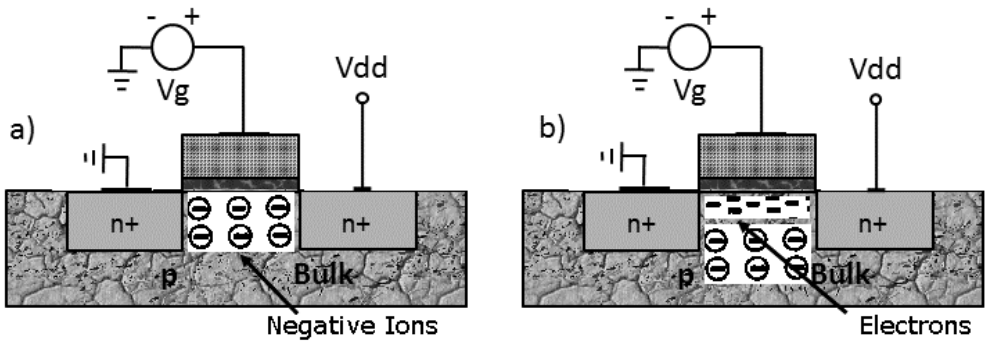

Figure 9: MOSFET driven by gate voltage where, a) is the formation of the depletion region until b) it becomes wide enough and charge carriers start flowing, turning on the transistor (Inversion layer). Modified image from [85].

The I/V characteristics of a MOSFET can be derived from equation (18):

$$I = Q_d v \tag{18}$$

One considers a semiconductor with a bar geometry (similar to the inversion layer) carrying a current, *I*. Afterwards the charge density, Q_d (C/m), that crosses the bar with velocity, *v* (m/s), is calculated. Since *v* = μE and E(x) = -(dV/dx), we end up with a current given by (19):

$$I_D = WC_{ox}\left[V_{GS} - V(x) - V_{th}\right]\mu_n \frac{dV(x)}{dx} \tag{19}$$

where *W* represents the width of the transistor, C_{ox} the gate oxide capacitance, V_{GS} is the gate-source voltage, *V(x)* is the channel potential at x and V_{th} is the threshold

voltage. Inserting the boundary conditions V(0) = 0 and V(L) = V_{DS}, where *L* is the effective channel length of the transistor and V_{DS} the drain-source voltage, and performing an integration according to (20):

$$\int_{x=0}^{L} I_D dx = \int_{V=0}^{V_{DS}} WC_{ox}\mu_n \left[V_{GS} - V(x) - V_{th}\right] dV \tag{20}$$

where μ_n is the electrons' mobility, we obtain:

$$I_D = \mu_n C_{ox} \frac{W}{L}\left[\left(V_{GS} - V_{th}\right)V_{DS} - \frac{1}{2}V_{DS}^2\right] \tag{21}$$

where I_D is the drain current. The typical I/VDS curve can be seen in figure 10 where there is an exponential phase given by a subthreshold conduction, a linear phase known as the triode region and finally a quadratic phase known as the saturation region (maximum current).

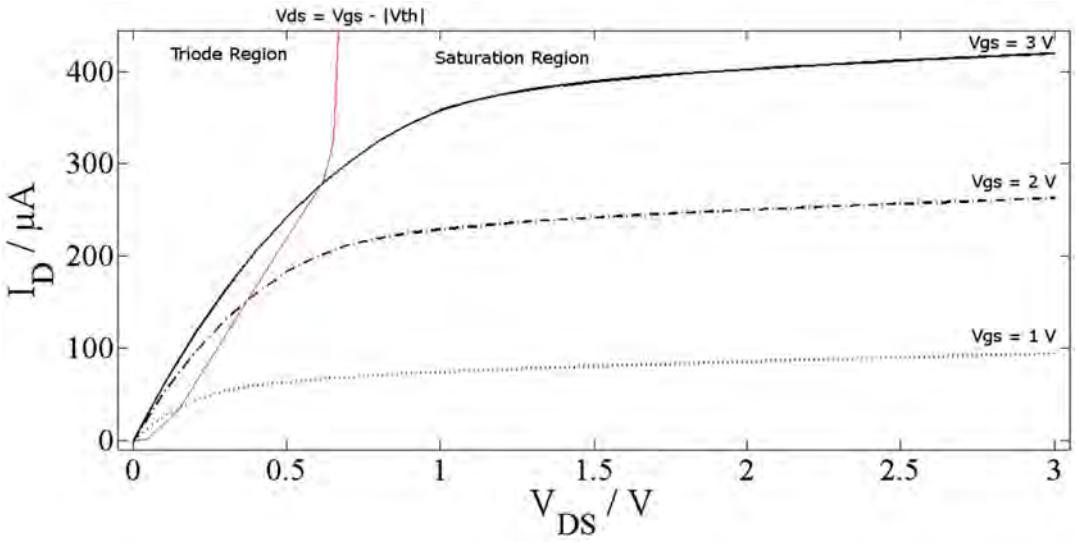

Figure 10: Simulation of the I_D/V_{DS} saturation curve for an n MOSFET using cadence virtuoso. The red line separates two regions of operation of modern MOSFETs: the triode (also known as Ohmic), and saturation, regions. However, there is another region of interest: the subthreshold region where V_{DS} is approx. zero ($V_{GS} \approx V_{th}$). A Low voltage threshold (lvt) transistor model was used from the TSMC 90 nm technology library (W = 100 nm, L = 200 nm and Vth = 426.3 mV).

The transconductance quantifies the drain-current variation with a gate-source voltage variation while keeping the drain-source voltage constant:

$$gm = \left.\frac{\partial I_D}{\partial V_{GS}}\right|_{V_{DS}} \tag{22}$$

One would normally aim for a high gm however, there is a tradeoff between signal amplification and noise amplification. Moreover, a higher gm will imply wider transistors that will consume more layout space.

3.1.1. Second order effects

If both the source and bulk of the transistors are not tied to ground, or that L is not constant and that the transistor does not work as a perfect switch, then there are 3 second order effects that needs to be considered as essential for circuit design [85]:

- **Body effect or backgate effect**: When the bulk voltage, V_B, drops below the source voltage. Considering $V_G < V_{th}$, as V_B becomes more negative, more holes are attracted to the substrate leaving a wider depletion region however, since V_{th} is a function of the charge density (Q_d) before the inversion layer is formed, then V_{th} also increases with an increase in Q_d that occurs due to a wider depletion region.

- **Channel-length modulation**: L decreases as the potential between the gate and drain, V_{GD}, increases ($L = L - \Delta L$).

- **Subthreshold conduction**: When the gate source potential, V_{GS}, is approximately the same as V_{th} ($V_{GS} \approx V_{th}$) there is a so called "weak inversion" layer that still lets some current flow from the drain to the source.

3.1.2. Sub-threshold region

In contrast with bipolar transistors, for V_{DS} lower than the threshold voltage ($V_{GS} \approx |V_{th}|$), MOS devices still conduct some current with an exponential behavior given by:

$$I_D = I_0 e^{\frac{V_{GS}}{\zeta V_T}} \tag{23}$$

Where $\zeta < 1$ (non-ideality factor) and $V_T = KT/q$. It is difficult to visualize this behavior in figure 10 but, if a logarithmic scale is used instead, this region can be observed. This operation mode is essential in modern circuit design, as well as our design, in order to save power, low power operation.

3.1.3. Triode region

The triode region, also known as the linear region (figure 10), is given by: $V_{DS} < V_{GS} - |V_{th}|$ where:

$$I_D = \frac{1}{2}\mu_n C_{ox}\frac{W}{L}\left(V_{GS} - V_{th}\right)V_{DS} \tag{24}$$

In this case, the linear relationship for the drain-source path can be represented by a linear resistor given by:

$$R_{on} = \frac{1}{\mu_n C_{ox}\frac{W}{L}\left(V_{GS} - V_{th}\right)} \tag{25}$$

A MOSFET can then operate as a resistor as long as the overdrive voltage (V_{GS}-V_{th}) is much higher than V_{DS}, $V_{DS} << 2(V_{GS} - V_{th})$ which corresponds to the deep triode region. From (22) one can calculate gm to be:

$$gm = \mu_n C_{ox}\frac{W}{L}V_{DS} \tag{26}$$

3.1.4. Saturation region

This region corresponds to the quadratic curve shown in figure 10. If $V_{DS} > V_{GS} - |V_{th}|$ then:

$$I_D = \frac{1}{2}\mu_n C_{ox}\frac{W}{L}\left(V_{GS} - V_{th}\right)^2 \quad (27)$$

This corresponds to $\partial I_D/\partial V_{DS}$ in the triode region which gives us the maximum I_D. From (22), gm can be given by:

$$gm = \mu_n C_{ox}\frac{W}{L}\left(V_{GS} - V_{th}\right) \quad (28)$$

The saturation region corresponds to the state when the transistor is “ON”.

3.1.5. Single stage amplifiers

Amplification is essential for circuit design. One must amplify an analog, or digital, signal because the signal is too low to drive a load, for overcoming the noise of a subsequent stage or for providing digital levels to a digital circuit. There are four type of configurations that will be here revised: common-source (CS) and common-gate (CG) topologies, source followers (SF) and cascode (CO) configuration [85].

3.1.5.1. Common source

This configuration, translates the gate-source voltage variations into an output current due to its transconductance properties. This current, when integrated in Rd, translates to a voltage output (Vout) according to figure 11.

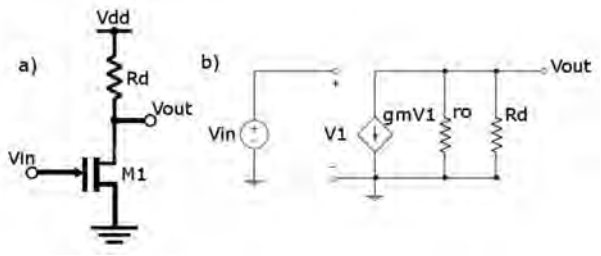

Figure 11: a) Common Source stage and b) Small signal representation considering M1 output resistance (ro).

Making the small signal analysis on can derive the following equations:

$$gmV_1(r_0 \,||R_D) = -V_{out} \tag{29}$$

Where $V_1 = V_{in}$ and the voltage gain $A_v = V_{out}/V_{in}$ then:

$$A_v = -gm\left(r_0 \,||\, R_D\right) \tag{30}$$

3.1.5.2. Source follower (common drain)

From the CS analysis one can see that the higher is R_D, the higher is the voltage gain (considering limited input supply). If the objective is to drive a low impedance load, then a buffer such as a source follower must be implemented after the CS (figure 12). This way, there will be negligible loss of signal. The SF can operate as a voltage buffer meaning that the output voltage will follow the input voltage, avoiding changes in Vout.

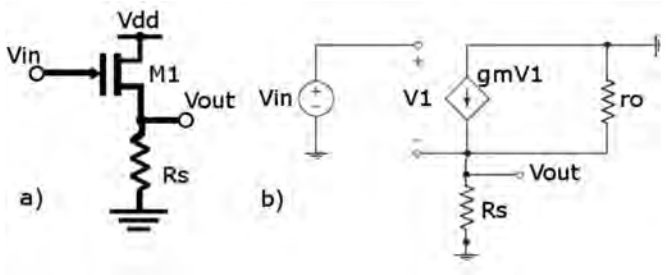

Figure 12: a) Source follower (SF) and b) Small signal representation considering M1 output resistance (ro).

From the small signal analysis one derives the following equations:

$$A_v = \frac{V_{out}}{V_{in}} = \frac{r_0 \parallel R_D}{\frac{1}{gm} + (r_0 \parallel R_D)} \approx 1 \tag{31}$$

Where $R_{out} \approx 1/gm \,||\, R_S \approx 1/gm$.

3.1.5.3. Common gate

Opposite to common source and source follower configuration, it is also possible to connect the source to the input signal, producing the output at the drain terminal according to figure 13. It can use higher Rd values producing higher voltages than the CS stage at the output. The gate is biased with a dc voltage to establish proper operation conditions.

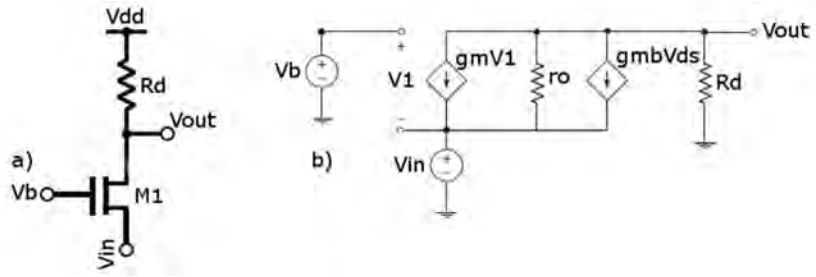

Figure 13: a) Common gate (CG) and b) Small signal representation considering body effect.

After a small signal analysis:

$$A_v = \left(\left(gm + gmb \right) r_0 + 1 \right) \frac{R_D}{r_0 + R_S} \tag{32}$$

Where Rout = $r_0 || R_D$, which will give us an $A_v \approx gmr_o$.

3.1.5.4. Cascode configuration

From figure 14 it is easy to see that the cascade of a common source with a common gate is called a "cascode" [85]. As it has been previously mentioned, the input signal of a common gate configuration can be a current and a common source converts a voltage signal to a current signal.

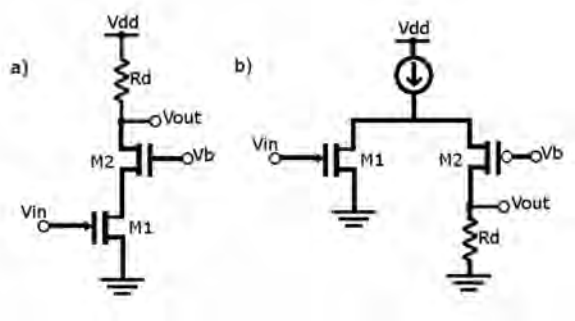

Figure 14: a) Cascode stage b) folded cascade with NMOS input.

M1 generates a small signal current proportional to Vin while M2 routes the current to R_D and converts it to a voltage (Vout). An important property of the cascade configuration is the output resistance, Rout, given by:

$$R_{out} = \left[1 + \left(gm2 + gmb2\right) r_{02}\right] r_{01} + r_{02} \tag{33}$$

By increasing the output resistance, R_{out}, one is increasing the voltage gain. Assuming $gmr_0 >> 1$ then:

$$R_{out} \approx \left(gm2 + gmb2\right) r_{02} r_{01} \tag{34}$$

Since $Gm_{total} = gm1$:

$$A_v = \left(gm2 + gmb2\right) r_{02} gm1 r_{01} \tag{35}$$

From figure 14 a), the cascode stage configuration main idea is to convert the input voltage into a current and apply the result to a common gate stage. However, nothing dictates that the transistors have to be of the same type. In fact, one can use an NMOS, and PMOS, in a cascode stage. The folded cascode configuration achieves an output impedance comparable to that of a normal telescopic amplifier (lower gain tradeoff) with lesser number of devices stacked between supply and ground in the output stage. This way the folded cascode is able to provide more output swing.

3.1.6. CS stage with current source load

Increasing the load resistance will increase the transistors gain (Av = -gmRd) but with the tradeoff of less voltage swing. Another approach could be to use a current source like in figure 15.

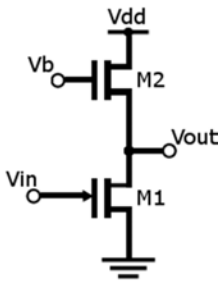

Figure 15: CS stage with current source load.

When both transistors operate in saturation then:

$$A_v = -gm_1(r_{01} \| r_{02}) \tag{36}$$

3.1.7. CS stage connected with a diode load

In CMOS fabrication layout space is important both for economical, and power consumption, reasons. In this way, resistors are often replaced by MOS transistors that can operate as a small signal transistor if the gate, and drain, are shorted together according to figure 16 (diode load connection).

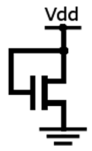

Figure 16: Diode connected NMOS.

The transistor will always be in saturation because the gate and drain have the same potential.

3.1.8. Differential amplifier

One of the most common tricks used both by biological and engineered devices for computing measurements insensitive to absolute reference values and robust to noise, is the one of using difference signals [86]. Instead of a single ended signal (measured in reference to ground, 0 V) a differential signal between two nodes can be measured in regards to a common mode potential (CM) that can have equal, or opposite signals to it, resulting in higher input voltage swings. This configuration plays an important advantage in improved PSRR and in higher output voltage swings. An example of a basic differential amplifier using diode loads can be seen in figure 17.

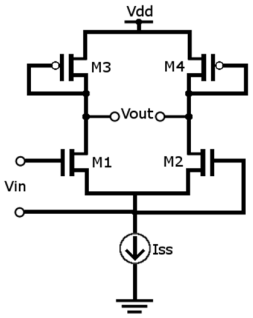

Figure 17: Differential pair diode connected

Implementing the half-circuit concept for small signal analysis where both transistor's branches are grounded, then the circuit gain is equal to the gain of one branch of the differential amplifier according to (36).

3.1.9. Current Mirror

An important issue that can affect a circuit's SNR is the use of stable current sources. From (21) one can see that I_D/I_{out}, has dependencies on the supply (V_{dd}), process and temperature. The overdrive voltage depends on the supply, and threshold, voltages and threshold voltage can vary by 100 mV from wafer to wafer. For this reason, the design of current sources in analog circuit is based on copying a reference current source that can be independent of temperature, process and supply voltage (reference generator) according to figure 18.

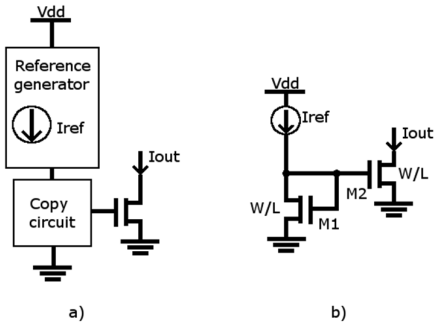

Figure 18: a) Current copying representation (conceptual) and b) basic current mirror

Two identical MOS devices, with the same gate-source voltage (Vgs) and operating in saturation, carry equal currents if one neglects channel length modulation. This way, from figure 18 b) one can write the following equations:

$$I_D = \frac{1}{2}\mu_n C_{ox}\left(\frac{W}{L}\right)_1 \left(V_{GS} - V_{th}\right)^2 \tag{37}$$

From M2:

$$I_D = \frac{1}{2}\mu_n C_{ox}\left(\frac{W}{L}\right)_2 \left(V_{GS} - V_{th}\right)^2 \tag{38}$$

Where the following relation between the transistors' size can be obtained:

$$I_{out} = \frac{\left(W/L\right)_2}{\left(W/L\right)_1} I_{ref} \tag{39}$$

Therefore, the ratio of *Iout/Iref* is given by the ratio of the devices dimension.

3.1.10. PSRR, CMRR & SNR

Thermal, and flicker, noise generated by the thermal agitation of the charge carriers and/or impurities in a conductive channel, respectively will affect the performance of any circuit especially in cases where the signal that needs to be detected is almost of the same order of magnitude as the noise. This is especially relevant for biological applications such as, for example, the study of neuronal action potential propagation [87], depending on the ionic concentration of chiefly salts such as Potassium (K^+) and Sodium (Na^+). For this reason, subthreshold operation of MOS transistors is extremely important in order to simulate biological functions. However, more importantly, a good CMRR and PSRR, are extremely important in order to detect signals of this order of magnitude.

When detecting low level signals, such as biological signals, the use of high performance amplifiers is necessary. In analog circuit design, the main building blocks are OTAs. Therefore, the performance of these amplifiers should be studied and analyzed as

function of power supply variations. The PSRR is often specified at dc or at very low frequencies (f < 1 Hz) [86]. This can be defined as:

$$PSRR = \frac{A(s)}{A_p(s)} \tag{40}$$

where $A_p(s)$ is the power supply gain and $A(s)$ is the open loop gain. PSRR is defined in the frequency domain where s = j.ω. By increasing the Gain Bandwith (GBW) of an amplifier, A(s) will also increase since it is directly proportional to the GBW [A(s) = 2.π.GBW/s for f > $f_{dominant}$], and as a result the PSRR increases. Therefore, ideally the PSRR should be infinite.

In order to compare different amplifiers, the PSRR can be normalized to 2.π.GBW/s, resulting in the parameter l/A_p(s) , i.e., the PSR [88]. The smaller is the power supply gain, the higher is PSR resulting in a better circuit performance (less noise contribution). In addition, if an amplifier has different power supplies, i.e., a negative (Vss) and a positive (Vdd), then both will have a PSRR value ($PSRR_{Vdd}$ and $PSRR_{Vss}$). The power supply variations introduce a current which can be translated in a transconductance (Gm_p). This current is then converted into a voltage at that same gain node as for the signal transfer function. As a result, the denominator of the voltage transfer functions, A_p(s) and A(s), are equal to each other and hence the PSRR can be given by the ratio of the signal transconductance (Gm) and the power supply transconductance (Gm_p):

$$PSRR = \frac{Gm}{Gm_p} \tag{41}$$

Another important factor for avoiding signal degradation from noise is the CMRR. Different from PSRR, the noise contribution gives variations at the common mode input

(V_{CM}) from the differential amplifier. These signals can appear at V_{CM} with the same, or opposite, phase which can be amplified considerably. For example, if there are both $PSRR_{vdd}$, and $PSRR_{vss}$, contributions of the same magnitude, then the noise contribution will double in value at the CM input node of an amplifier. The CMRR can be defined according to the following equation:

$$CMRR = \frac{A_v}{A_{CM}} \tag{42}$$

where *Av* is the single node gain and A_{CM} is the CM gain. Both PSRR, and CMRR, can be measured in decibels and the bigger these values are, the more immune to noise is the op-amp, translating in a better SNR which corresponds to the ratio between the signal and the total background noise that originates from the noise sources already described previously in this section. In this way:

$$SNR = \frac{P_{signal}}{P_{noise}} \tag{43}$$

where P_{signal}, and P_{noise}, are the total signal, and background noise, power respectively.

A way of reducing the total noise power is by implementing an independent current source, i.e., by designing a current source independent of temperature variations one can achieve a stable voltage supply that is not affected by temperature variations also known as the bandgap reference (section 4.2.1). This supply voltage will also be independent of an unregulated initial supply that could arise from, for example, a wireless power source.

4. Sensor Design Implementation

The design implications of the OHS such as low power interface architecture, separation using a membrane and pressure transducer size make this sensor suitable for biomedical/biological applications. Therefore, this sensor could benefit from the technology developments made around fuel cells such as glucose fuel cells, as a reliable and long-lasting energy source. Glucose fuel cells, based on abiotic catalysts such as noble metals and activated carbon, have already been developed as power supplies for cardiac pacemakers in the sixties however, even though it has been demonstrated its long lasting capabilities, its power performance is limited to μW [89]. For this reason, it became extremely important to focus on the developments made in the MEMS industry and apply them to the OHS in order to enhance its properties and make it a suitable solution for future implantation. These properties are: sensor size, membrane size, pressure transducer size, CMOS processing technology, power consumption/supply voltage, power supply, choice of materials, longevity, sensitivity, etc.

In this section the different development stages of the final sensor prototype (project aim) are demonstrated. However, the final prototype is a result of an evolution of previous prototypes developed to help finding the right materials/parts. In this way, three different prototypes were used in this project in order to validate the different parts constituting the OHS such as:

- *Prototype 1* – A similar osmotic sensor had been used in a previous project [22] (stainless steel encapsulation) and has been adapted to an acetal copolymer encapsulation in order to study the permselectivity of different types of membranes. This work has been published in [5].

- *Prototype 2* – This prototype was composed by a custom made test PCB connected to the pressure transducer used in this project (SW415-2, Sensonor AS, Norway) in order to test the produced ASIC and the purchased transducer. The pressure transducer was bonded the PCB and connected to

a pressure pump in order to simulate different pressures (pressure vs output frequency). This work was published in [90].

- *Prototype 3* – This constituted the final prototype that integrated the whole system together. This system was composed by an encapsulation containing the semi-permeable membrane, separating a RC from the external media, and a substrate integrating the pressure transducer and the ASIC. This was all assembled together with a measurable beaker that contained different solutions mimicking the interstitial fluids of the human body with different osmotic strengths, simulating different levels of hydration. This work was published in [91].

The OHS sensor here presented is a *proof of concept* at a larger scale however, its interface uses a low power architecture in order to keep a small footprint with minimum power consumption so that the sensor can have the possibility to be implantable and be power induced activated with, for example, the near field interface (NFC) of a smartphone. The lower the power consumption is, the more achievable it will be to power the sensor using fuel cell technology such as, for example, a glucose fuel cell for powering implantable medical devices [92]. Glucose fuel cells have already reported peak powers of 180 μW [93]. This would be particularly useful if one considers continuous measurements with a hydration threshold alarm.

4.1. Osmotic pressure sensor

The sensor here presented, uses a MEMS transducer (section 4.1.22) to record the OP generated from the water diffusion, through a semi-permeable membrane, due to OP changes that result from the ionic concentration difference between two medias/solutions separated by the same membrane (figure 19). The osmotic sensor showed in figure 19 is built around a RC integrated as part of a sensor housing, with a small access channel to a pressure transducer, and separated from the outside media

with a semi-permeable membrane fixed to the encapsulation using an O-ring together with a membrane support disc. The RC is filled with a reference solution (RS) containing the same OS as the BF in the human body and, any changes in the OS of the liquid media surrounding the sensor encapsulation will translate in a change in the OS as it has been previously explained.

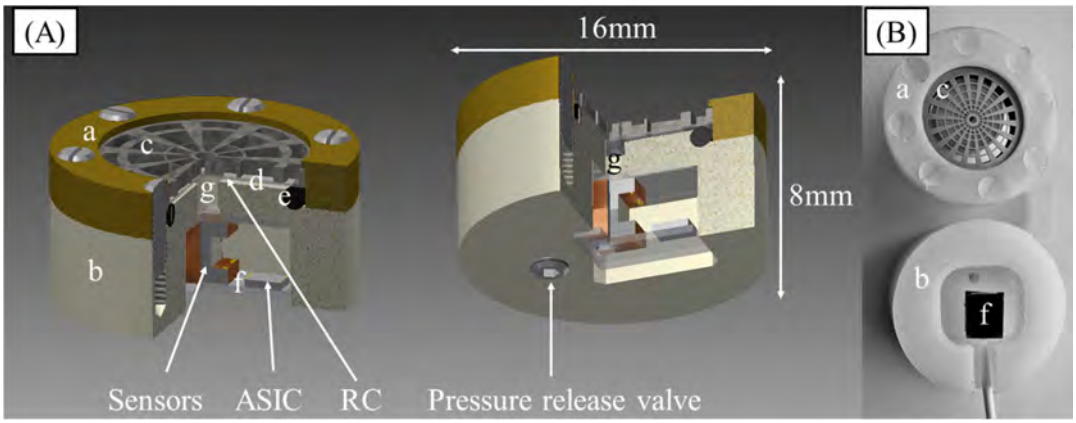

Figure 19: (A) CAD image of the hydration sensor including (a) the lid, (b) sensor housing, (c) stainless steel membrane support disc, (d) semi-permeable membrane, (e) O-ring, (f) substrate with two pressure transducers mounted back to back with the ASIC and (g) a small channel filled with paraffin oil. The lid and sensor housing is attached by 6 x M2 screws. (B) Sensor encapsulation made in acetal copolymer sharing the same lettering as in A [91].

4.1.1. Encapsulation

The sensor encapsulation was manufactured in acetal copolymer (RS components, 139-546, UK) and designed to be round shaped in order to avoid sharp edges that could lead to inflammation and an immune response associated to it but also because it was easier to fabricate (figure 19 B).

4.1.1.1. Membrane

The membrane used for the separation is one of the most important parts of the hydration sensor since it plays a very important role in the changes in OP (responsible for retaining the salts), the detection time, sensitivity and resolution of the sensor. Any

leaks will increase the noise of the system and will affect the resolution by impending it to reach the maximum OP.

From previous studies [5], the use of the commercially available Nafion N115, or NR211, (Ion Power, USA) was proved to be the best choice. The Dupont Nafion PFSA membrane commercially available from Ion Power, USA, is a non-reinforced film based on the chemically stabilized PTFE copolymer in the acid (H^+) form. These membranes exhibit excellent physical and chemical properties, proving to have an excellent mechanical and chemical stability. However, the Nafion reduces the OP by half, or more, since it will only block the Anions present in the PBS solution.

Nafion films are first synthesized by the copolymerization of tetrafluoroethylene (TFE) and a derivative of a perfluoro (alkyl vinyl ether) with sulfonyl acid fluoride. The resulting product is sulfonyl fluoride ($-SO_2F$) groups that can be extruded into a film. When this film is immersed in a hot aqueous NaOH the ($–SO_2F$) groups convert to sulfonate groups ($-SO_3^-Na^+$) giving us the neutral/salt form of the Nafion. Nafion can be converted to the acid form, containing the sulfonic acid ($-SO_3H$) groups. The Teflon backbone with the sulfonic acid groups is what gives the Nafion its characteristics.

The membrane implementation/choice was based on the patent from LeVeen et al. [20] where dense polymeric membranes are suggested in his invention. However, ePTFE ($QBV657^{EXP4D}$, GE, USA) is an example of a membrane with trademark GORE-TEX (microporous PTFE or expanded PTFE) and proved to be too dense as did SILON (Silon-IPN, BioMedSciences, USA) and PTFE (Teflon PFA, Chemours, USA).

4.1.2. Transducer

The osmotic sensor is equipped with the SW415-2 silicon pressure transducer (Sensonor, Norway). This is a microfabricated silicon membrane die equipped with four piezoresistors in a Wheatstone bridge configuration. The piezoresistors are embedded in an N-Epi layer that prevents direct contact with the aqueous media, making this

sensor resistant to hostile environments such as the interstitial fluid of the human body according to figure 20 [92]. The transducer has a bridge resistance of 12 kΩ and offers a sensitivity of 64 mV bar^{-1} rated at a standard supply voltage of 5 V. In contrast, the power conserving methodology employed in this work has limited the supply voltage to 1 V (Bangap reference output voltage) which in turn is inverted for every transition of V_{out}, increasing its sensitivity according to (44).

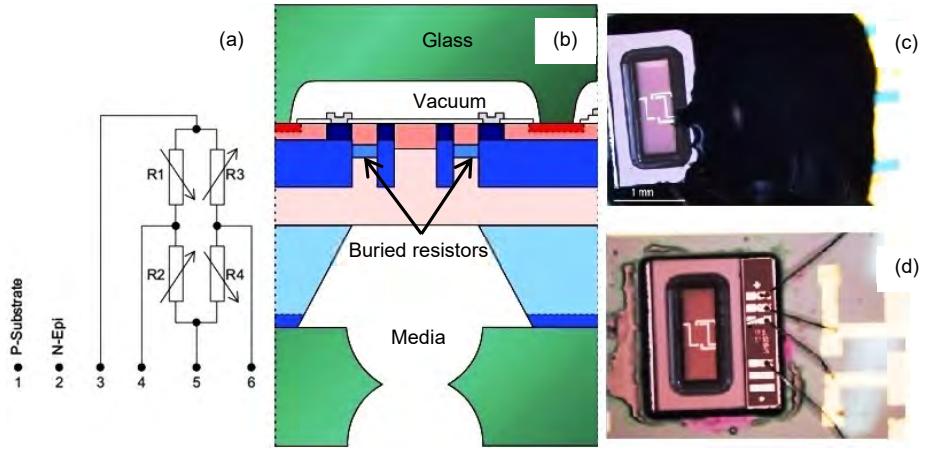

Figure 20: (a) Electrical circuit diagram for the SW415-2 pressure sensor, (b) SW4 pressure sensor series microfabrication diagram, (c) Glob top epoxy covering / insulating the gold wires and (d) Wire bonding between the pressure sensor and the cooper on the PCB for prototype 2. Figures (a), and (b), provided by Sensonor AS.

Although a 1 V supply will decrease the sensitivity to 12.8 mV bar^{-1}, the tradeoff lies in saving power while maintaining adequate device performance. In order to save power (number of resistive components used is proportional to the power dissipation) the pressure transducer's supply voltage is inverted, for every transition of V_{out}, permitting the use of one branch of the transducer without losing sensitivity by keeping the same pressure change times two (2Π). The maximum pressure that can be applied to the SW415-2 is 2 bar which translates in a total resistance variation given by (44):

$$\Delta R = (R_1 + R_2) \times sensitivity_{1\,V} \tag{44}$$

where, V_{supply} = 1V, (R_1 + R_2) = 12 kΩ and a sensitivity (for 1 V supply) = 12.8 mVbar^{-1}. The change in resistance thus corresponds to ΔR = 153.6 Ω bar^{-1}, but due to the constant inversion of the sensor's supply, ΔR = 307.2 Ω bar^{-1}. Thus, for ΔΠ = 2 bar, ΔR = 614 Ω.

The MEMS transducer is used to record the OP generated in the RC from the water diffusion through the semi-permeable membrane. The expected pressure change is 745 mbar (±372.5 mbar) which will correspond to a change in the output frequency of approx. 6.5 Hz, between 8.5 Hz (0 bar) and approx. 15 Hz (745 mbar) as it is explained in section 6.4. The pressure transducer is characterized for a pressure span of 2 bar (figure 35).

4.2. ASIC

The front end interface of the OHS was based on a previous design used for a blood glucose sensor [22]. This design was modified and translated from the STMicroelectronics deep sub-micron process (STM 90nm) [93] to the newer TSMC 90nm processing technology that is currently used by the collaborating partner on the IC circuit design (Nanoelectronics group (NANO) at the Department of Informatics (IFI), University of Oslo (UiO)).

The new interface could be described as an "upgrade"/improvement of a previous one developed by P. Häfliger and E. Johannessen [93]. The objective was to create a similar circuit in TSMC 90nm technology (uses 1 V supply) and add new circuit blocks such as, for example, the temperature block shown in figure 21 that helps compensating for temperature induced pressure changes. The SNR was improved by focusing mainly on three blocks: the bandgap reference, the bias generator and the pressure-to-frequency converter according to figure 21. Also, the circuit should be able to monitor temperature.

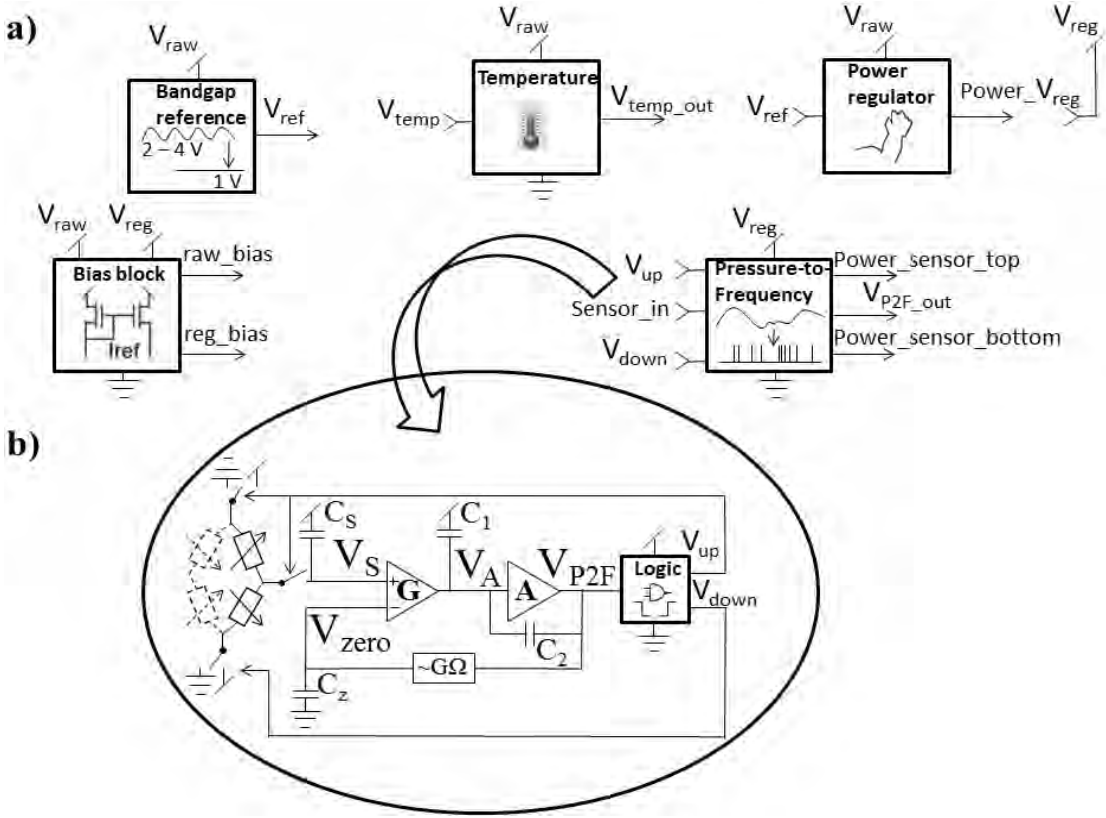

Figure 21: Block diagram of the front-end interface circuit design where a) represents the different blocks while b) is a more detailed overview of the pressure to frequency block converter (P2F).

As it has been previously stated, the circuit diagram presented in figure 21 represents a further development of the architecture developed in [93, 94] and is divided in five main blocks comprising (i) a bandgap reference, (ii) power gain (for the regulated voltage), (iii) bias circuitry, (iv) temperature and (v) pressure-to-frequency (samples, and powers, the pressure transducer and outputs V_{P2F_out}). However, since the ASIC does not hold a telemetry block, it will be externally powered, in contrast with [93].

4.2.1. Bandgap reference/Power amplifier

A bandgap reference, based on Browkaw circuit (figure 22 & figure 33) was chosen for use in the ASIC due to its stable output voltage which is proportional to the bandgap of the substrate (silicon) which is approx. 1.25 V [95].

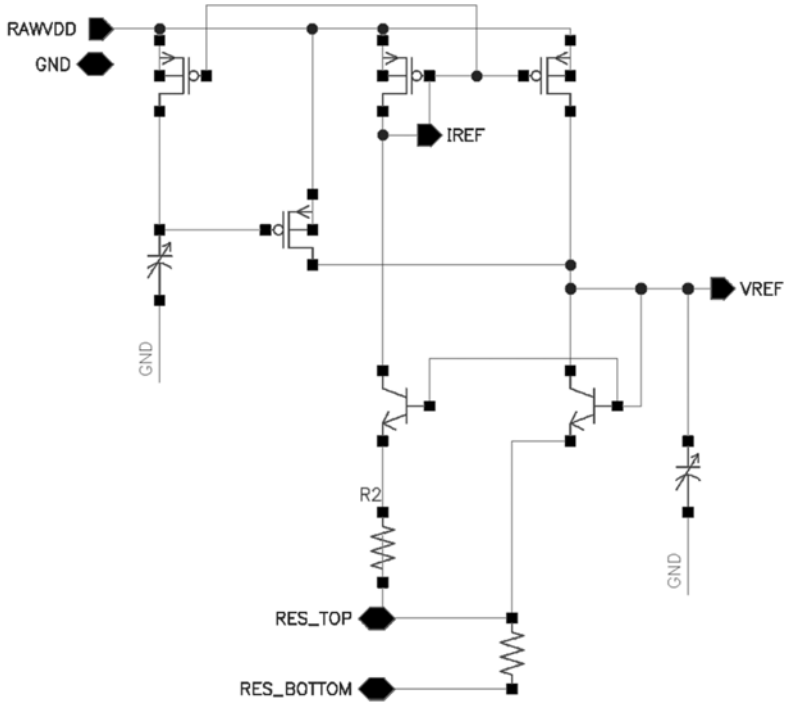

Figure 22: Bandgap reference cadence virtuoso schematics with auto start function implemented by M2 and M3 PMOS transistors.

The circuit consists of two bipolar transistors with different emitter areas (x2.5 difference in width) where the transistor with a larger emitter area requires a smaller base emitter voltage, V_{BE}, for the same current. Both transistors' V_{BE} decrease with an increase in temperature (approx. −2 mV/K) whereas the difference between both transistors' V_{BEs} (ΔV_{BE}) increase with an increase in temperature. The circuit output is the sum of the ΔV_{BE} with V_{BE}. If the ratio between the first, R2, and second, R3, resistors (ratio of 5.3 in our design) is chosen properly, the two opposing temperature coefficients will cancel each other resulting in an output with no temperature dependence. Since the bandgap reference is based on Bipolar Junction Transistors (BJTs) and resistors, it has tradeoffs such as power consumption and layout space.

4.2.2. BIAS generator

Analog or mixed-signal CMOS chips usually require a number of fixed reference currents for biasing amplifiers, determining time constants and pulse widths, powering loads for static logic, etc. [96] This is done by deriving a wide-ranging set of fixed bias currents from a single master current source according to figure 23.

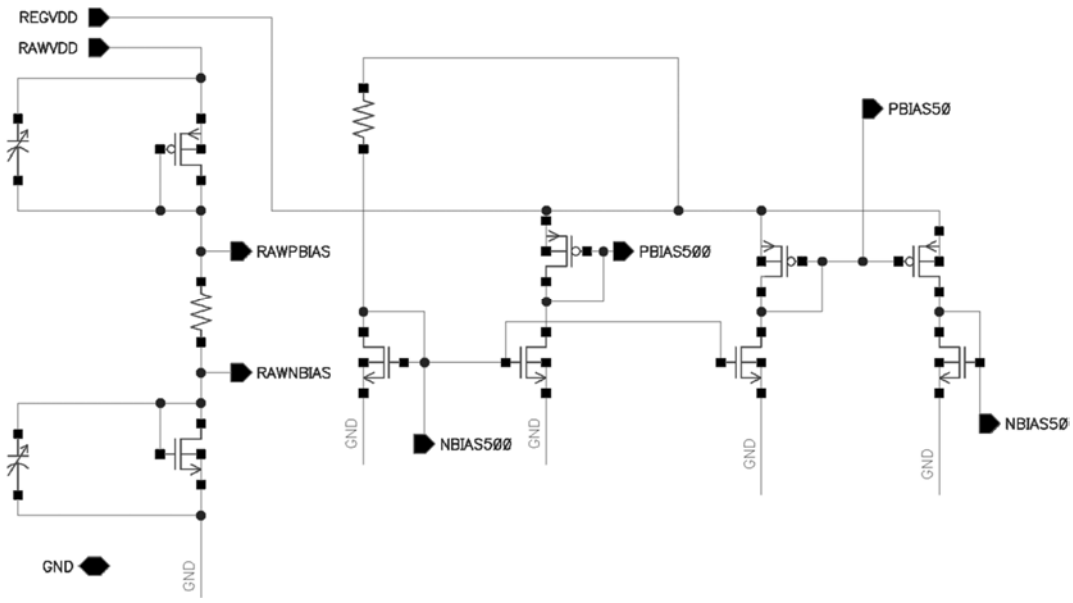

Figure 23: BIAS block for the rawbias (copied using the unregulated power supply of 2.5 V) and 50 nA current bias copied from the regulated supply voltage. Schematics printed from cadence virtuoso.

The chip is operated in the sub-threshold regime (bias currents per device of approximately 50 nA) and has been shown to consume only 76 µW [22] during simulation.

4.2.3. Pressure-to-frequency converter

The simplified diagram of the pressure-to-frequency block [figure 21 b)] illustrates the sampling modulation principle. The pressure transducer will be temporarily powered and generate a sampling voltage (V_S) which will then be converted into a current by a transconductance amplifier, G. The current will be integrated in C_1, and C_2, until the threshold of amplifier A is reached and V_{P2F_out} (P2F) goes high. The feedback loop in amplifier A ensures that as soon as V_A reaches the threshold of A, it is increased by an amount proportional to $regV_{dd}[C_2/(C_1+C_2)]$ avoiding jitter [86]. Every transition of V_{out} will reverse the power supply to the transducer provoking the current to reverse. Once the threshold of amplifier A is reached again, both capacitors will discharge at the same rate as they were charged. Thus the circuit is a resistor controlled oscillator (RCO) that functions as an analog-to-interval converter based on the integrate and fire principle

(I&F) [93, 94]. The circuit uses a feedback from the output of amplifier A to the input of the transconductance amplifier through a low-pass RC filter which replaces the second branch of the Wheatstone bridge. Since the acquisition time is not extremely important (hydration being a "slow" biological event ranging from minutes to hours) a high time constant can be used eliminating low frequency noise (1/f). In order to reach values close to GΩ for the feedback resistor, Häfliger & Johannessen [93] used the transistors' gate leakage saving layout space and energy while cancelling 1/f noise and G offset. The low-pass feedback to the transamp (V_{zero}) attempts to match the average of V_{out} keeping the duty cycle at 50% avoiding nonlinearities (figure 24).

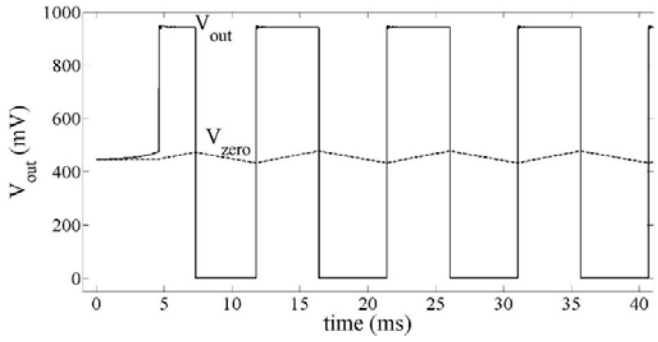

Figure 24: Drawn line: Vout. Dashed line: Vzero. Schematic simulation.

The chip has been shown to consume only 76 µW [22] by powering the sensor for a short period (approximately 13µs) and performing a sample and hold (S&H) [93] according to figure 21 b) & figure 25.

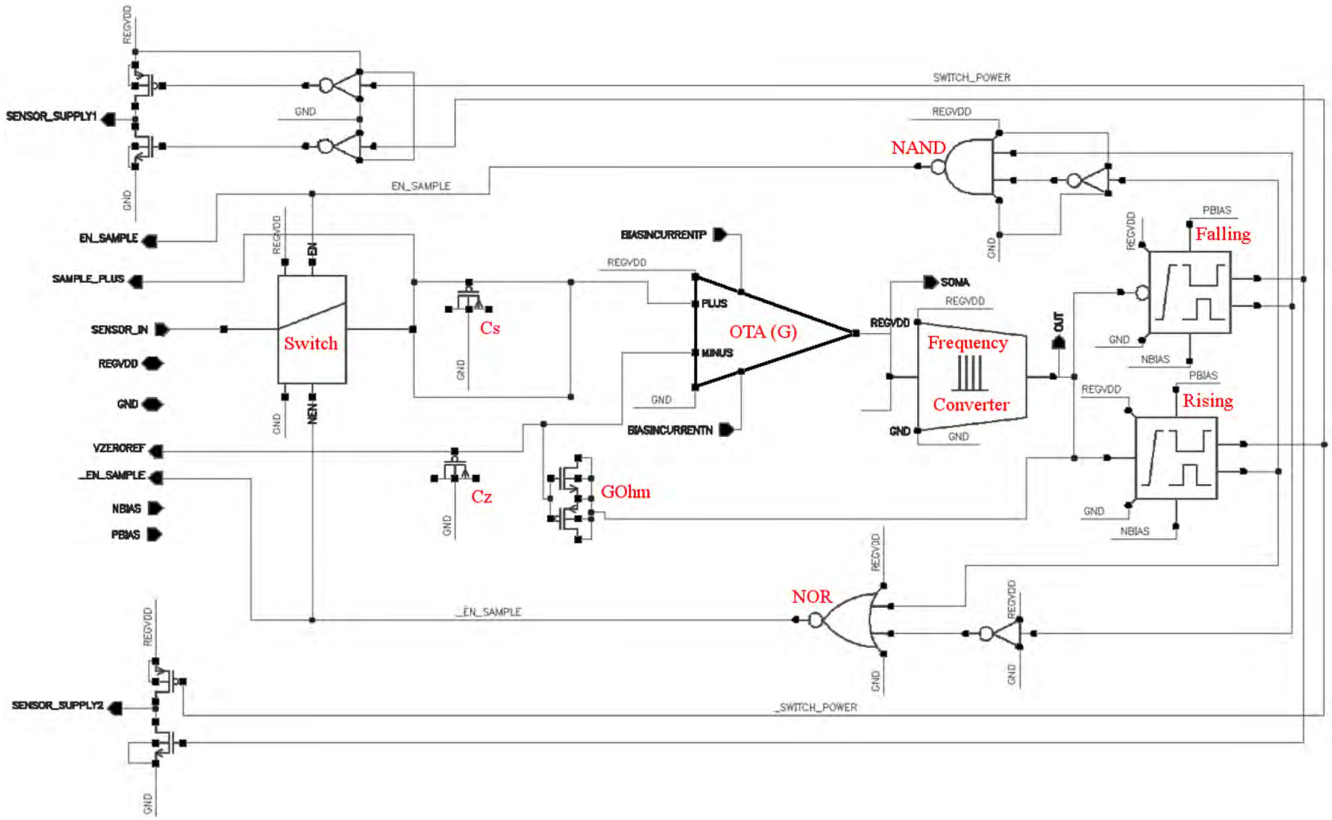

Figure 25: Pressure-to-frequency block schematics printed from cadence virtuoso (TSMC 90nm). Output "OUT" is the frequency modulated signal that translates the voltage input variations that are proportional to the osmotic pressure changes.

The schematics of the P2F block presented in figure 25 show, on the left, different input/output pads for the different signals handled by the same block. The signal travels through a sample and hold (S&H), made by a switch and C_S, into the OTA and to the current-to-frequency converter which outputs a signal with a frequency proportional to the OP recorded by the pressure transducer (not shown in figure 25). The power to the pressure transducer is then switched by using a signal edge detection block (one is inverted), i.e., through a series of logic (not represented) the output can be low, or high, depending if the output signal edge is rising or falling. The output represented with a longer period (shorter frequency) is used to switch the power to the pressure transducer (*switch_power* and *_switch_power* lines) while the shorter period (higher frequency) output is used to power the switch block by enabling or not enabling the signal sampling. In last, the GOhm resistor on the feedback of the OTA is simulated by shorting the source, drain and bulk together of a PMOS and NMOS.

4.2.4. Temperature monitoring

Temperature variations will change the OP, according to (14), which makes it an important variable to record. A temperature monitoring circuit was therefore integrated using the linear dependency of R_2 in the bandgap reference circuit (figure 33) with temperature. The circuit's temperature sensitivity is characterized in figure 34.

4.2.5. Layout

The circuit layout presented in this paper measures 565x265 μm^2, on a chip measuring 1x1 mm (figure 26), and represents an adaption to a new CMOS processing technology and the specific sensor input of the architecture presented in [93, 94].

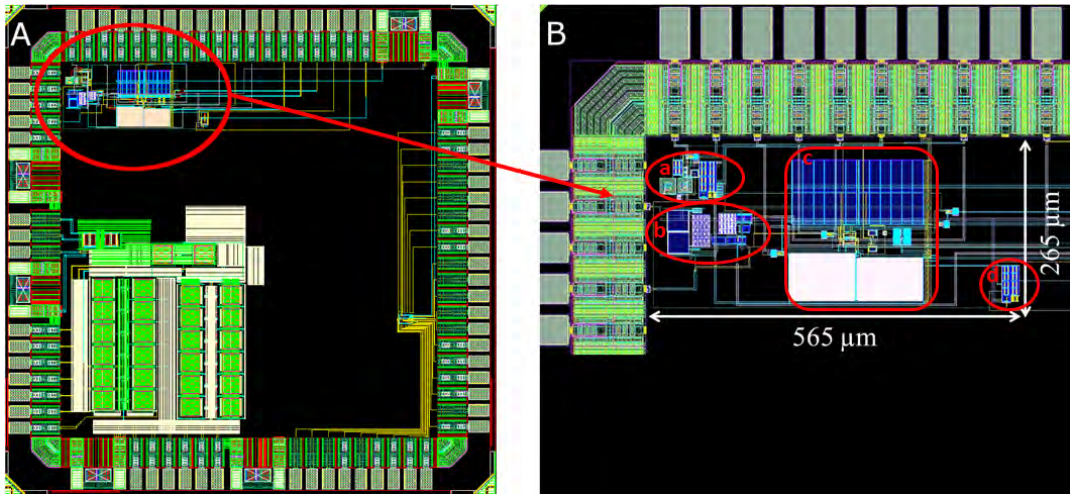

Figure 26: (A) The red circle is marking the ASIC and is zoomed in (B). In (B) one can see the different blocks marked with circles where: a) is the bandgap reference together with the power regulator, b) is the bias, c) is the pressure-to-frequency (P2F) and d) represents an inverter for the output signal.

The different colors (figure 26) are showing different metal layers that can only be differentiated using specific colors.

4.2.6. Integration

Two substrates measuring 10 x 10 mm were microfabricated on a 4'' silicon wafer in order to accommodate the pressure transducer, the ASIC and some necessary surface mounted devices (SMD). While the ASIC and pressure transducer were bonded to the first substrate, the SMD were bonded to the second substrate that was interconnected to the first using a Teflon coated wire containing 10 leads (Wire Technologies, USA) according to figure 27.

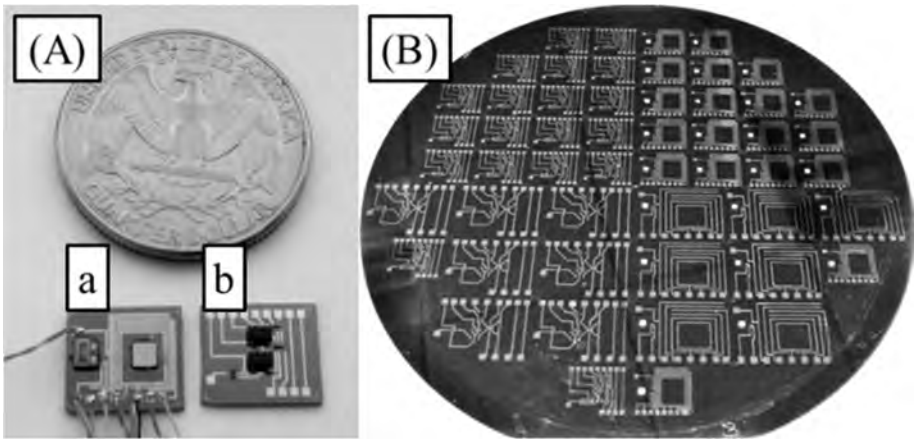

Figure 27: (A) 10x10 mm2 substrates (x2) which contains (a) the ASIC and pressure transducer(s), and (b) the SMD's. (B) Substrate pattern on a 4" wafer prior to dicing.

The leads were soldered to the gold contact pads on the substrates using a low temperature melting solder such as the rose metal alloy (50Bi, 28PB, 22Sn) in order to avoid the gold from evaporating. The same Teflon coated wire was used to connect the power resulting in a transdermal wire if the hydration sensor were to be implanted.

5. Materials and Methods

This chapter focus mainly on the methodology implemented in building and characterizing *prototype 3* of the OHS, however, there were independent tests performed on the permselectivity of different semi-permeable membranes (with *prototype 1*) and the ASIC characterization / properties, including the characterization of the pressure transducer, (with *prototype 2*). The list of materials used in the fabrication of the OHS device are given in Table IV:

Table IV: Materials purchased and suppliers.

Material	Supplier	Land
Acetal rod (Ø 25mm)	RS	UK
Membrane Support Disc	RS	UK
PCB	RS	UK
SMD	RS	UK
PBS solution	Sigma-Aldrich	USA
USB 6009 DAQ	National Instruments (NI)	USA
Wire bonder Delvotek 5610	F&K (available at Norfab, Norway)	Austria
Pneumatic/hydraulic hand pump	GE Druck	Austria
Temperature cycler VT series	Weiss Technik (available at Norfab, Norway)	Belgium
Substrate wafer	Norfab	Norway
Mask aligner	EV group (available at Norfab, Norway)	Austria
Etching chemicals / Developers	MicroChemicals (available at Norfab, Norway)	Germany

Measurable beaker	Biltema	Norway
Silicone Compound 3140	Dow Corning	USA
Araldite 2020	Huntsman	UK
Glob top epoxy	EPO-TEK	USA
Nafion membrane N115 (5 mil)	Ion Power	USA
Nafion membrane NR211 (1 mil)	Ion Power	USA
ePTFE membrane QBV657EXP4D	Able Seal and Design	USA
Silon membrane 2-5 mil	Bio Med Sciences	USA

5.1. Membrane investigation

The membrane tests were performed using *prototype 1* of the OHS and an absolute pressure sensor (HSCSAND030PAAA5, Honeywell, USA) was used to record the OP with a voltage output.

The sensor was first assembled in a RS containing a balanced hydration level of 280 mOsm L^{-1}. Once an equilibrium was reached (0 bar), the media solution was changed to a level of 20 % overhydration (220 mOsm L^{-1}) to provoke a water diffusion from the medium into the RC increasing, therefore, the pressure inside the RC. This was repeated 3 times for each membrane (figure 30).

5.2. ASIC

As previously written in this thesis, the main focus of the ASIC design was to implement it in TSMC90nm processing technology and try to improve the SNR of the circuit. Two possibilities were related to the BIAS block dependency on the unregulated power supply (2V – 4V) and the PSRR of the OTA (G) according to figure 21. The ASIC provided us with the front-end interface of the OHS converting the changes in pressure to a

frequency output according to figure 24 making a RCO due to the nature of the pressure transducer (Wheatstone bridge resistor). One of the most noteworthy aspects of this circuit's layout lays on the fact that the feedback resistor to the OTA, making a low-pass filter, uses the gate leakage of a PMOS, and NMOS, transistors to simulate a GOhm resistor that would otherwise consume more layout space (section 6.2.2) resulting in a higher power consumption, an increase in noise and cost.

Following the circuit architecture presented in section 4.2, the schematics was transferred to the TSMC90nm technology adopting new models with slightly different rules and parasitic parameters. After all errors were fixed, a simulation took place to test the circuit.

5.2.1. SNR

The method implemented to measure the SNR, was to calculate the output frequency variation, Δf_{out}, for the maximum pressure difference (maximum signal). First, for an unregulated supply, V_{raw} = 2 V, and finally for V_{raw} = 4 V. The difference in frequency will correspond to the noise level. In this way, two BIAS blocks were implemented where $BIAS_{raw}$ corresponds to the dependency of the bias currents on V_{raw} and BIAS corresponds to the block eliminating the bias currents dependency on V_{raw}, according to figure 23, with a direct influence on the P2F block (Table VII).

Another technique used, in order to achieve a better SNR figure, was to power the sensor for a short period (approximately 127 µs for each transition of V_{P2F}) which permits the polarity of the sensor supply to be switched and a single sample and hold step to be performed.

5.2.2. PSRR

The next step consisted in evaluating the PSRR for the OTA (G on figure 21) according to the approach used in [88, 97]. The power supply variation introduces a current in the circuit so it does exist a power supply transconductance, Gm. This current is then

converted into some voltage at the gain node (only one for each circuit) with the same gain as the signal transfer function. For this reason, the PSRR can be defined by the ratio of the signal transconductance (Gm(s)) and the power supply tranconductance [$Gm_p(s)$]. When increasing the Gain Bandwidth (GBW) of the OTA, A(s) increases, increasing the PSRR according to (40). PSRR can be normalized to $2\pi GBW/s$ for $f > f_{dominant}$ resulting in the parameter $1/A_p(s)$, known as PSR (reciprocal of the power supply gain). PSR, for high frequencies, is a constant.

An OTA has two power supplies, V_{dd} and V_{ss}, then the PSRR for each of the power supplies can be defined ($PSRR^+$ and $PSRR^-$). However, for our OTA, V_{ss} is GND meaning that there is no $PSRR^-$ contribution. Therefore, according to the setup in figure 28 one can simulate, using cadence, the PSRR.

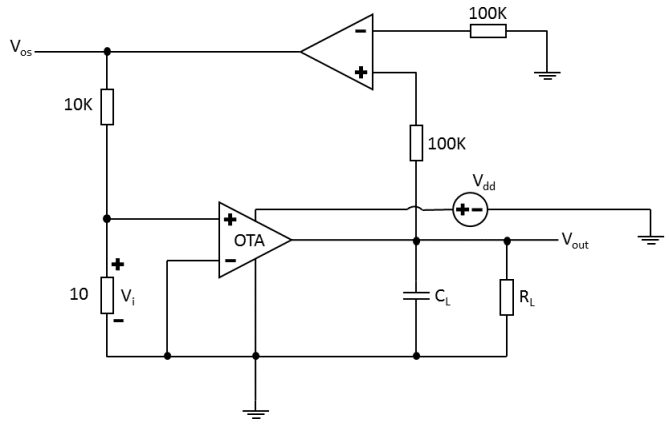

Figure 28: General schematic configuration for studying $A_{open\ loop}$, CMRR and PSRR of Op amps [97]. The inverter used for finding the offset voltage (V_{os}) is an ideal op-amp written using verilogA in cadence.

It is applied an AC magnitude of 100 mV, with a 1 V offset, to Vdd accomplishing a sinusoidal signal between 900 mV and 1100 mV at a frequency of 13.5 MHz (transmitting power frequency).

From (40) one can calculate the $PSRR^+$ according to:

$$PSRR^{+} = \left|\frac{A_{vd}}{A_{cm}}\right| = \frac{V_{out}/V_{id}}{V_{out}/V_{dd}} = \frac{V_{dd}}{V_{id}} \quad (45)$$

Where $V_{id} = V_i$ and $V_{os} = 1000V_i$ hence $V_{id} = 1000V_{os}$, providing:

$$PSRR^{+} = \frac{V_{dd}}{\frac{V_{os}}{1000}} = \frac{1000V_{dd}}{V_{os}} \quad (46)$$

Important to notice that the PSRR should be studied at the frequency of the supply voltage and not at the GBW of the OTA. Since the transmitting power frequency used previously in [22] is 13.5 MHz, this was the frequency of the AC signal used for this simulation.

5.2.3. Temperature monitoring

The bandgap temperature sensitivity was measured by placing the ASIC (mounted on a test PCB) inside a climate chamber (VT series, Weiss Technik, Belgium) where the temperature was cycled from 10 ºC to 50 ºC during 30 minutes and sampled at a 15 s sampling rate (figure 34).

5.3. ASIC implementation & Characterization

In order to test and characterize the ASIC, the pressure transducer had to be mounted on a custom made PCB with different test points (test PCB). In order to accomplish a full test platform for the ASIC and transducer, the pressure transducer was mounted on the test PCB made in the electronics lab at HBV. It was fixed in position using an epoxy (Araldite 202, Huntsman, UK) and wire bonded to the substrate (cooper pads with tin

plating to protect the cooper from oxidation) using a semi-automatic wire bonder (Delvotic 5610, F&K, Austria). In the end, the bonding pads were protected using glob top (T7139, EPO-TEK, USA). A small hole through the PCB allowed access to the back of the pressure transducer and a custom made ¼'' tube inlet (made in acetal in the mechanical workshop at HBV) was mounted using araldite 2020. The pressure transducer was then connected to a pneumatic hand pump (DPI 104, GE Druck, UK) and the applied pressures were recorded with the ASIC. The pressure was changed over a range of 0-2 bar (dynamic range) in 100 mbar increments (figure 35).

5.4. Temperature dependency

The impact of temperature on OP was tested with the previously used climate cabinet (VT series, Weiss Technik, Belgium) for a temperature span of 40 ºC according to figure 36.

5.5. Packaging

The fabrication & integration of the encapsulation together with the membrane and substrate (including the pressure transducer plus SMD and ASIC) was done in different fabrication steps and is here described.

5.5.1. Prototype manufacture (tools)

The sensor was fabricate using a lathe (Bradford Lathes, USA) to turn, and bore, an acetal rod to the dimensions shown in figure 19. The slot for inserting the double layer substrate was made using a milling machine (Bridgeport, USA). Both machines were manual, used high speed steel tool bits (HSS), and available at the mechanical workshop at HSN. Acetal is a biocompatible material, with a strong tensile strength, and chemical resistant which permits it to be autoclaved. The membrane support disc used was the same as the one described in [22], made of stainless steel (316 L).

5.5.2. Substrate preparation

In section 5.5 it was described how the encapsulation was fabricated using an acetal rod and machining it to the desired dimensions. However, a very important part of the packaging process is the fabrication of the substrate that will include the pressure transducer, the ASIC, the external SMD and the contact pads for powering and sampling the interface that is shown in figure 27. The bonding pads of the ASIC were electrically connected to the substrate, using a semi-automatic wire bonder (Delvotic 5610, F&K, Austria), and protected with a glob top epoxy (T7139, EPO-TEK, USA). In order to keep a small footprint, it was decided to use two substrates in a "sandwich" assembly, meaning that a) is placed upside-down on the top of b) according to figure 27 A. The electronic components are protected with silicone compound sealant (3140, Dow Corning, USA) to avoid moisture diffusing inside as well as immobilizing the substrates. The final substrate assembly is then attached to the encapsulation using a two components epoxy (Araldite 2020, Huntsman, UK) which, on a second step, fills up the cavity containing the substrate in order to fixate part of the wire so that there is no stress on the soldering pads. The OHS was then integrated in a beaker on the top of an ASIC test PCB platform according to figure 29 in order to test/validate the sensor.

A <100> 4'' wafer was purchased from the Norwegian micro- and nanofabrication facility (NorFab) with a 600 nm layer of SiO2 (double sided), a 50 nm layer of NiCr (adhesion layer on top side) and a 500 nm Au layer (on the top of the NiCr layer) (figure 27 B), according to Table V. The microfabrication steps implemented are based on the following techniques:

- Spin deposition of photoresist
- Pre-Baking
- Photolithography
    - Alignment
    - Exposure
- Development
- Photoresist Stripping
- Post-Baking (Hard Bake)
- Etching

These steps were repeated for each side of the wafer according to the pattern on the wafer.

Table V: Microfabrication steps for the making of the substrate.

Step	Schematic	Process	Parameters	Side	Supplier
1		•Thermal oxidation. •NiCr deposition. •Au deposition.	• 600 nm SiO_2. • 50 nm NiCr. • 500 nm Au.	Both	Norfab
2	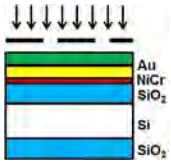	•Photoresist spin deposition. •Photolithography.	• Spin deposition of positive photoresist S1813 at 3000 rpm for 60 s (acc. 1000 rpm/m). • Photolithography exposure time of 40 s (soft contact).	Top	Shipley (USA) Norfab
3		•Development. •Gold etching.	• Development for 2 minutes with trichloroethylene (TCE). • Gold etching for 1m35s.	Top	µChemicals (Germany)
4	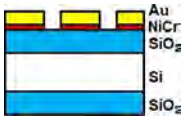	•Photoresist stripping. •NiCr etching.	• Photoresist removal S1165. • NiCr etching for 2 minutes.	Top	µChemicals Shipley (USA)
5	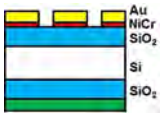	•Photoresist spin deposition.	• Spin deposition of positive photoresist S1828 at 1500 rpm for 5 s and 3000 rpm for 33 s (acc. 1000 rpm/s).	Bottom	Shipley (USA)
6	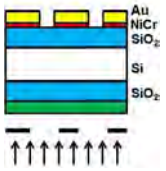	•Bottom mask alignment and photolithography. •Development of S1828.	• Same as in step 2. • Development for 2 minutes.	Bottom	Norfab

7	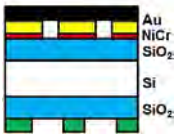	•Wafer placed on wafer holder.	• Wafer cover for top side protection.	Top	Norfab
8		•SiO_2 etching. •Photoresist stripping.	• SiO_2 etching with Wet Buffered Oxide Etch (BOE) for 8 minutes. • Same as in step 4.	Bottom	Norfab
9		•Bulk etching with 25% TMAH.	• At 90 °C for 10 hours.	Bottom	Norfab
10	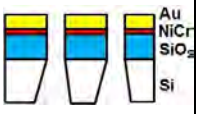	•Wafer holder removal.		Top	Norfab

The fabrication procedures in Table V were performed at the MST lab, and the NTNU NANOLAB, as part of the Norfab laboratory group, Norway. In order to have a more detailed overview of the different steps, it is here described complementary information for each step:

Step 1 – It was performed at NTNU NANOLAB where the wafers were purchased from, with metal layers deposited. The NiCr acts as an adhesion layer, and diffusion barrier, for the gold (Au) on silicon dioxide (SiO_2).

Step 2 – Photoresist is spin deposited on the prepared wafer and baked for 2 minutes at 100 ºC on a hot plate. For the photolithography process, a mask aligner (EVG620, EV group, Austria) was used.

Step 3 – After development, gold etching was performed using HCl/HNO_3 with a mixing concentration 1:3 (*aqua regia*).

Step 4 – After the photoresist removal, it was used diluted sulfuric acid (H_2SO_4 96% aqueous) heated at 100 °C to etch away the Nichrome (NiCr).

Step 5 – After spin deposition of positive photoresist, the wafer was baked for 2 minutes on a hot plate at 100 ºC.

Step 6 – Development performed using the same trichloroethylene (TCE) solution as in step 3.

Step 7 – The wafer cover was a mechanical wafer holder for a single wafer with backside protection. These are made of Polyether ether ketone (PEEK) material.

Step 8 – SiO_2 is etched away before etching the Silicon (Si) in order to open a hole through the wafer.

Step 9 – It was used a Tetramethylammonium hydroxide (TMAH) solution to etch the bulk / Si. The solution will also etch away the SiO_2, reducing its thickness. For this reason, according to [98], the SiO_2 etch rate for a 20% TMAH solution (at 80 °C) will be less than 50 nm/h and the etching rate of the Si will be 40 µm/h. This way, after etching a hole through the 525 µm Si wafer one will still have approximately a 550 nm layer of SiO_2. A higher percentage of TMAH and a higher temperature permitted accelerating the etching process.

The lithography process was performed for the layout design where the holes made on the wafer (using TMAH solution) intention was to provide access from the solution to the pressure transducer in order to record the OP.

5.6. Test and validation of osmotic hydration sensor

The MEMS transducer is able to record the hydrostatic pressure resulting from the water diffusion through the semi-permeable membrane to/from the RC through an access channel in the RC that allows the fluid to come in contact with the pressure transducer according to figure 19. The hydrostatic pressure will be proportional to the OP created by the difference in salt concentration between the RS and the media solution. The experimental procedure is here presented as the steps necessary to perform a validation test of the sensor consisting on the following stages:

- Reference solution preparation
- Membrane preparation
- Sensor assembly in reference solution
- Sensor “bleeding”
- Sensor validation

An illustration of the experimental setup is shown in figure 29.

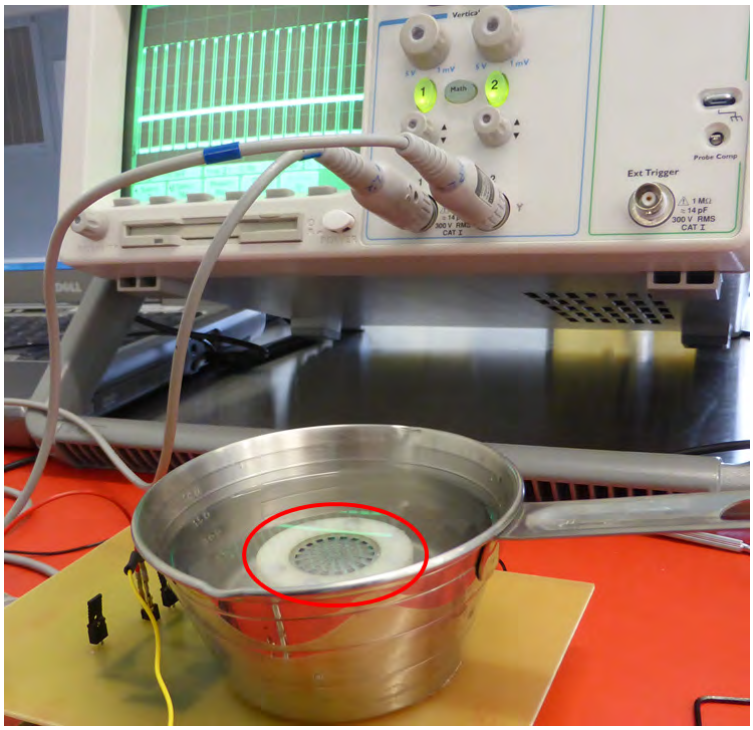

Figure 29: Experimental procedure for validation of the OHS (marked in red).

5.6.1. Reference solution preparation

The RC is filled up with a RS with the same osmolarity of the blood (serum osmolality) for a normal hydrated person by dissolving a PBS powder in 1 L DI water. We use a PBS solution (P5368, Sigma-Aldrich, US) that has the same OS as the BF. The concentration of sodium chloride in PBS is [NaCl] = 137 mmol L^{-1} while the concentration of potassium chloride is [KCl] = 2.7 mmol L^{-1}. One can calculate the total OS, for one litre of solution according to (16) giving a total osmolarity equal to 279.4 mOsm L^{-1}. This is slightly inferior to the theoretical value, however, we are neglecting other salts present in the PBS solution that will increase the OS of the RS.

5.6.2. Membrane preparation

The membrane was initially cut, using a scalp tool, to a square shape and left to hydrate in DI water in order to account for expansion that might occur to the membranes in DI

water. Afterwards, the membrane was placed over the membrane support disc and trimmed on the edges in order to get a circumference shape with the same diameter as its support disc. The membrane, plus support disc, were then integrated together with the encapsulation and an O-ring was used in order to help holding the membrane in position and help sealing the RC according to figure 19.

5.6.3. Sensor assembly in reference solution

The sensor is assembled and immersed inside a PBS solution and will record an equilibrium pressure of 0 bar. Once the salt concentration of the media increases (dehydration), or decreases (overhydration), the permeate will diffuse through the semi-permeable membrane out of the RC, or into the RC, respectively trying to reach a chemical equilibrium (osmotic equilibrium). The relation between the salt concentration and the OP is given by Henry's law according to (14) [22].

5.6.4. Sensor "bleeding"

In figure 19 one can observe a pressure release valve/screw which function is to release the excess pressure created inside the RC when assembling the sensor inside the PBS solution. This process is here described as the sensor "bleeding" where excess RS is leaked outside in order to equilibrate the pressure inside the RC with the pressure outside the encapsulation, that is proportional to the media fluid (PBS) height plus the atmospheric pressure.

5.6.5. Sensor validation

In order to validate our sensor an experiment simulating ±20% hydration change was conducted, and the output frequency from the OHS was recorded. From previous work [90], the characterization curve (frequency output vs pressure) is given by (47):

$$Pressure_{osmotic} = \prod = 323\left(f_{out} - 8.9 \right) \quad (47)$$

For this experiment we characterized the hydration sensor for ±20% variation in hydration which corresponds to a Δosmolarity = ±60 mOsm L^{-1} (sensor's dynamic range). The sensor was immersed, and assembled, inside a beaker containing a PBS solution with 20% higher salt content in order to simulate a state of serious dehydration. After "bleeding" the sensor, the media was replaced by another PBS solution with the same osmolarity as the blood in the human body (approx. 280 mOsm L^{-1}) and the sensor's response was recorded. Before replacing the semi-permeable membrane according to the procedure described in [5], the same procedure was repeated two times: firstly, for reaching a serious state of overhydration (approx. 220 mOsm L^{-1}), and secondly, for reaching a serious state of dehydration (approx. 340 mOsm L^{-1}) which corresponds to the initial equilibrium state. Therefore, we study the sensor's dynamic response for a change in osmolarity from 220 to 340 mOsm L^{-1}, from over- to dehydration (ΔOsmolarity = ±60 mOsm L^{-1}) which corresponds to a variation in the OP of ±1.49 bar according to (3). However, since the membrane retentate are the anions only, mainly Cl^-, our OP variation is reduced by half to ±745 mbar. This procedure is repeated 3 times in order to have statistical valid results.

It was also used different semi-permeable membranes in order to analyze one that provides a better resolution, i.e, the membrane that allows recording the highest OP. This was done by recording 20% change in hydration for the Nafion, ePTFE and Silon membranes. The Nafion membranes used were the 5 mil N115, and the 1 mil NR211, from DuPont (IonPower, USA) while the ePTFE used was the 5 mil QBV657EXP4D from GE Energy (Able Seal and Design, USA) and the Silon membrane thicknesses tried out were 2, and 5, mil (Bio Med Sciences, USA).

One final experiment was to show the OP dependence on temperature according to (14) . In order to show this, an OP was induced, by changing the media, and the temperature was set to vary between 10 °C to 50 °C through a 2 hour period. The temperature was

cycled with a climate chamber (Weiss Technik 64, Weiss Technik, Belgium). In order for this experiment to work, the sensor had to be in equilibrium.

All experiments were repeated 3 times at 37 °C and the data was collected using a USB 6009 data acquisition (DAQ) card connected to a pc equipped with LabView software (NI, USA).

Note: 1 mil is a thousand of an inch (0.001 inches) and is equivalent to 0.0251 mm (25.4 μm).

6. Results and discussion

6.1. Membranes

The sensor response to a change in 20% hydration equipped with different membranes is shown in figure 30. Both Nafion N115, and NR211, are able to record an OP of 270, and 520, mbar respectively while the ePTFE only records a low 40 mbar. The N115 has a response time of approx. 7 hours but the NR211 can reach 100% signal in approx. 5.5 hours. On the other hand, the ePTFE response time is approx. 10 hours.

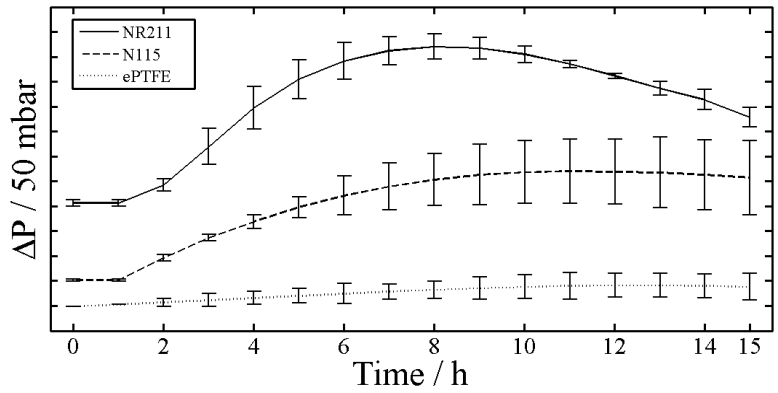

Figure 30: Osmotic pressure response from the Nafion N115 (127 µm, Nafion NR211 (25.4 µm) and the ePTFE QBV657EXP4D (127 µm).

6.1.1. Ion-exchange membranes

The sensor is capable of recording OPs similar to the theoretical values using the Nafion NR211 membrane. The thinner NR211 provides a faster response time over the N115 and permit the sensor to record a higher OP before the pressure decrease most likely due to an efflux of counter ions according to [5]. One must take into consideration that a ΔOsmolarity = ±60 mOsm L^{-1} corresponds to a variation in the OP of ±1.49 bar according to (14). However, since the Nafion membrane is a proton exchange membrane, it allows cations to diffuse across it while blocking the anions (Cl^-). The OP

changes are reduced by half, resulting in an effective ΔOsmolarity = ±30 mOsm L^{-1}, instead.

From figure 31 and Table VI it is noticeable a significant Na^+ contamination meaning that the membrane sulfonate groups ($SO3^-$) are bonding to sodium (NaSO3) releasing H^+ ("hoping" between different sulfonic acid groups) and changing the conductivity properties of the membrane which will induce an anionic leakage of Cl^- ions. It has been shown that multivalent cations (divalent and trivalent cations) exchange with the polymer network more preferably than monovalent cations affecting the Nafion membrane's conductivity [99]. It is also proved that cationic ions have a higher affinity for the sulfonate acid groups than protons which will affect the conductivity and water diffusion through the membrane [99]. This will change the cations mobility through the membrane and, eventually, neutralize its charge. In addition, the fact that protons are released into the RS, together with sodium, will increase the ionic concentration in the RS more than expected providing an error on the recorded OP.

The performance degradation of the Nafion membranes was examined by investigating the potential for stoichiometric changes in the material composition during its exposure to the physiological PBS solution. Hence, the membranes were subject to Energy-dispersive X-ray spectroscopy analysis (EDS) with the results presented in figure 31. The membranes were rinsed with DI water and dehydrated before examination under the scanning electron microscope (SEM, Philips XL30) and with the EDS scan compared with new and unused membranes.

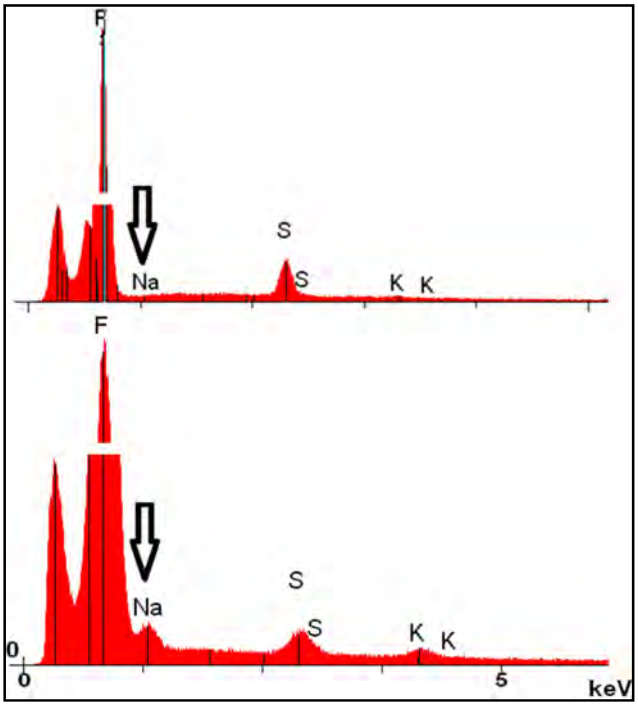

Figure 31: EDS analysis showing the composition of the Nafion N115 membrane before and after immersion in PBS for 60 hours (counts vs KeV) [5].

The EDS results suggest that the composition of the Nafion membrane is modified after exposure to PBS as observed with the clear presence of sodium (Na) and potassium (K) content after exposure. The Na peak indicates a concentration of 6.54 wt% already after 60 hours of exposure to PBS, and the amount of sodium was found to increase with time as shown in Table VI.

Table VI: Nafion N115 contamination with Na

Exposure to PBS (hours)	**Experiment** figure 31	**Na (% wt)**
0	-	0
60	-	6.5
140	1	9.8
200	2	9.9
260	3	10.4

Although there is a clear increase in the sodium concentration as indicated by the weight percent ratio, there is not a direct linear dependency with time, i.e., one cannot clearly differentiate between the quantity of Na between 140 and 260 hours, suggesting that the membrane becomes saturated.

6.1.2. Gas permeable membranes

Since the Nafion membrane is reducing the sensor's signal by half, it was considered that the a vapor exchange membrane, such as Teflon (PTFE), ePTFE and SILON could be better candidates as suggested in prior art published by LeVeen et al. [20]. However, this was not the case and a possible explanation could be related to the transport method through the exchange membranes. The diffusion of water vapor across a dense polymeric membrane consists of three steps: first is the sorption of the water molecule, second is the diffusion across the membrane and finally the evaporation/adsorption of water into the opposite side. The water vapor transport is initially zero, until the moisture concentration on the far side of the membrane becomes greater than zero.

The result is something called the “incubation” period. After the incubation period, the permeate flux through the membrane, J, is given by the sum of the contributions of two forces: (i) the mechanical force due to a pressure gradient and (ii) the chemical force due to interaction of water vapor with the membrane. The flux due to the mechanical force is proportional to the pressure gradient while that due to chemical force is proportional to concentration gradient according to (48) [100]:

$$J = K_1 \frac{\left[\left(c_0 - c_i\right)\right]}{l_0} + K_2 \frac{\left[\left(p_0 - p_i\right)\right]}{l_0} \tag{48}$$

where J is the net flux per unit area and unit time, c_0, and c_i, are the concentrations, p_0, and p_i, are the pressures imposed on a membrane, K_1, and K_2, are constants and l_0 is the membrane’s thickness.

It seems as if the dense backbone structure of gas permeable membranes does not allow water vapor to diffuse fast enough in order to permit recording pressure variations at the time scales used in the current setup (hours). The low diffusion flux of water vapor across gas permeable membranes might be explained according to [100]. The contribution of the mechanical force to permeability increases with a pressure increase, while the contribution of the chemical force to permeability decreases with a pressure increase. This means that the mechanical, and chemical, forces will act against each other keeping the permeability level almost constant, if not, very low. Increasing the temperature does not seem to help since permeability is a product of diffusion and solubility, equation (9). Diffusion increases, while solubility decreases, with temperature respectively creating little impact on the permeability.

As it has been stated before, the Silon membrane was studied as a possible candidate. This membrane combines the properties of Silicone with PTFE, making a membrane with similar properties to Polydimethylsiloxane (PDMS), with Silicone in the backbone making

it more resistant to tensile stress while increasing the permeability to water vapor. However, Silon did not record changes in the OP and was later excluded.

6.2. ASIC

6.2.1. Schematics

During this phase the schematics where transferred to the newer TSMC 90nm processing technology implementing both active, and passive, models available. However, design changes were implemented in order to achieve a better SNR.

6.2.1.1. SNR

The values in Table VII show Δf_{out}, and the SNR, in function of the BIAS block used, where the older block previously developed in [93] (dependent on raw supply voltage, V_{raw}) is here identified as $BIAS_{raw}$. The procedure for calculating the values in Table VII is described in section 5.2.1.

Table VII: SNR values for different BIAS blocks.

BIAS block	**Δf_{out} (%)**	**$SNR_{dB} = 20\log(A_{signal}/A_{noise})$**
$BIAS_{raw}$	7.2	22.8
BIAS	2.9	30.8

One can see that, by eliminating the dependency of the bias currents on V_{raw}, an improvement of 8 dB can be achieved increasing the circuit's resolution by 4.3%. This improvement can be considered significant in regards to the low power operation of the ASIC and sensitivity of the pressure transducer. This was a simulated improvement that

deserved to be implemented in the old circuit design (STM 90 nm) when transferring to the newer TSMC 90 nm technology.

6.2.1.2. PSRR

The OTA is connected according to figure 28 and subject to an AC simulation between 10 Hz and 100 MHz resulting in a $PSRR^+$ according to figure 32. One can see that the $PSRR^+$ is very good, for a frequency of 13,5 MHz, $PSRR^+$ = 94,8 dB and $V_{dd}/V_i = 10^{4,74}$ meaning that, for a ΔV_{dd} = 100 mV, ΔV_i (input variation) = 1,8 µV [PSRR >> 1].

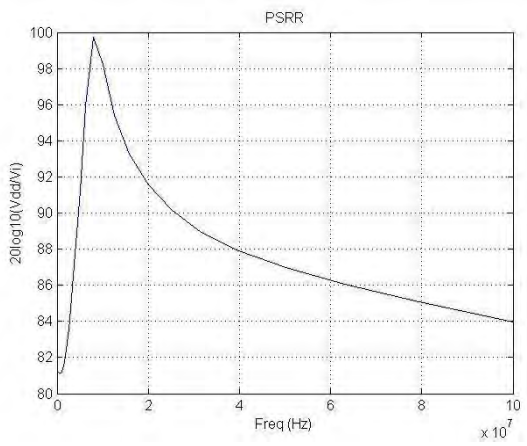

Figure 32: PSRR for the OTA where $PSRR_{dB}$=20log[A (s)/(Ap (s))].

6.2.2. Layout

Preventive measures were taken in order to reduce the layout space (footprint), noise effects and power consumption. This was implemented by using the previous discussed approach, an Analog-to-Analog conversion but also by avoiding power consuming, increasing the thermal noise, components such as resistors for the gate leakage of PMOS, and NMOS, transistors. This permitted simulating a GOhm resistor in order to save power and layout space according to (49):

$$R = R_S\left(\frac{L}{W}\right) \tag{49}$$

Where R_S is the material's resistivity (Ohm/m^2), L is the length and W is the width of the material.

In addition, the capacitors Cs, and Cz, (figure 21) were also replaced by thick gate oxide transistors in order to preserve power. Unfortunately, for the layout simulation, it was not possible to simulate the gate leakage of the transistors implemented as a feedback resistor which originated some uncertainty that could only be checked once the chip was produced. The circuit testing showed that there was an unanticipated leakage current from the gate to ground which had to be accounted for.

6.2.3. Temperature monitoring

Temperature variations will change the OP according to (14) which makes it an important variable to record. A temperature monitoring circuit was therefore implemented based on the difference between the two base–emitter voltages (given by the RESTOP pad) from the bipolar transistors (positive temperature coefficient) according to figure 33.

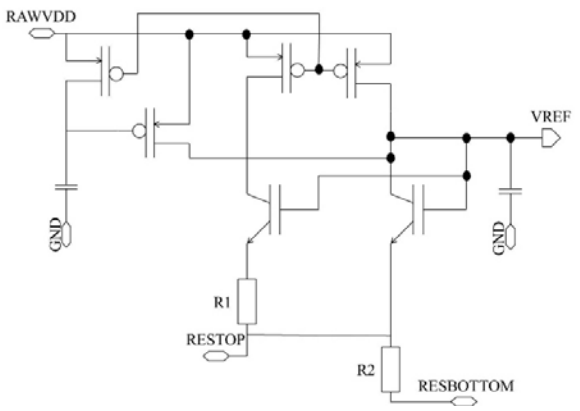

Figure 33: Brokaw bandgap reference with an output voltage around 1.25 V. The voltage across R_1 increases and the voltage across R_2 decreases with temperature cancelling out the V_{REF} temperature dependency.

The results for the voltage output at RESTPOP are given in figure 34.

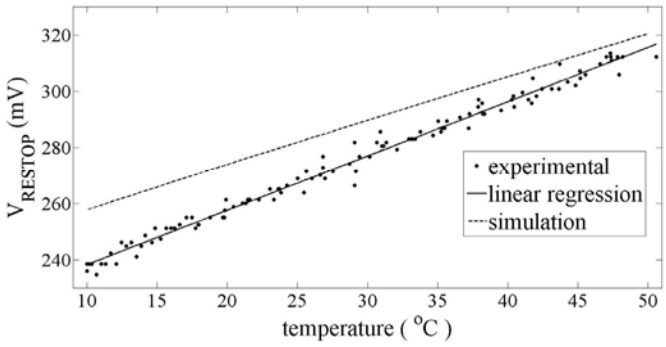

Figure 34: V_{RESTOP} as function of temperature. Temperature measured outside chip encapsulation, not matching temperature of the die (lower).

6.2.4. ASIC implementation

The characterization curve can be observed in figure and gives us the output frequency (f_{out}) in function of the applied pressure to the pressure transducer.

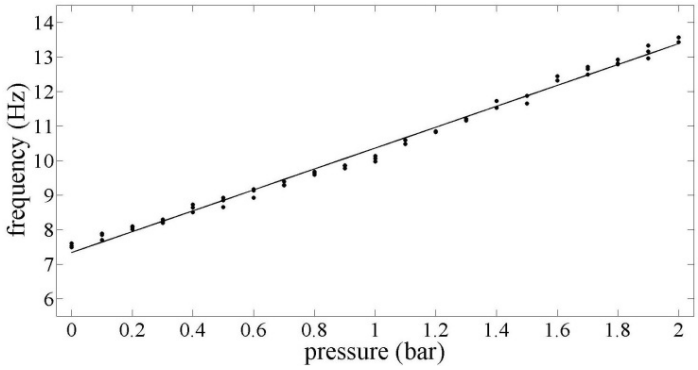

Figure 35: Applied pressure vs output frequency (fout), showing experimental data (dots) and linear regression (solid line), fout averaged over 1 s.

The need to average f_{out} over 1 s results from a leakage to ground that was observed in the feedback node to the transconductance amplifier (figure 21 & figure 25) which was not expected from previous work [93]. This might be due to differences between the STM90nm and the TSMC90nm CMOS processing technologies. It is possible that the thick gate oxide transistors [C_S and C_Z, figure 21], together with the GOhm resistor simulated via a PFET transistor with the gate connected to V_{zero} (figure 21) and the source (S), drain (D) and bulk (B) connected to the opposite terminal, present a "laminar" leakage to GND with the TSMC90nm. This leakage prevented V_{zero} from matching V_{P2F} (not reaching more than 300 mV) causing V_{P2F} not to oscillate. Since V_{P2F} switches after a time proportional to the difference of V_S and V_{zero} minus the offset of G, this was compensated by connecting V_S to ground through an external 1.4 kΩ resistor forcing V_S to approximately 300 mV and making V_{P2F} oscillate. This resulted in a 20% duty cycle instead of 50% (figure 24). Furthermore, during the ASIC test phase, it was noticed a missing pad for the power input of the pressure transducer. This error resulted in

bypassing the logic responsible for powering the pressure transducer (not shown), through two external inverters that sampled the V_{P2F} square wave signal to the transducer's V_{dd} and V_{ss} (inverted). The logic implemented was, therefore, replaced by external SMD however, these were low voltage operated inverters (1 V) powered with V_{reg} (figure 21).

The external correction circuit increased the thermal, and 1/f, noise as well as the power consumption (average power increased by a factor of 10) compared to [93], making it difficult to record pressure intervals bellow 100 mbar. However, averaging the frequency over a 100 ms period improved the accuracy, permitting pressure recordings of 75 mbar (representing 2 % change in dehydration that in turn would reduce the physical performance of an athlete by 30% [3]).

As for the power management, in simulation (i.e. without any fixes for leakage of V_{zero}) the ASIC consumes an average power of 39.4 µW. The transconductance amplifier, G (figure 21), in the pressure-to-frequency block (P2F), is biased in the sub-threshold regime (bias currents of approx. 50 nA). Thus, the piezoresistive pressure sensor itself is the most power consuming unit of the system (167 µW at 1 V supply) but this is corrected by powering it only for approx. 13 µs and using a S&H circuit where the pressure value can be stored. The ASIC power distribution is simulated for a 2.5 V supply using Cadence Virtuoso (Table VIII).

Table VIII: Simulated power consumption for each circuit block.

Block	Bandgap reference	Power regulator	Bias block	Temp.	P2F	Pressure sensor (average)
Power	9.5 µW	14.1 µW	8 µW	1 µW	0.4 µW	6.4 µW

One can see in figure a frequency mean value of <f> = 13.65 Hz with a standard deviation of σ = 0.15 Hz, which gives an accuracy of $ENOB_{SNR}$ = 5.71 bits (see note). The resolution constitutes 52.45 (= 25.71) steps in the dynamic range. Both mean values for the frequency, <f>, and standard deviation, σ, were calculated after recording the frequency 100 times for the maximum error, corresponding to 2 bar.

Note: In this work, it is used $ENOB_{SNR} = \log_2 (A/\sqrt{2}\sigma_{noise}) - (1.76/6.02)$ with A being the signal range and σ the root mean square (RMS) noise contribution. $ENOB_{SNR}$ considers the limitation by noise but neglects any influence of distortion. In [93] a more strict definition was employed: $ENOB_{6\sigma} = \log_2 A / 6\sigma_{noise} = ENOB_{SNR} - 1.79$ where it requires that the LSB for any single sample for a conversion of ENOB bits should be correct with 99.9% certainty [101].

6.3. Temperature dependency

According to (14) a temperature variation of 40 °C should induce an OP change of approx. 200 mbar. The results in figure 36 showed a variation in the OP of approx. 117 mbar, similar to the theoretical results.

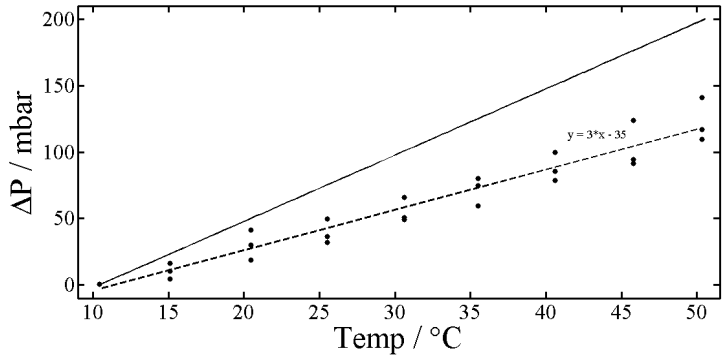

Figure 36: Osmotic pressure variation with temperature. Continuous line represents the theoretical curve while the dashed line represents the experimental fitting curve. Initial osmotic pressure is set at 0 bar.

This is an important environmental effect that is normally neglected however, from figure 36, there is a very big impact from a possible temperature increase due to ASIC, and room, temperature induced changes (normally an increase) that can have a very big impact on such a small volume as it is the case of the RS. This means that there will be a temperature gradient between the media solution and the RS which will reduce the OP reading when the colder media solution (water and cations) diffuse into the warmer RS. In addition, temperature will also influence the diffusion coefficient of the cations through the membrane.

The difference of approx. 83 mbar between the experimental, and theoretical, data observed in figure 36 could, therefore, be explained by a decrease in the osmotic coefficient induced by temperature changes.

6.4. Osmotic hydration sensor characterization & validation

The sensor response over the dynamic range, from 220 mOsm L^{-1} to 340 mOsm L^{-1} is presented in figure 37. The average maximum pressure reached for a state of serious overhydration was 760 mbar (11.2 Hz) while the middle point average, representing normal hydration, was 520 mbar (10.5 Hz). These results are in accordance with a previous developed prototype [5].

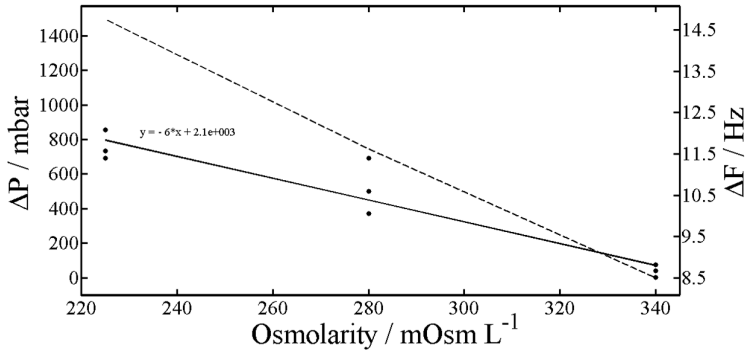

Figure 37: Characterization curve of the hydration sensor from a serious state of dehydration (Osmolarity = 340 mOsm L^{-1}), to a normal state hydration (Osmolarity = 280 mOsm L^{-1}), to a state of serious overhydration (Osmolarity = 220 mOsm L^{-1}). The dashed line represents the theoretical curve while the continuous line represents the experimental curve.

It has been shown in [90] that the hydration sensor is capable of detecting variations in hydration down to 2% [3]. In figure 37 one can see that the standard deviation is not very significant for osmolarities equal to 220, and 340, mOsm L^{-1} however, the same does not happen to osmolarities equivalent to 280 mOsm L^{-1}. This larger deviation could be explained by air bubbles that get trapped inside the RC during assembling, reducing its effective solution volume while increasing the pressure. For this reason, the volume decreases and less water diffuses into the RC (OP effect) limiting the OP recorded. The difference between the experimental, and theoretical, values could be explained by sodium contaminating the Nafion membrane sulfonate group in the backbone as it has

been identified in previous work [5]. Deposition of Na^+ cations in the membrane's backbone seems to be affecting its charge resulting in an anionic (Cl^-) leakage/diffusion across it.

6.4.1. Response time

The response time of the hydration sensor is approx. 5.5 h. This value is a result of different factors such as: temperature, volume, membrane solubility, membrane diffusion and the rate of change in hydration in the human body (slow biological process that the organism takes time in detecting). It was here identified an anionic leakage from the Nafion membrane used which affects the sensor's response time at the leakage's rate (approx. 5 mbar h^{-1}).

Fouling at the membrane surface could also be a reason for the deterioration of the cations conductivity but it is difficult to avoid it in a constant pressure setup. Normally, the industry uses pressure driven setups applying a laminar flow to reduce fouling [102].

An alternative way of negotiating the response time would be to look at the rate of change in pressure (approx. 50 mbar/h for a state of serious dehydration) rather than the absolute change as an indication (and potential severity) of a change in hydration level.

A thinner membrane would provide us with a higher flux (transfer rate) according to (2) , affecting the sensor's response time. However, it is the intrinsic properties of the membranes (solutes retention and water vapor permeability capabilities) that are going to allow recording a higher OP.

7. Conclusions and future work

Merging MEMS with membrane technology and nanoelectronics interface platforms has paved the way towards the development of a new class of miniaturized biomedical sensors that have the potential of tracking physiological markers in real time. It is presented in this thesis a novel hydration sensor based on the principle of OP to target changes in hydration of individuals that can be considered high risk or whom are not capable to consciously notice if they are dehydrated, or overhydrated.

This technology is still at a *proof of concept* level but it shows the possibility to use OP as a signature of hydration over a sensing range of ± 60 mOsml L^{-1} with a resolution capable of detecting a change in hydration of only 2%. All sensor components were based on microfabrication rendering them compatible for future miniaturization into a fully implantable sensor, once the packaging methodology permits a size reduction to the sub 10 mm regime. A significant advantage of such a sensor is that it may replace more complicated, and time consuming, techniques that are currently being used. Further, the sensor concept, based on polymeric membranes for separation of physiological markers of human pathologies, would also work as a platform for similar osmotic sensors measuring other pathologies.

During the prototyping of this device, several key advantages for this approach are evident, including the portability, low power consumption, resolution and miniaturization. All these factors go hand in hand, i.e., the low power interface constitutes a platform for further miniaturization of the sensor which will increase its portability. The membrane retention properties can also affect the sensitivity and response time. Therefore, the three most significant findings of this PhD work are related to the membrane choice (separation/sensitivity), the front-end electronic interface (power/resolution) and packaging (size/microfabrication):

(i) Membrane science offers an enormous potential in the development and integration of novel medical sensors as it is here demonstrated. The use of polymer based biocompatible materials to perform solute separations/filtration is still in rapid development and it presents an excellent alternative to techniques that will increase the complexity of the device, such as, optical, thermal, ultrasound, or conductive parameters. The membrane plays an important role in the detection of hydration, sensitivity and response time. The development of the device is ongoing, and we hope to resolve a leakage issue, due to membrane contamination, during the next iteration of the technology. There are membranes available that could help preventing this downside of our current membrane, including a Nafion membrane in the Na^+ form.

(ii) A significant part of achieving a functional miniaturized device is to aim for an ultralow power device architecture. This was achieved by choosing the new TSMC 90 nm CMOS technology as the basis for the electronic circuit design, combined with the Analog-to-Analog approach implemented with an architecture based on the I&F principle [94]. This approach revealed a low power consumption but with the tradeoff of sensitivity. The low power architecture is imperative for the durability of, for example, a battery operated sensor, but is also important in reducing heat, noise and keeping a small footprint. This circuit's low power architecture reduced the sensitivity by half when powering the pressure transducer at 1 V, instead of the recommended 5 V, but these are tradeoffs that have to be considered during the design stage. This was contradicted by inverting the supply to the transducer at every transition of the output signal which allowed doubling the sensitivity, equation (44). The reason for using 1 V was because it is what the TSMC 90 nm technology provides/uses.

(iii) The packaging process is very important in achieving a miniaturized OHS. By combining an in-house designed miniaturized ASIC with commercially available

SMD, and a pressure transducer sensor, (with very small footprints) it is possible to achieve very small interface platforms to power & sample the sensor. The SMD here used are in the size category 0603 (0.06 x 0.03 inches), however, one can find smaller sizes (e.g., 0101). The dimensions of these devices introduce challenges in packaging (sensor housing) that made the sensor much larger than it could be done in theory. Challenges included the bonding of the ASIC to the substrate as well as the fabrication of the encapsulation. The substrate used proved to be very difficult to wire bond and, in future implementations, one should consider using a different substrate.

The potential of the OHS is enormous and could revolutionize the performance of athletes, and other professionals, with a big physical stress/wear-out by allowing these to exceed the limits that have been stipulated so far without putting at risk their, or others, health. Moreover, it could carefully monitor the hydration level of patients, or other individuals, that are dependent on a third person for their wellbeing. There is also evidence that the OHS could be beneficial for healthy people, with less physically demanding daily routines, due to the importance of a good water balance to keep a good cell function and, in this way, keep an individual healthy (prevention).

8. Outlook

The outlook of the work presented in this thesis can be devided in three main categories:

(i) Membrane

The Cl^- leakage from the Nafion membrane may be addressed by using a Nafion membrane in the Na^+ form, i.e., the Na^+ is bounded to the polymer network (membrane backbone containing the sulfonate groups) in order to avoid ionic competition/contamination that could release protons into the solution (changing the pH value) and changing the membrane polarity that could lead to an anionic leakage. Another approach could be to investigate other membranes (e.g., PDMS).

(ii) *Sensor Interface*

The “laminar” gate leakage to ground detected from the thick gate oxide transistor models in the TSMC 90 nm could be accounted for by replacing these transistor models with, e.g., capacitors and a resistor. This would require more layout space and power consumption but with a tradeoff of noise reduction and increased resolution. The two SMD (inverters) used in the sensor’s interface may be eliminated by adding the power output pads to the pressure transducer on the layout. Finally, adding an RF module would allow implantation.

(iii) *Packaging*

The challenges involving packaging are complex and should be further investigated in order to further miniaturize the sensor. This process could be improved by printing the sensor encapsulation (3D printing), injection molding, or micromachining. In addition to the sensor housing, the electronics platform for the interface could be

reduced in size by integrating all components in the ASIC since the chip had enough layout space available. A thinner membrane, together with a smaller RC volume, may allow a higher diffusion flux and decrease the response time according to Fick's first law of diffusion. Finally, the substrate used could be improved by using a different adhesion layer between the SiO_2 and Au.

These implementations, may improve considerably the sensor's performance. A second generation of the OHS could have a higher sensitivity, a higher resolution and a smaller size. Further miniaturization of the OHS could allow preliminary *in vivo* testing on laboratory animals following the European directive 2010/63/EU for animal welfare. These experiments would be particularly important for the validation and commercialization of the sensor, however, another alternative to implantation could be to use a skin patch with microneedles to sample the BF.

References

[1] S. W. Yeargin and e. al., "Heat acclimatization and hydration status of American football players during initial summer workouts," *J Strength Cond Res,* vol. 20, pp. 463-70, August 2006.

[2] D. J. Casa and e. al., "Influence of hydration on physiological function and performance during trail running in the heat," *J Athl Train,* vol. 45, pp. 147-56, Mar-Apr 2010.

[3] L. E. Armstrong, D. L. Costill, and W. J. Fink, "Influence of diuretic-induced dehydration on competitive running performance," *Med Sci Sports Exerc,* vol. 17, pp. 456-61, August 1985.

[4] H. M. Binkley, J. Beckett, D. J. Casa, D. M. Kleiner, and P. E. Plummer, "National Athletic Trainers' Association position statement: Exertional heat illnesses," *Journal of Athletic Training,* vol. 37, pp. 329-343, Jul-Sep 2002.

[5] L. A. Fernandes, P. Hafliger, M. Azadmehr, and E. Johannessen, "Design and characterization of an osmotic sensor for the detection of events associated with dehydration and overhydration," *IEEE Journal of Translational Engineering in Health and Medicine,* vol. 1, pp. 1-9, 21 August 2013.

[6] T. A. Howell and e. al., "Method and apparatus to sense hydration level of a person," U.S. Patent 8734341 B2, issued Nov. 2, 2006.

[7] Gelfand and e. al., "Patient hydration system with hydration state detection," U.S. Patent 7736354 B2, issud April 21, 2006.

[8] X. Xuedong, "Three-dimensional vertical hydration/dehydration sensor," U.S. Patent 20100145294 A1, issued Dec. 5, 2008.

[9] J. C. Beck and e. al., "An Integrated Wireless Patch for Physiological Monitoring," U.S. Patent 8718742 B2, issued May 23, 2008.

[10] Runze, "Methods and apparatuses for measuring skin properties," W.O. Patent 2009027898 A1, issued Aug. 20, 2008.

[11] Cohen-Solal and e. al., "Method and apparatus for determining hydration levels," U.S. Patent 20100174187 A1, issued Mar. 29, 2007.

[12] C. R. Baker, "Method and apparatus for estimating water reserves," U.S. Patent 8357090 B2, issued Mar. 9, 2007.

[13] S. M. Shirreffs, "Markers of hydration status," *Eur J Clin Nutr,* vol. 57, pp. 6-9, December 2003.

[14] L. E. Armstrong, "Assessing Hydration Status: The Elusive Gold Standard," *Journal of the American College of Nutrition,* vol. 26, pp. 575S-584S, 2007/10/01 2007.

[15] A. C. R. Grayson, R. S. Shawgo, A. M. Johnson, N. T. Flynn, Y. Li, J. Michael*, et al.*, "A BioMEMS review: MEMS technology for physiologically integrated devices," *Proceedings of the IEEE,* vol. 92, pp. 6 - 21, January 2004.

[16] G. Kotzar, M. Freas, P. Abel, A. Fleischman, S. Roy, C. Zorman*, et al.*, "Evaluation of MEMS materials of construction for implantable medical devices," *Biomaterials,* vol. 23, pp. 2737-50, Jul 2002.

[17] C. M. Li, H. Dong, X. Cao, and T. Luong, "Implantable electrochemical sensors for biomedical and clinical applications: progress, problems, and future possibilities," *Current Medicinal Chemistry,* vol. 14, pp. 937-51, 2007.

[18] J. T. Santini, Jr., M. J. Cima, and R. Langer, "A controlled-release microchip," *Nature,* vol. 397, pp. 335-8, Jan 28 1999.

[19] X. Zou, X. Xu, L. Yao, and Y. Lian, "A 1-V 450-nW Fully Integrated Programmable Biomedical Sensor Interface Chip," *IEEE Journal of solid-state circuits,* vol. 44, pp. 1067 - 1077, April 2009.

[20] H. H. LeVeen, E. G. LeVeen, and R. F. LeVeen, "Osmolarity sensor," U.S. Patent 5388449 A, issued July 6, 1993.

[21] M. Gobbi, M. Cowen, and D. Ugboma, "Fluid and electrolyte balance," in *Nursing practice: hospital and home: the adult*, M. F. Alexander, Fawcett, Josephine (Tonks) N. and Runciman, Phyllis J. (eds.), Ed., ed Churchill Livingstone: Elsevier, 2006, pp. 763-785.

[22] E. Johannessen, O. Krushinitskaya, A. Sokolov, P. Häfliger, and A. Hoogerwerf, "Toward an injectable continuous osmotic glucose sensor," *Journal of Diabetes Science and Technology,* vol. 4, pp. 882-92, Jully 2010.

[23] L. E. Armstrong, "Hydration assessment techniques," *Nutr Rev,* vol. 63, pp. S40-54, Jun 2005.

[24] B. Andersson, "Thirst—and Brain Control of Water Balance: Recent research on thirst suggests that sodium-sensitive receptors near the third ventricle participate in the control of the complex balance of fluids in the body," *American Scientist,* vol. 59, pp. 408-415, 1971.

[25] K. King. (2007) Experiment of One: Over hydration: Too much of a good thing? *ULTRARUNNING*.

[26] P. E. Watson, I. D. Watson, and R. D. Batt, "Total body water volumes for adult males and females estimated from simple anthropometric measurements," *Am J Clin Nutr,* vol. 33, pp. 27-39, Jan 1980.

[27] D. Benton, "Dehydration influences mood and cognition: a plausible hypothesis?," *Nutrients,* vol. 3, pp. 555-73, May 2011.

[28] K. M. Chow, C. C. Szeto, T. Y. Wong, C. B. Leung, and P. K. Li, "Risk factors for thiazide-induced hyponatraemia," *QJM,* vol. 96, pp. 911-7, Dec 2003.

[29] S. J. Montain, M. N. Sawka, and C. B. Wenger, "Hyponatremia associated with exercise: risk factors and pathogenesis," *Exerc Sport Sci Rev,* vol. 29, pp. 113-7, Jul 2001.

[30] L. E. Armstrong, W. C. Curtis, R. W. Hubbard, R. P. Francesconi, R. Moore, and E. W. Askew, "Symptomatic hyponatremia during prolonged exercise in heat," *Med Sci Sports Exerc,* vol. 25, pp. 543-9, May 1993.

[31] H. D. Backer, E. Shopes, S. L. Collins, and H. Barkan, "Exertional heat illness and hyponatremia in hikers," *Am J Emerg Med,* vol. 17, pp. 532-9, Oct 1999.

[32] M. M. Grant and W. M. Kubo, "Assessing a Patient's Hydration Status," *The American Journal of Nursing,* vol. 75, pp. 1306-1311, 1975.

[33] A. C., A. Diedrich, and S. R. Raj, "Techniques Used for the Determination of Blood Volume," *Journal of Medical Sciences,* vol. 334, pp. 32-36, July 2007.

[34] E. L. Williams, K. L. Hildebrand, S. A. McCormick, and M. J. Bedel, "The effect of intravenous lactated Ringer's solution versus 0.9% sodium chloride solution on serum osmolality in human volunteers," *Anesth Analg,* vol. 88, pp. 999-1003, May 1999.

[35] G. Ciuti, L. Ricotti, A. Menciassi, and P. Dario, "MEMS Sensor Technologies for Human Centred Applications in Healthcare, Physical Activities, Safety and Environmental Sensing: A Review on Research Activities in Italy," *Sensors (Basel, Switzerland),* vol. 15, pp. 6441-6468, 17th March 2015.

[36] T. G. Pickering, J. E. Hall, L. J. Appel, B. E. Falkner, J. Graves, M. N. Hill*, et al.*, "Recommendations for Blood Pressure Measurement in Humans and Experimental Animals: Part 1: Blood Pressure Measurement in Humans: A Statement for Professionals From the Subcommittee of Professional and Public Education of the American Heart Association Council on High Blood Pressure Research," *Hypertension,* vol. 45, pp. 142-161, January 1, 2005 2005.

[37] W. Hasenkamp, D. Forchelet, K. Pataky, J. Villard, H. Van Lintel, A. Bertsch*, et al.*, "Polyimide/SU-8 catheter-tip MEMS gauge pressure sensor," *Biomed Microdevices,* vol. 14, pp. 819-28, Oct 2012.

[38] A. Moglia, A. Menciassi, M. O. Schurr, and P. Dario, "Wireless capsule endoscopy: from diagnostic devices to multipurpose robotic systems," *Biomedical Microdevices,* vol. 9, pp. 235-243, 2006.

[39] A. El Gamal, "Trends in CMOS image sensor technology and design," in *Electron Devices Meeting, 2002. IEDM '02. International*, 2002, pp. 805-808.

[40] L. Wentai, K. Vichienchom, M. Clements, S. C. DeMarco, C. Hughes, E. McGucken*, et al.*, "A neuro-stimulus chip with telemetry unit for retinal prosthetic device," *Solid-State Circuits, IEEE Journal of,* vol. 35, pp. 1487-1497, 2000.

[41] C. T. Chiang and C. Y. Wu, "Implantable neuromorphic vision chips," *Electronics Letters,* vol. 40, pp. 361-363, 2004.

[42] M. Azadmehr, J. P. Abrahamsen, and P. Hafliger, "A foveated AER imager chip [address event representation]," in *IEEE International Symposium on Circuits and Systems (ISCAS)* Kobe, 2005, pp. 2751-2754.

[43] M. Mahowald, *An Analog VLSI System for Stereoscopic Vision*: Kluwer Academic Publishers, 1994.

[44] T. Delbrück and C. A. Mead, "An electronic photoreceptor sensitive to small changes in intensity," in *Advances in neural information processing systems 1*, S. T. David, Ed., ed: Morgan Kaufmann Publishers Inc., 1989, pp. 720-727.

[45] N. I. Maluf and e. al., "Recent Advances in Medical Applications of MEMS," in *WESCON/96*, Anaheim, CA, 1996, pp. 60-63.

[46] Volvok and e. al., "Membranes and Nanotechnologies," *Nanotechnologies in Russia,* vol. 3, pp. 656-687, 2008.

[47] J. P. Chen, H. Mou, L. K. Wang, and T. Matsuura, "Advanced Physicochemical Treatment Processes," in *Handbook of Environmental Engineering*. vol. 4, ed: Humana Press, 2006.

[48] J. o. G. Crespo, K. W. Böddeker, and North Atlantic Treaty Organization. Scientific Affairs Division., *Membrane processes in separation and purification*. Dordrecht The Netherlands ; Boston: Kulwer Academic Publishers, 1994.

[49] A. D. Revchuk and I. H. Suffet, "Ultrafiltration separation of aquatic natural organic matter: Chemical probes for quality assurance," *Water Research,* vol. 43, pp. 3685-3692, 8// 2009.

[50] R. V. Reis and A. Zydney, "Bioprocess membrane technology (vol 297, pg 16, 2007)," *Journal of Membrane Science,* vol. 302, pp. 271-271, September 15 2007.

[51] H. Chen, L. Yuan, W. Song, Z. Wu, and D. Li, "Biocompatible polymer materials: Role of protein–surface interactions," *Progress in Polymer Science,* vol. 33, pp. 1059-1087, 11// 2008.

[52] N. S. Pereira and P. Klaus-Viktor, *Membrane Technology: in the Chemical Industry*, 2nd, Revised and Enlarged Edition ed.: WILEY-VCH, 2006.

[53] R. D. Noble and S. A. Stern, *Membrane Separations Technology Principles and Applications*, 1 ed.: Elsevier Science B.V., 1995.

[54] S. Loeb and S. Sourirajan, "Sea water demineralization by means of an osmotic membrane," *Advances in Chemistry,* vol. 38, pp. 117-132, 1963.

[55] S. C. George and S. Thomas, "Transport phenomena through polymeric systems," *Progress in Polymer Science,* vol. 26, pp. 985-1017, 8// 2001.

[56] E. C. Suloff, "Sorption Behavior of an Aliphatic Series of Aldehydes in the Presence of Poly(ethylene terephthalate) Blends Containing Aldehyde Scavenging Agents," PhD Dissertation, Food Science and Technology, Virginia Tech, Digital Library and Archives (DLA), 2002.

[57] N. Vahdat and V. D. Sullivan, "Estimation of permeation rate of chemicals through elastometric materials," *Journal of Applied Polymer Science,* vol. 79, pp. 1265-1272, 2001.

[58] A. Paul, T. Laurila, V. Vuorinen, and S. V. Divinski, "Fick's Laws of Diffusion," in *Thermodynamics, Diffusion and the Kirkendall Effect in Solids*, ed Cham: Springer International Publishing, 2014, pp. 115-139.

[59] J. Park and R. S. Lakes, *Biomaterials: An Introduction*, 3 ed.: Springer Science + Business Media, 2007.

[60] M. Hirose, Y. Minamizaki, and Y. Kamiyama, "The relationship between polymer molecular structure of RO membrane skin layers and their RO performances," *Journal of Membrane Science,* vol. 123, pp. 151-156, June 1996.

[61] T. W. Xu, "Ion exchange membranes: State of their development and perspective," *Journal of Membrane Science,* vol. 263, pp. 1-29, October 15 2005.

[62] P. Tremblay, M. M. Savard, J. Vermette, and R. Paquin, "Gas permeability, diffusivity and solubility of nitrogen, helium, methane, carbon dioxide and formaldehyde in dense polymeric membranes using a new on-line permeation apparatus," *Journal of Membrane Science,* vol. 282, pp. 245-256, October 5 2006.

[63] J. Crank, *The Mathematics of Diffusion*: Clarendon Press, Oxford, 1975.

[64] H. Lin and B. D. Freeman, "Gas solubility, diffusivity and permeability in poly(ethylene oxide)," *Journal of Membrane Science,* vol. 239, pp. 105-117, 8/1/ 2004.

[65] A. Abdelrasoul, H. Doan, and A. Lohi, "A mechanistic model for ultrafiltration membrane fouling by latex," *Journal of Membrane Science,* vol. 433, pp. 88-99, Apr 15 2013.

[66] L. Bowman and J. D. Meindl, "The Packaging of Implantable Integrated Sensors," *Biomedical Engineering, IEEE Transactions on,* vol. BME-33, pp. 248-255, 1986.

[67] J. B. Park and R. S. Lakes, *Biomaterials*, Third ed.: Springer New York, 2007.

[68] G. Jiang and D. D. Zhou, "Technology Advances and Challenges in Hermetic Packaging for Implantable Medical Devices," in *Implantable Neural Prostheses 2: Techniques and Engineering Approaches*, D. Zhou and E. Greenbaum, Eds., ed New York, NY: Springer New York, 2010, pp. 27-61.

[69] Mercado and e. al., "Digital Health and Bio-Medical Packaging," in *Materials for Advanced Packaging*, D. Lu and C. P. Wong, Eds., ed: Springer Science + Business, 2009.

[70] M. Kothari and C. Chui, "Hermetic seal and method to create the same," 2008.

[71] L. Bowman and J. D. Meindl, "The Packaging of Implantable Integrated Sensors," *IEEE Transactions on Biomedical Engineering,* vol. BME-33, pp. 248-255, 1986.

[72] G. Voskerician, M. S. Shive, R. S. Shawgo, H. von Recum, J. M. Anderson, M. J. Cima*, et al.*, "Biocompatibility and biofouling of MEMS drug delivery devices," *Biomaterials,* vol. 24, pp. 1959-67, May 2003.

[73] Franz and e. al., "Imune responses to implants - A review of the implications for the design of immunomodulatory biomaterials," *Biomaterials,* vol. 32, pp. 6692-6709, 2011.

[74] W. H. Ko and T. M. Spear, "Packaging Materials and Techniques for Implantable Instruments," *Engineering in Medicine and Biology Magazine,* vol. 2, pp. 24-38, 1983.

[75] L. Xiao, A. Demosthenous, and N. Donaldson, "Implantable Stimulator Failures: Causes, Outcomes, and Solutions," in *Engineering in Medicine and Biology Society, 2007. EMBS 2007. 29th Annual International Conference of the IEEE*, 2007, pp. 5786-5789.

[76] S. K. Lower, "Solutions," in *chem1 virtual textbook a reference text for General Chemistry*, ed: Simon Fraser University.

[77] M. H. Lietzke and R. W. Stoughton, "The calculation of activity coefficients from osmotic coefficient data," *The Journal of Physical Chemistry,* vol. 66, pp. 508-509, 1962.

[78] G. R. Pazuki, "Correlation and prediction of osmotic coefficient and water activity of aqueous electrolyte solutions by a two-ionic parameter model," *Journal of Chemistry Thermodynamics,* vol. 37, pp. 667-670, 2005.

[79] F. Maloberti and P. Malcovati, "Microsystems and Smart Sensor Interfaces: A Review," *Analog Integrated Circuits and Signal Processing,* vol. 15, pp. 9-26, 1998/01/01 1998.

[80] F. M. Wanlass, "Low stand-by power complementary field effect circuitry," U.S. Patent 3356858 A, issued June 18, 1963.

[81] Y. Taur, D. A. Buchanan, W. Chen, and D. J. Frank, "CMOS scaling into the nanometer regime," *Proceedings of the IEEE,* vol. 85, pp. 486 - 504, 1997.

[82] P. Harpe, E. Cantatore, and A. Roermund, "A 2.2/2.7fJ/conversion-step 10/12b 40kS/s SAR ADC with Data-Driven Noise Reduction," presented at the IEEE International Solid-State Circuits Conference, San Francisco, CA, 2013.

[83] N. Reynders and W. Dehaene, "Variation-Resilient Building Blocks for Ultra-Low-Energy Sub-Threshold Design," *IEEE Transactions on Circuits and Systems II: Express Briefs,* vol. 59, pp. 898 - 902, 2013.

[84] S. Adibi, "Biomedical Sensing Analyzer (BSA) for Mobile-Health (mHealth)-LTE," *IEEE Journal of Biomedical and Health Informatics* vol. PP, p. 1, May 30 2013.

[85] B. Razavi, *Design of analog CMOS integrated circuits*, Preview ed. Boston: McGraw-Hill, 2000.

[86] C. Mead, "Computation in Neuromorphic Analog VLSI Systems," ed: Addison Wesley, 1989.

[87] C. H. Luo and Y. Rudy, "A dynamic model of the cardiac ventricular action potential. I. Simulations of ionic currents and concentration changes," *Circ Res,* vol. 74, pp. 1071-96, Jun 1994.

[88] M. S. J. Steyaert and W. Sansen, "Power supply rejection ratio in operational transconductance amplifiers," *Circuits and Systems, IEEE Transactions on,* vol. 37, pp. 1077-1084, 1990.

[89] S. Kerzenmacher, J. Ducrée, R. Zengerle, and F. von Stetten, "Energy harvesting by implantable abiotically catalyzed glucose fuel cells," *Journal of Power Sources,* vol. 182, pp. 1-17, 7/15/ 2008.

[90] L. A. Fernandes, E. Johannessen, M. Azadmehr, and P. Hafliger, "Low power integrated electronics system for the operation of a miniaturized hydration sensor," presented at the IEEE International New Circuits and Systems (NEWCAS), Trois-Rivières, Canada, 2014.

[91] L. A. L. Fernandes, M. Azadmehr, E. A. Johannessen, H. P, x00E, and fliger, "An Osmotic Pressure Sensor for Monitoring the Level of Hydration in Biological Fluids," *IEEE Sensors Journal,* vol. 16, pp. 4331-4337, 2016.

[92] N. Trung Thanh, L. A. L. Fernandes, and P. Hafliger, "An Energy-Efficient Implantable Transponder for Biomedical Piezo-Resistance Pressure Sensors," *Sensors Journal, IEEE,* vol. 14, pp. 1836-1843, 2014.

[93] E. Johannessen and P. Häfliger, "Analog to interval encoder with active use of gate leakage for an implanted blood-sugar sensor," presented at the IEEE Biomedical Circuits and Systems, 2008.

[94] Mead and Carver, "Analog VLSI and neural systems," ed: Addison-Wesley, 1989, pp. 371-379.

[95] A. Brokaw, "A simple three-terminal IC bandgap reference," in *Solid-State Circuits Conference. Digest of Technical Papers. 1974 IEEE International*, 1974, pp. 188-189.

[96] T. Delbruck and A. van Schaik, "Bias current generators with wide dynamic range," in *Circuits and Systems, 2004. ISCAS '04. Proceedings of the 2004 International Symposium on*, 2004, pp. I-337-I-340 Vol.1.

[97] P. E. Allen and D. R. Holberg, "LECTURE 250 – SIMULATION AND MEASUREMENT OF OP AMPS (Georgia Tech 2010)," in *CMOS Analog Circuit Design*, 2nd ed New York: Oxford University Press, 2002, pp. 310-341.

[98] K. Biswas and S. Kal, "Etch characteristics of KOH, TMAH and dual doped TMAH for bulk micromachining of silicon," *Microelectronics Journal,* vol. 37, pp. 519-525, Jun 2006.

[99] K. Hongsirikarn, J. G. Goodwin Jr, S. Greenway, and S. Creager, "Effect of cations (Na+, Ca2+, Fe3+) on the conductivity of a Nafion membrane," *Journal of Power Sources,* vol. 195, pp. 7213-7220, 11/1/ 2010.

[100] A. Jena; and K. Gupta;, "Characterization of water vapor permeable membranes," *Desalination,* vol. 149, pp. 471-476, 2002.

[101] N. T. Trung and P. Häfliger, "Time domain ADC for blood glucose implant," *Electronics Letters,* vol. 47, pp. 18 - 20, 22 December 2011.

[102] J. Xu, G. P. Sheng, H. W. Luo, W. W. Li, L. F. Wang, and H. Q. Yu, "Fouling of proton exchange membrane (PEM) deteriorates the performance of microbial fuel cell," *Water Res,* vol. 46, pp. 1817-24, Apr 15 2012.

Papers omitted due to publisher's restrictions